Star formation efficiency in extended UV disks and at high redshifts

Isadora Chaves Bicalho

▶ **To cite this version:**

Isadora Chaves Bicalho. Star formation efficiency in extended UV disks and at high redshifts. Astrophysics [astro-ph]. Université Paris sciences et lettres, 2018. English. NNT : 2018PSLEO018 . tel-02122710

HAL Id: tel-02122710
https://theses.hal.science/tel-02122710

Submitted on 7 May 2019

HAL is a multi-disciplinary open access archive for the deposit and dissemination of scientific research documents, whether they are published or not. The documents may come from teaching and research institutions in France or abroad, or from public or private research centers.

L'archive ouverte pluridisciplinaire **HAL**, est destinée au dépôt et à la diffusion de documents scientifiques de niveau recherche, publiés ou non, émanant des établissements d'enseignement et de recherche français ou étrangers, des laboratoires publics ou privés.

PSL
UNIVERSITÉ PARIS

THÈSE DE DOCTORAT
DE L'UNIVERSITÉ PSL

Préparée à l'Observatoire de Paris

STAR FORMATION EFFICIENCY IN EXTENDED UV DISKS AND AT HIGH REDSHIFT

Soutenue par

Isadora CHAVES BICALHO

Le 10 septembre 2018

Ecole doctorale n°127

Astronomie et astrophysique d'Île-de-France

Spécialité

Astronomie, astrophysique

Composition du jury :

Samuel BOISSIER Chargé de recherche, LAM	*Rapporteur*
Françoise COMBES Astronome, LERMA	*Directrice de thèse*
Miroslava DESSAUGES-ZAVADSKY Chercheur, Observatoire de Genève	*Examinatrice*
Bruno GUIDERDONI Directeur de recherche, CRAL	*Rapporteur*
Daniel ROUAN Directeur de recherche, LESIA	*Président du jury*
Philippe SALOMÉ Astronome-adjoint, LERMA	*Codirecteur de thèse*

l'Observatoire de Paris | PSL

THÈSE DE DOCTORAT
DE L'OBSERVATOIRE DE PARIS

École Doctorale d'Astronomie & Astrophysique d'Île-de-France

LERMA, Observatoire de Paris

STAR FORMATION EFFICIENCY IN EXTENDED UV DISKS AND AT HIGH REDSHIFT

Présentée par

Isadora Chaves Bicalho

Et soutenue publiquement le 10 de Septembre de 2018 :

Françoise COMBES	Directrice de thèse
Philippe SALOMÉ	Co-Direteur de thèse
Samuel Boissier	Rapporteur
Bruno Guiderdon	Rapporteur
Daniel Rouan	Président du Jury
Miroslava Dessauges-Zavadsky	Examinatrice

Except where otherwise noted, this work is licensed under
http://creativecommons.org/licenses/by-nc-nd/3.0/

Résumé

La question de la formation et l'évolution des galaxies est certainement l'une des énigmes les plus profondes de l'astrophysique contemporaine. Une galaxie étant définie par son contenu en gaz et étoiles, toute théorie de la formation des galaxies doit étudier la question de la formation des étoiles. Les observations ont montré que les étoiles se forment dans des nuages moléculaires denses. Le taux de formation des étoiles au sein d'une galaxie dépend donc de sa capacité à former des nuages moléculaires. La détermination de ces processus et de leur efficacité sont parmi les questions les plus importantes dans notre compréhension de la formation d'étoiles. Le présent travail étudie les lois de formation d'étoiles dans un large éventail de conditions physiques et dynamiques, y compris dans des environnements de faible densité et jusqu'à des échelles de nuages moléculaires, ainsi que des galaxies à grand redshift, pour explorer l'histoire cosmique de la formation des étoiles. Les environnements à faible densité, comme les parties externes des disques des galaxies, imitent les conditions physiques des galaxies naines et aussi celle des galaxies de l'Univers primordial. Au cours du temps de Hubble, il y a eu un pic dans le taux de formation d'étoiles, à z $\sim$ 1-2, il y a environ dix milliards d'années. Ensuite, le taux moyen de formation d'étoiles a chuté drastiquement d'un facteur 20 jusqu'au taux actuel. Cette thèse se concentre sur l'efficacité de la formation des étoiles dans deux contextes : dans les environnements de faible densité, comme les disques externes des galaxies et à l'époque du maximum de la formation d'étoiles cosmique.

Abstract

Perhaps one of the most enigmatic domains of astrophysics is that of galaxy formation and evolution. A galaxy is defined by its stellar and gas contents. Hence, any theory of galaxy formation has to address the question of the formation of stars. Observations show that star formation takes place in dense molecular clouds. Therefore, the efficiency of star formation of a galaxy is determined by its ability to form molecular clouds.

The determination of these processes and their efficiency is among the most important issues in our understanding of star formation. The present work studies the star formation laws in a wide range of physical and dynamical conditions, even in low density environments and down to molecular cloud scales, as well as high redshift galaxies, to explore the cosmic star formation history.

Low density environments, like the outermost disk of galaxies mimic the physical conditions of dwarf galaxies and also that of galaxies in the early Universe. Across the Hubble time, there was a peak in the star formation rate, at z$\sim$ 1-2, about ten billions years ago. Then the average star formation rate dropped by a factor 20 down to the present rate. This Ph.D focuses on the star formation efficiency in two contexts: in low environments, like outer galaxy disks and at the epoch the near the peak of star formation.

Research summary

The extended ultraviolet (XUV) disk galaxies are one of the most interesting objects studied over the last few years. The UV emission, revealed by GALEX, extends well beyond the optical disk, after the drop of Hα emission, the usual tracer of star formation. This shows that sporadic star formation can occur in a large fraction of the HI disk, at radii up to 3 or 4 times the optical radius. These regions, dominated by almost pristine gas and poor in stars, bear some similarity to early stages of spiral galaxies and high-redshift galaxies. One remarkable example is M83, a nearby galaxy with an extended UV disk reaching 2 times the optical radius. It offers the opportunity to search for the molecular gas and characterise the star formation in outer disk regions, traced by the UV emission. We obtained deep CO(2-1) observations with ALMA of a small region in a 1.5'× 3' rectangle located at $r_{gal} = 7.85'$ over a bright UV region of M83. However, our progress in understanding these XUV disks has been halted by the difficulty of detecting molecular gas via CO emission. No highly significant ($> 5\sigma$) CO was detected by ALMA in the M83 XUV disk, while we expected to detect 20-30 molecular clouds with $SNR > 17$. A possible explanation is that the expected molecular clouds are CO-dark, because of the strong UV radiation field. The latter preferentially dissociates CO with respect to H_2, due to the small size of the star forming clumps in the outer regions of galaxies.

Star formation efficiency at high redshifts during the winding-down of star formation were obtained with a linear relation and with a constant depletion time. The Plateau de Bure High-z Blue Sequence Survey (PHIBSS) survey aims to understand early galaxy evolution from the perspective of the molecular gas reservoirs. The project lasted for four years of observations. The PHIBSS combined sample of about 200 galaxies allowed a better understanding of the Kennicut-Schmidt (KS) law using the superficial density of H_2. The NOEMA observations with a spatial resolution of about 3" enables us to have a broad idea of the inner dynamics of high redshift galaxies. However this is not sufficient to resolve substructures. Mapping the CO(3-2) or CO(4-3) line emission with ALMA could allow us to characterize the star-forming regions of these galaxies and their kinematics with a good resolution. Considering the line widths of the CO(2-1) unresolved PHIBSS2 observations, we thus anticipate about 6 gaseous clumps per galaxy on average. Assuming 50% uncertainties on the final molecular gas mass and SFR densities, a sample of six galaxies should consequently let us estimate the mean depletion time and the average Toomre stability parameter at the scale of the star-forming clumps with a 17% accuracy. However, this was not what we found in our ALMA observations. The study of this sample, with CO(2-1), CO(3-2) and CO(4-3) emissions could constrain and study better the star formation efficiency in mean sequence galaxies after the star formation peak. The PHIBSS2 could do measurements to confirm the uniformity of the galaxy-averaged KS relation between the total SFR and molecular gas surface densities, with a linear exponent $n = 1$ at each epoch and a depletion time that varies slowly with redshift.

Acknowledgements

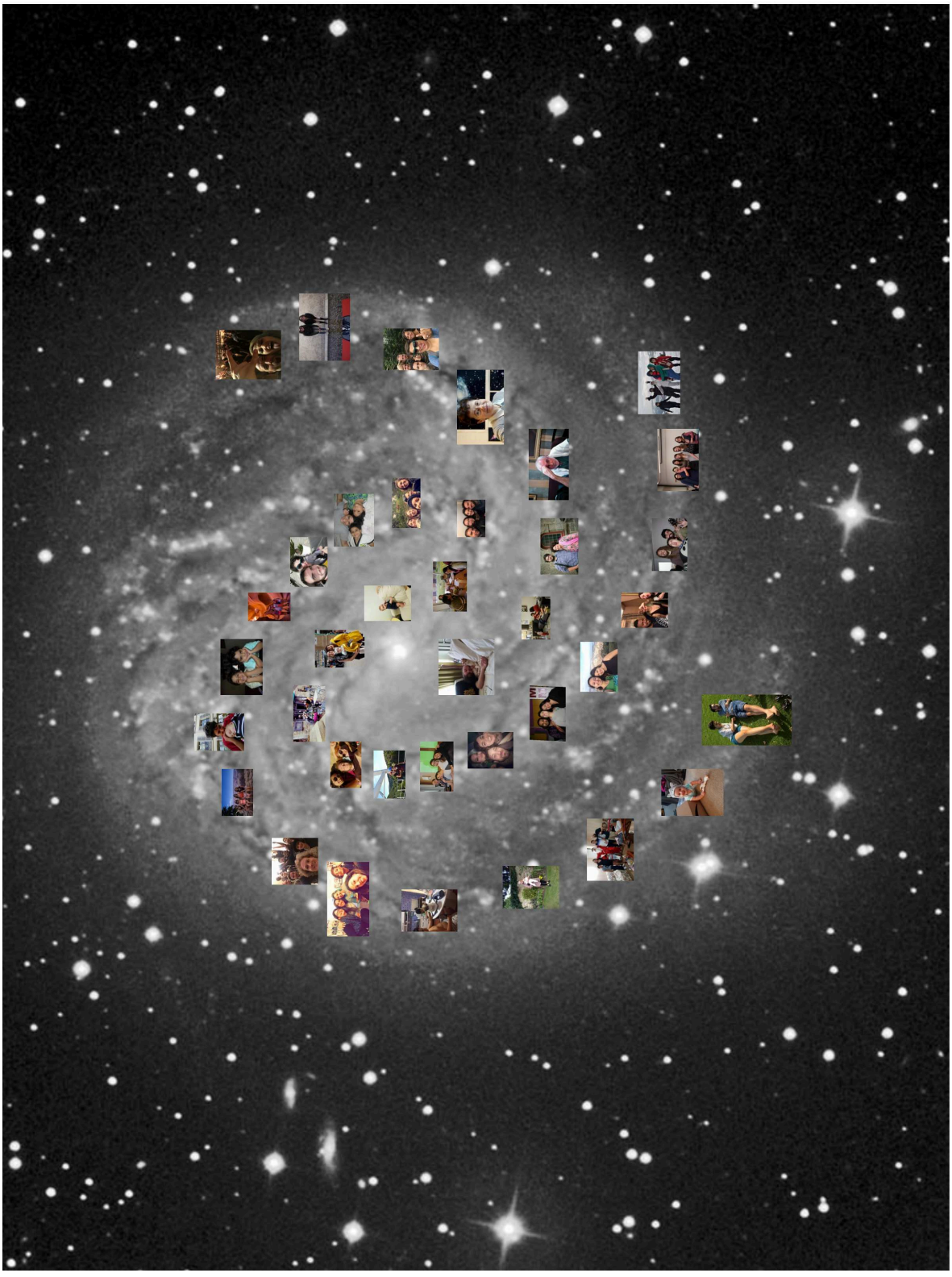

Contents

Résumé i

Abstract iii

Research summary v

Acknowledgements vii

Table of contents x

List of figures xii

Introduction

1 Star formation through cosmic time 3

1.1 Galaxies: the great discovery . . . 5

1.1.1 Observing nebulae . . . 5

1.1.2 Nebulae to galaxies . . . 6

1.1.3 Galaxy classification . . . 8

1.2 How do galaxies form? . . . 9

1.2.1 Structure formation . . . 10

Structure formation trough mergers . . . 11

1.2.2 Galaxy formation . . . 12

1.3 Interstellar Medium Gas . . . 15

1.3.1 Molecular gas . . . 16

1.3.2 Giant Molecular Clouds: the site of star formation . . . 17

GMC dynamics . . . 18

Formation of GMCs and formation of H_2 . . . 18

1.4 Star Formation Rate . . . 20

1.4.1 Indicators from direct stellar light . . . 21

UV continuum . . . 21

Optical . . . 21

1.4.2 Indicators from dust . . . 22

1.4.3 Indicators from mixed processes . . . 23

1.5 Star formation Efficiency . . . 24

1.5.1 Kennicutt-Schmidt relation . . . 24
Depletion time . . . 26
Molecular star formation law . . . 27
1.5.2 What controls SFE . . . 28
Magnetic Fields . . . 28
Turbulence . . . 29
Self-regulation . . . 29

Part One - XUV Disk Galaxies

2 XUV disk galaxies 33
2.1 Extended discs . . . 36
2.1.1 Morphology and classification . . . 39
2.1.2 Star formation in the outer disk . . . 40
2.1.3 Importance . . . 42
2.2 Molecular gas in XUV disks galaxies . . . 42
2.3 The case of M83 . . . 43
2.3.1 Observations . . . 44
2.3.2 CO emission detection and upper limits . . . 46
2.3.3 Matched Filter Technique . . . 48
2.3.4 Stacking of CO spectra, according to the HI velocity . . . 49
2.3.5 Star formation diagram . . . 51
2.4 Discussion and Perspectives . . . 52
2.4.1 M83 star formation efficiency . . . 52
2.4.2 Diagnostic comparison . . . 53
2.4.3 The dearth of CO emission in the outer disc of M83 . . . 53
2.4.4 Perpectives . . . 56

Part Two - The star formation efficiency at high-redshift

3 Star formation in galaxies at higher redshift 59
3.1 The star formation at high redshift . . . 62
3.1.1 The cosmic star formation history . . . 62
3.1.2 Main Sequence galaxies . . . 63
3.1.3 SFE at high redshift . . . 64
3.2 The PHIBSS Program . . . 65

4 PHIBSS2: Plateau de Bure HIgh-z Blue Sequence Survey 2 69
4.1 The PHIBSS2 Large Program . . . 69
4.1.1 Sample . . . 72
4.1.2 Observations . . . 72
4.1.3 The Kennicutt-Schmidt relation in PHIBSS2 . . . 76
4.2 Resolved galaxies with NOEMA . . . 78

5 ALMA 83

5.1 Observations 83
5.1.1 sample selection 84

Conclusion

6 Conclusion and perspectives **89**
6.1 XUV galaxies 90
6.2 High redshift galaxies 91

References **95**

List of Figures

1.1 William Herschel's nebulae . . . 6
1.2 Andromeda Galaxy by Isaac Roberts in 1888 . . . 7
1.3 Hubble's law . . . 8
1.4 Hubble Classification . . . 9
1.5 Vaucouleurs galaxy classification . . . 10
1.6 Galaxy Merger . . . 11
1.7 NGC 2623 . . . 12
1.8 Galaxy Formation scenario . . . 13
1.9 Figure 8 from Bolatto et al. (2013) . . . 19
1.10 Mixed SFR indicator from Calzetti et al., 2007 . . . 23
1.11 Star formation law from (Kennicutt, 1998) . . . 24
1.12 KS from Bigiel et al. (2008). . . . 30

2.1 MK01 figure . . . 36
2.2 Figure fromMartin & Kennicutt (2001) . . . 37
2.3 GP07 Figure . . . 38
2.4 The M83 radial profiles . . . 41
2.5 The M83 image . . . 43
2.6 The M83 image observations . . . 45
2.7 Scheme of the ALMA mosaic of M83 observations . . . 46
2.8 Detection assessment . . . 47
2.9 The H_α image of the region is shown, from Subaru (Koda et al., 2012). The magenta circles show the positions where CO was searched for. . . . 47
2.10 Upper limits . . . 48
2.11 Histogram using the MT technique . . . 49
2.12 CO and HI spectra . . . 50
2.13 CO and HI spectra . . . 51
2.14 M83 KS . . . 52
2.15 KS diagram of XUV disk galaxies . . . 54
2.16 Figure proposal . . . 56

3.1 SFCH . . . 63
3.2 SFCH . . . 64
3.3 SFE versus redshift . . . 65
3.4 CO velocity maps from Tacconi et al. (2010) . . . 66
3.5 PHIBSS KS, z=2-3 and z=1-1.5 from Tacconi et al. (2013) . . . 67

4.1 $t_{dep} = M_{molgas}$/SFR from (Tacconi et al., 2018) 70
4.2 Galaxy parameters as a function of the bulge-to-total mass ratio from Freundlich et al. (submitted). 71
4.3 KS relation using a weighted least-square fitting 77
4.4 KS relation with different data sample 78
4.5 PHIBSS2 KS relation 79
4.6 EG008 maps 80
4.7 XA54 maps 81
4.8 XG55 maps 82

5.1 CO(4-3) spectra for two galaxies 85

Introduction

CHAPTER 1

Star formation through cosmic time

Perhaps one of the most enigmatic domains of astrophysics is that of galaxy formation and evolution. With current technological advances, our ability to understand the inner mechanics and subtleties of galaxies is ever improving. As an example, the advent of increasingly powerful space and ground-based telescopes, the boundaries and depths within which humanity's unfaltering eye may probe is continuously being pushed further. The curiosities and intricacies we have long found ourselves unable to fully resolve are rapidly entering into the realm of contemporary empirical efforts.

Studying galaxies, how they are 'born', informs us about the Universe history and also helps us to trace the Universe structure. The early Universe was very homogeneous and galaxies started to form from gravitational instabilities. The standard model of cosmology, known as Λ-CDM, is very constrained by the Cosmic Microwave Background. This model is a Friedmann-Lemaître-Robertson-Walker model assuming the existence of a cosmological constant (Λ) and cold dark matter (CDM). Observations show that there exist much less massive galaxies than what theory predicts. The cause of this difference is still in debate in the scientific community.

Observations show that stars are formed in galaxies at much larger rates ten billion years ago than now. Nowadays, the cosmic star formation density is twenty times lower than at the beginning. Stars are formed from cold molecular gas, and high rate in the star formation means a high gas supply.

This chapter introduces some aspects of galaxy formation and evolution. The first section provides an historical perspective on observations of nearby and distant galaxies. The second section comes back to the formation and evolution scenario for galaxies within the standard ΛCDM cosmological model.

The last section focuses in star formation and its efficiency in galaxies. The section describes mainly the star formation laws and their contribution in the understanding of galaxy formation. For the introduction of this work I have read books and reviews, principally from renown astronomers that want to share their knowledge with the community. This chapter was inspired by the reading of the books from Roy (2017), Combes (2009), Sparke & Gallagher (2007) and Mo et al. (2010).

Galaxies: the great discovery

Galaxies are the bricks of the enormous building called Universe. They are extraordinary objects for probing and understanding the Universe. Through the late 1910s and all 1920s astronomers proved that our Milky Way was one of numerous "island-universe" with colossal distances between them. The German naturalist and explorer Alexander von Humboldt (1769-1859) coined the expression of "island-universe" for what was called "nebulae".

Observing nebulae

The Greek-Egyptian mathematician and astronomer Claudius Ptolemy of Alexandria (c.90-168) was the first to mention objects in the sky. He identified "nebulous stars": Messier 34, Messier 44, Messier 7 and the stellar pair λ Sagittarius. For him, Meissa was "the nebulous star in the head of Orion". One thousand five hundred years later, Galileo Galilei (1564-1642) showed that Meissa was simply a pack of unresolved stars. For Galileo and his contemporaries, all nebulous patches are expected to be resolved into stars through a powerful enough telescope. The Persian astronomer Abd al-Rahman ibn Umar al-Sufi (903-986) wrote about the "cloud" of Andromeda in his *Book of the Constellations of the Fixed Stars of 965*, including the 48 Ptolemaic constellations, and drawings of each constellation as seen on the celestial globe. The nebulous of Andromeda was seen through the Medieval epoch; indeed this object is visible to the naked eye. Andromeda is one of the 3 other objects (apart from the Milky Way) that are visible to the naked eye: Messier 31, Messier 33, and the two Magalhães clouds (in English they translate the name of the Portuguese navigator Fernão de Magalhães to Magellan).

Despite the fact that Galileo observed great portions of the sky with his telescope, we have no evidence that he truly observed the Andromeda "nebula". Galileo surmised that with greater power in instrumentation one could resolve the "clouds" into stars like he did with Meissa. After the advance of the telescopes, astronomers became more and more intrigued by "nebulae". It was the French astronomer Charles Messier (1730-1817) who provided a great catalog of nebulae, used even nowadays. Ahead of his time, another French astronomer Nicolas Louis de Lacaille (1713-62) catalogued 42 nebulae and clusters of the Southern sky and proposed a practical classification of nebulae. He divided them in three groups: the first are nebulae without stars, then nebulous stars in clusters and finally stars accompanied by nebulosity. This was the base for the known globular clusters, open clusters and gaseous nebulae.

The same kind of concept about the "island-universe" was used in 1755 by the philosopher Immanuel Kant (1724-1804). Using consistency arguments and Newton's theory of gravitation, he speculated about the cosmic shapes. He denied the idea where nebulae are a huge flattened star, flattening induced by rapid rotation (Pierre Louis de Maupertuis's idea). According to him, I quote "there are no such individual huge stars but systems of many stars". He worked with this nebular hypothesis of an interstellar cloud of matter

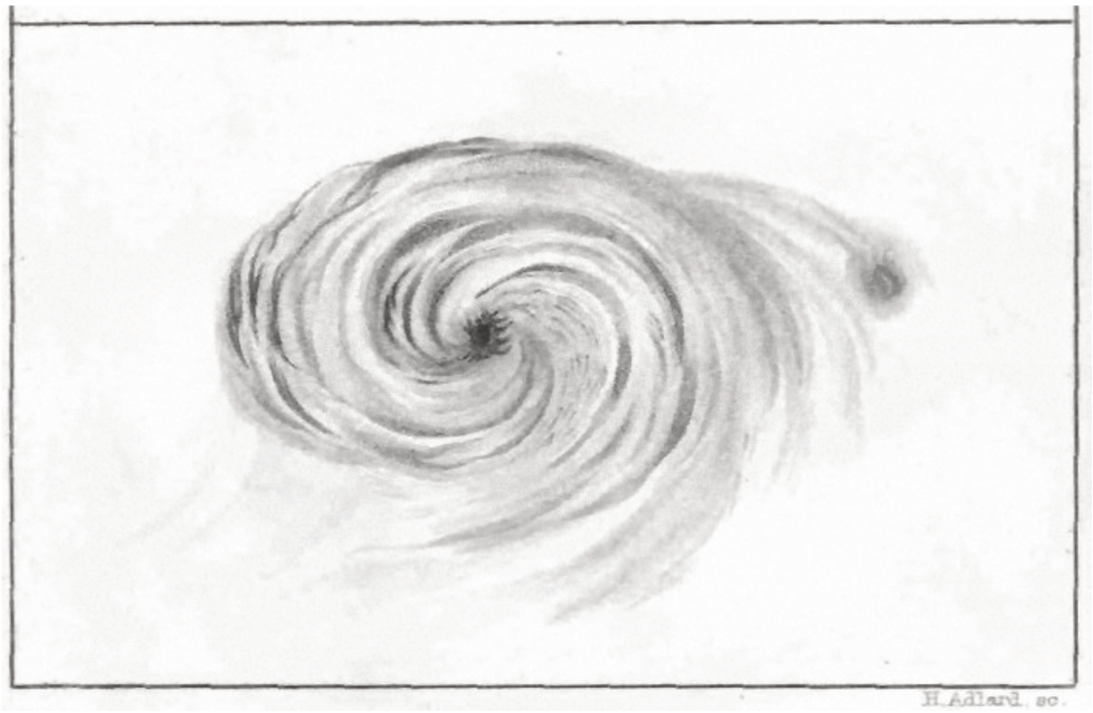

Figure 1.1 – *One of the famous nebulae drawn by John William Herschel, Outlines of Astronomy, Sixth edition, London 1859.*

collapsing under the gravity's action. This hypothesis gained strength and popularity with Pierre-Simon de Laplace in *Exposition du système du monde.*

Carolina Herschel (1750-1848) is among the most famous women in the history of astronomy. Caroline H. was famous by her observations and competences in cataloguing about 2.500 star clusters and nebulae. She was really intrigued by nebulae and suggested to her brother William Herschel to study these objects "...her demonstration to William that nebulae were there in abundance awaiting discovery was to prove momentous." said M. Hoskin in his book *Discovery of the Universe: William and Caroline Herschel.* The Herschels were really important to explore and describe the nebulae and everything that came further.

Nebulae to galaxies

The new technique of spectroscopy was employed to spread the lights of stars and nebulae. It was the german physicist Joseph von Fraunhofer (1787-1826) that invented the spectroscope in 1814. The British couple William Huggins (1824-1910) and Margaret Lindsay Huggins (1848-1915) used the spectroscope in astronomy. They found that the spectra of astronomical objects resemble those of the Earth, and could possibly have the same elements. Applying spectroscopy to the nebulae, William Huggins wrote " The riddle of the nebulae was solved (...) the light of this nebulae had clearly been emitted by a luminous gas".

William Herschel made observations of the Milky Way (MW) and for him, like the traditional view that humankind is the center of everything, all nebulae had to belong to the Milky Way. This galactocentric view was still supported during the 1920s by Harlow Shapley (1885-1972): globular clusters are giant ensembles of millions of stars in a spherical shape. For him, some globular clusters are missing because they are torn apart by tidal forces and destroyed. The same argument was developed for the destruction of spirals, reinforcing the idea that the spiral nebulae we see with telescopes are members of our own galaxy.

Isaac Roberts (1829-1904) was the first to obtain an image of a nebula in Andromeda. It was considered the first photograph of a galaxy. He supported Kant's vision, and he also envisioned the two small galaxies companions of M31. Also, due to the observation in 1885 of a "nova" in M31, the community started to become suspicious. We know today that it was the first time we could observe a Supernova outside of the MW (SN1885). Nevertheless, to have the proof of the existence of "external nebulae" it was necessary to break the barriers that determine accurate distances between "our Universe" and them. It was the idea of using the novae and supernovae like standard candles in this nebulae that started to open the mind of the community. Heber Curtis, George Ritchey and Knut Lundmark were essential for this distance calculations. Leading the distance determination Ernest Opik (1893-1985) analyzed the internal rotation motion of M31 and started to put an end in this great debate.

Figure 1.2 – *Most consider Roberts' magnum opus to be a photograph showing the structure of M31, the Great Nebula in Andromeda taken in 1888. The long exposure photograph revealed the structures in the Andromeda nebulae, which was quite unexpected at the time.*

Cepheid variable stars are very well known nowadays by their character of reliable standard candles. The astronomer Henrietta Swan Leavitt (1868-1921) identified in 1908

a class of variable stars that obeyed a relation between luminosity and period. Leavitt's work changed the paradigm of distance determination. Due to this amazing discovery, Edwin Powell Hubble (1889-1953) used this relation to understand the distances to the galaxies. Hubble determined the extragalactic distances by using the newly calibrated Cepheids from Leavitt. Of course Shapley was incredulous, claiming that the nebulae are located inside of the big Milky Way. Hubble's observations of 1931 supported the study made by George Lemaître (1894-1966) about the expansion of the Universe. Where he describe the expanding and contracting Universe into general relativity equations models in 1927. Unfortunately this work was written in French, and the posterity gave all the credit to Hubble about the velocity-distance relation, now known as the Hubble law.

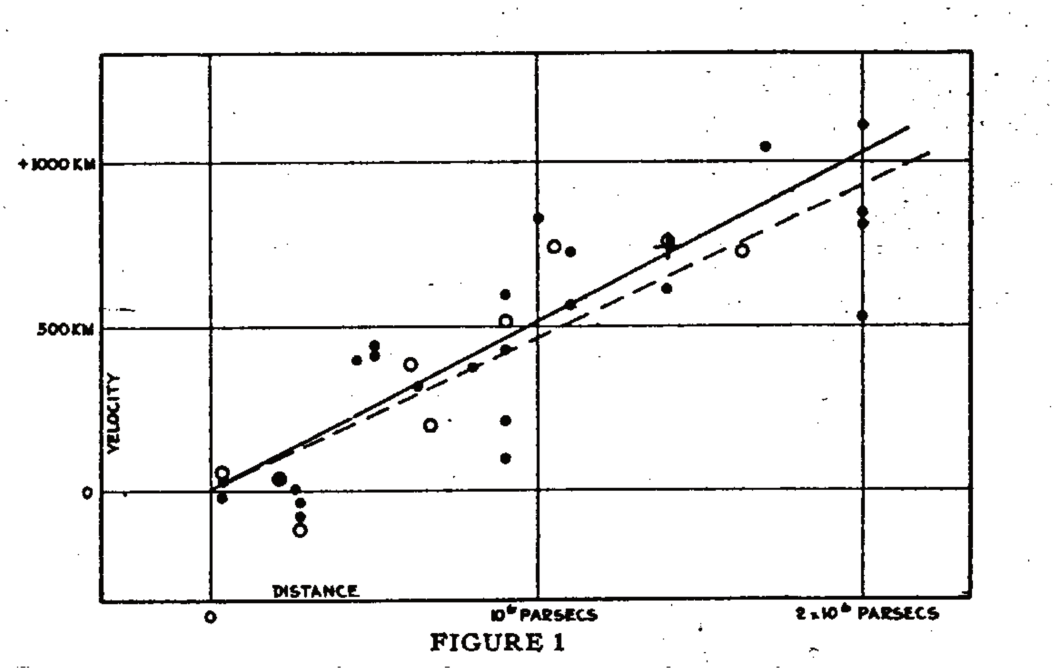

Figure 1.3 – *This is the plot made by Edwin Hubble in 1922. Hubble's law can be easily depicted in a "Hubble Diagram" in which the velocity (assumed approximately proportional to the redshift) of an object is plotted with respect to its distance from the observer. A straight line of positive slope on this diagram is the visual depiction of Hubble's law.*

Galaxy classification

The most recognized morphological galaxy classification was made by Hubble. It is known as the Hubble classification and it was published in 1926, dividing regular galaxies into 3 broad classes: ellipticals, lenticulars and spirals. However, the Swedish astronomer Knut Lundmark (1889-1958) was ahead of Hubble. He proposed a classification system of "anagalactic" nebulae which was analogous to Hubble's classification.

Adelaide Ames (1900-1932) worked on "bright spiral nebulae". She and her advisor, Harlow Shapley, worked on the properties of galaxies and galaxy clusters. They found deviations from isotropy in the general distribution of galaxies. She classified galaxies

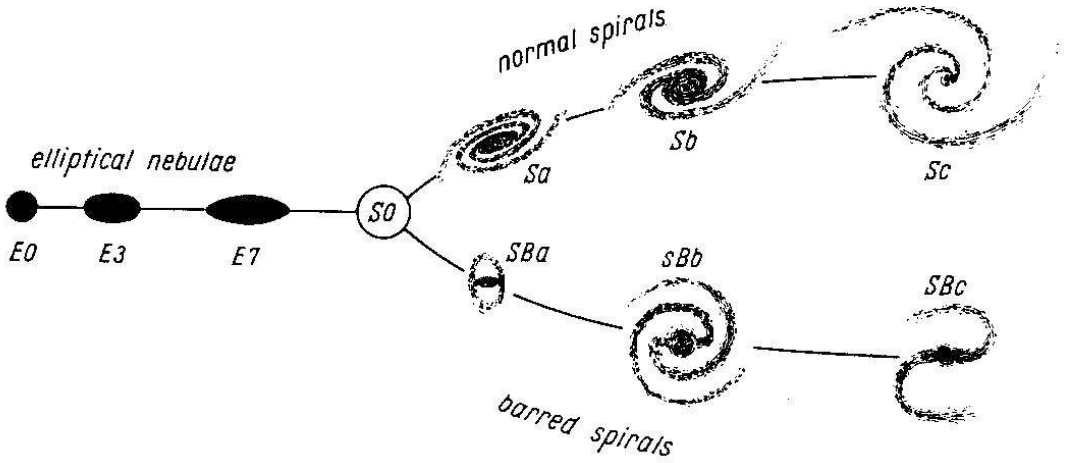

Figure 1.4 – *The tuning-fork style diagram of the Hubble sequence, made by Edwin Hubble. The Hubble sequence is a morphological classification scheme for galaxies invented by Edwin Hubble in 1926. Hubble's scheme divides regular galaxies into 3 broad classes: ellipticals, lenticulars and spirals, based on their visual appearance (originally on photographic plates*

and have even created a new catalogue (Shapley-Ames catalogue), which became a basis for the later research on galaxies and their classifications.

Gerard de Vaucouleurs published a work on the classification and morphology of galaxies in 1959. He introduced a 3D concept, distinguishing shapes of galaxies and their fine structures. His classification was complete and more elegant than Hubble's, but also more complicated. He contributed many things for galaxy classifications, e.g the SAB intermediate bars, pseudo-rings, a more consistent way to classify the lenticulars or S0.

How do galaxies form?

How galaxies are formed? Among many physical parameters, there are some more essential: the rate at which gas masses collapse through self-gravity, their rotation rate and the density fluctuations.

The current standard cosmological model assumes a very homogeneous and isotropic Universe at early times, which is confirmed by the observations of the Cosmic Microwave Background (CMB) radiation. The most preferred cosmological model is the Λ-CDM model. The parameters of this model are well constrained also by the observation of CMB (e.g., Planck Collaboration et al., 2015, 2017). This model is a Big Bang model with a flat Euclidian spatial geometry where the Universe expansion is accelerating and it is 13.8 billion years old (Planck Collaboration et al., 2015).

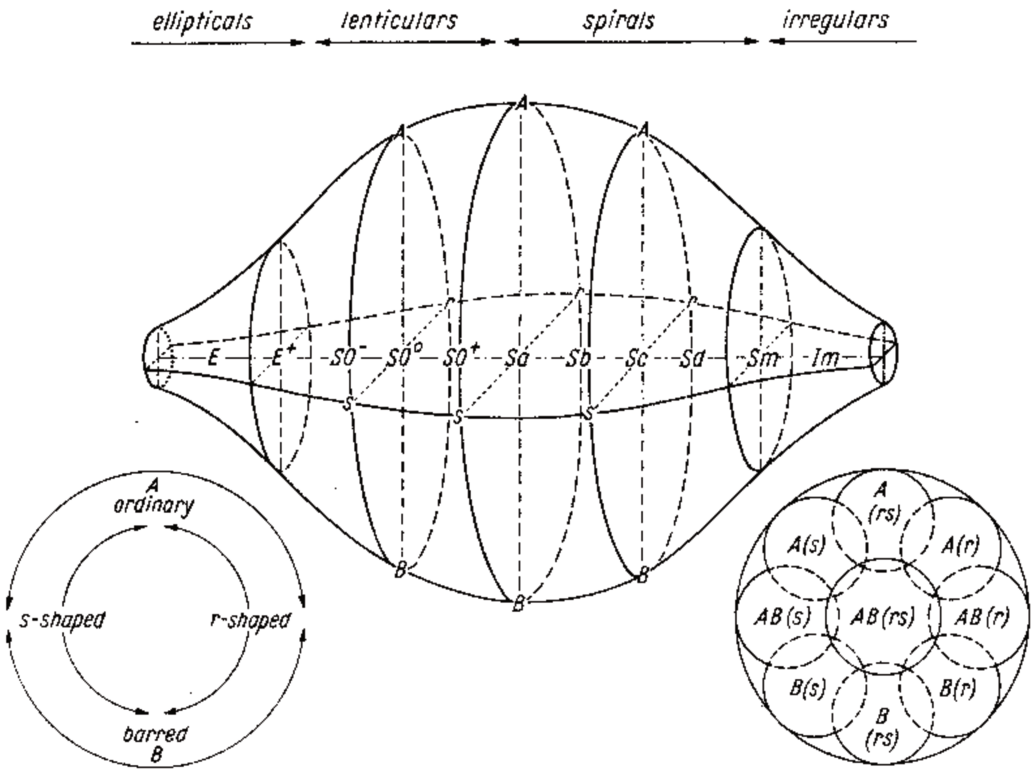

Figure 1.5 – *Gerard de Vaucouleurs developed an extension of the Hubble classification of galaxy types involving a 3D classification grid extending from ellipticals at one end to irregulars at the other. For those and lenticular galaxies, de Vaucouleurs' classification is somewhat similar to Hubble's classification, but for spiral galaxies distinctions are made between normal and ringed, barred and unbarred, and transitional types, and even the simpler structures have various sub-classifications, leading to a more detailed "shorthand" description.*

Structure formation

Structure formation is mostly determined by dark matter dynamics. The scenario of the formation of structures is hierarchical,in a way where the first structures to form are the smallest and they merge afterwards to form the larger ones.In this kind of scenario, the star formation is not continuous,starburts trigged by tidal interactions and also could creat different morphological types by the magnitude of the mergers. Galaxies are assumed to form within the potential wells of dark matter haloes (White & Rees, 1978). This model has not always been the most accepted. During the 1970s and 1980s there were two opposing models: the 'top-down' scenario where existing large structures fragment down to form the galaxies and the 'bottom-up' scenario where the smallest structures form first (this is the origin of the hierarchical scenario). These models are different principally due to the nature of primordial fluctuations from which structures develop. The density fluctuations correspond to fluctuations in gravitational potential, including all particles and photons. There can exist isothermal fluctuations (constant temperature). There are also fluctuations in the temperature and pressure with constant entropy, known as adiabatic fluctuations. Since WMAP observations of the CMB, we know that were exist

fluctuations in temperature, leading to an adiabatic model.

Structure formation trough mergers

With the very informative CMB observations, the properties of the early Universe are well constrained to confirm that indeed the most probable model is the "bottom-up". This paradigm was implemented with the cold dark matter, which supports the hierarchical scenario of dark-matter structure formation. Dark matter interacts just in a gravitational way. After the Big Bang the neutral gas collapses in gravitational wells created by the dark matter. The accumulation of matter in galaxies could occur, then, by interactions with one another. They lose their relative orbital energy and then merge. Mergers are very efficient if the galaxies relative velocities are of the same order as their rotational velocities.

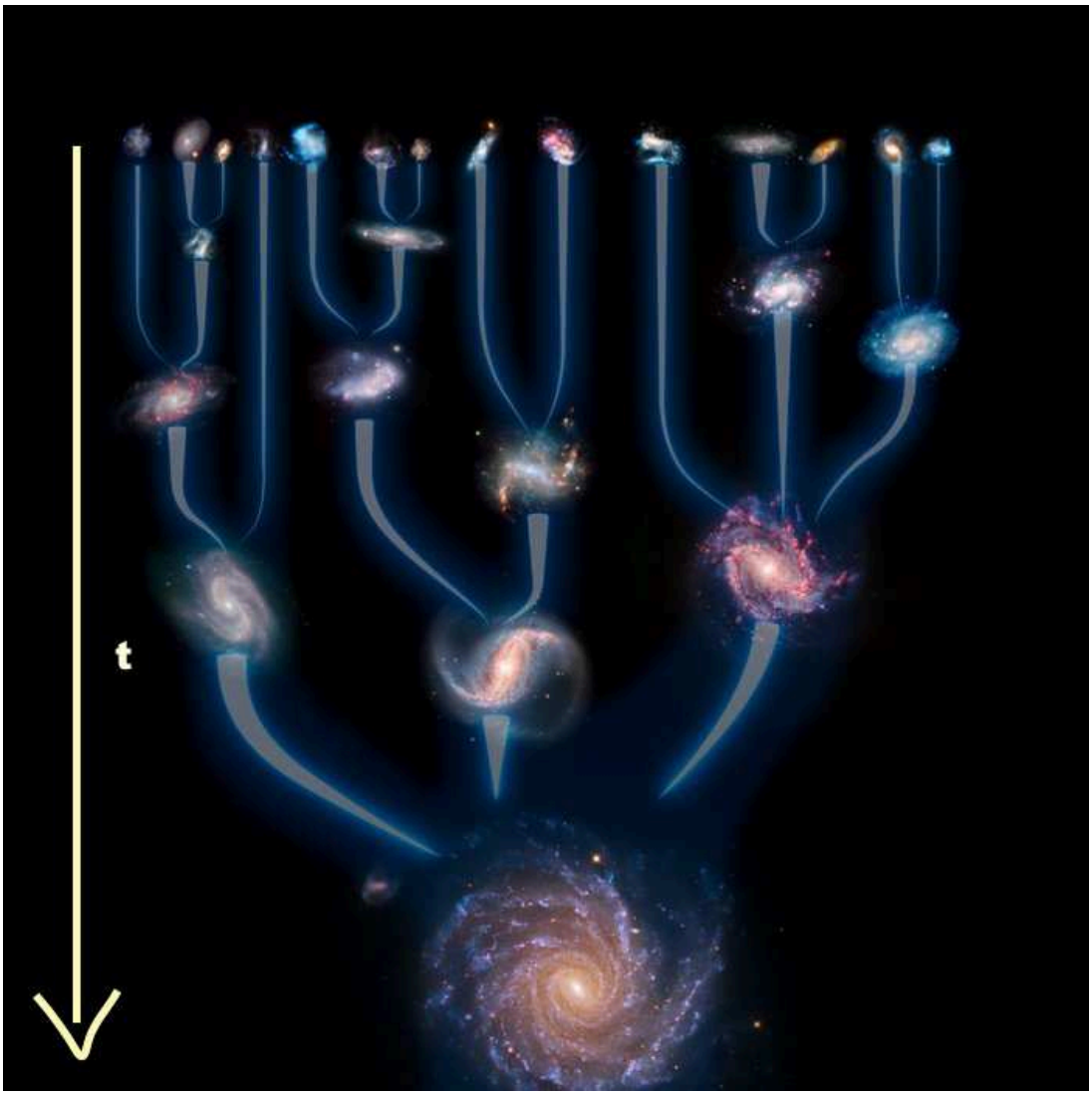

Figure 1.6 – *Representation of a merger tree. The disks grow between the mergers. The halos and the bulges grow during mergers. Figure from ESO images.*

The first galaxies do not have a regular structure; they are very rich in gas and unstable to form clumps. They have not yet acquired their today morphologies. After some star formation, their disks are somewhat stabilised by the stellar component. They still merge with another, and this process contributes to form the galaxy structures, like bulges, halos and disks. This model of galaxy formation is called the merger tree scenario (see figure 1.6): there is a hierarchy of merger events to form the structures. Galaxies are still merging now, although with a reduced frequency, and it is possible to observe in detail the merger between two galaxies (see figure 1.7). However, an open question is still in debate: the only way to create bulge is trough merger? Or are there another way to form this structure? Simulation where able to form bulges that macthed observed scaling relations or low bulge-to-total ratios (e.g Guedes et al. (2013), Okamoto (2013), Aumer et al. (2013) Christensen et al.(2014a)). Moreover, no simulation has yet formed a bulge with a realistic formation history **?**.

Figure 1.7 – *NGC 2623 is a galaxy system in a late stage of merging.*

Galaxy formation

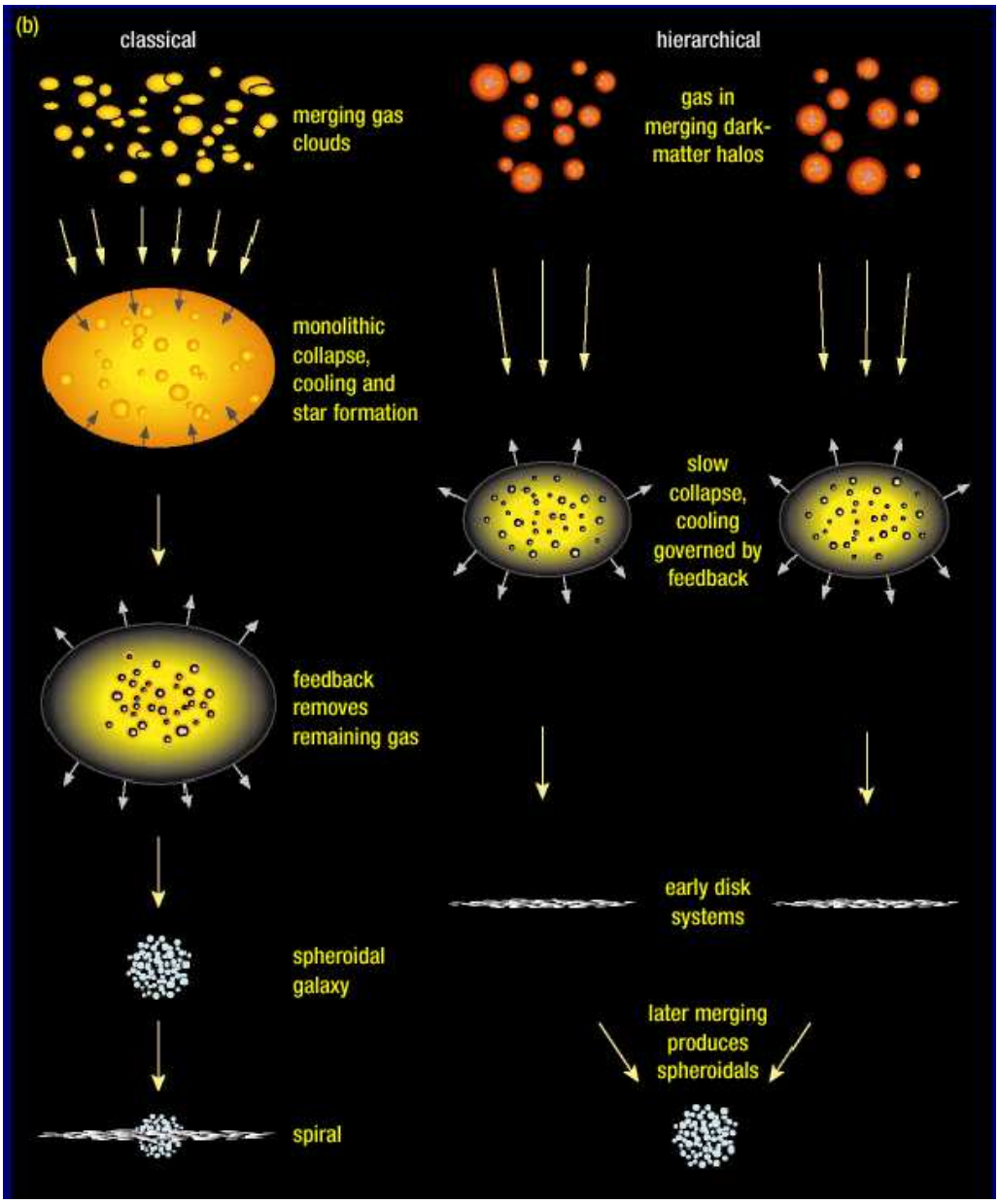

Figure 1.8 – *Representation of the two main scenarios of galaxy formation. Left: there is a group of gas clouds that collapses under its own gravity. They have a rapid cooling and star formation rate, with a time-scale comparable with the collapsing time, and therefore their stars have a spheroidal shape. Afterwards, there is gas expulsion through stellar winds and supernovae explosions (stellar feedback). A gas-free elliptical galaxy or a spherical bulge is thus formed after one or two billion years. Right: the gas collapses quicker than it cools and form stars. The gas has time to become flat and turns into a disk, which will form stars. In this scenario, the disks form before the bulges. Figure from Combes (2009)*

In a hierarchical Universe (see the right hand panel in figure1.8), in which dark matter halos and their gas content grow in mass and size with time, the angular momentum of material accreting onto a galaxy will, on average, increase with time also. As a result, disk formation is an "inside out" process. The inside-out scenario that results from combining spherical collapse and angular momentum redistribution proceeds as follows. Initially the gas and dark matter are coupled and expand with the Hubble flow. The innermost shells turn around. The dark matter virializes, and the gas is shock heated to the virial temperature. The cooling time for these inner shells is very short, and some of the gas may quickly condense into cold lumps and form bulge stars. Later, the outermost shells turn around, and their gas is shock heated. However, for these outer shells, the higher virial temperatures and lower gas densities result in longer cooling times, so that as the gas cools and falls to its corresponding angular momentum radius, it is shocked again and forms stars. Higher angular momentum material ends up outside the bulge and forms the disk.

Lower angular momentum material falls into the bulge, which continues to grow slowly but may be halted by energy input from a supernova and/or a massive black hole that can initiate a wind that blows out the gas.Our present knowledge about the initial distribution of angular momentum, star formation efficiency and supernovae feedback suggest that the exponential disks can arises without the need for viscous redistributions of angular momentum (Dutton 2009; Stringer et al. 2010). The more the gas is densest more the star formation will proceed most rapidly. Which means, in the inner regions of the disks more star formation will occurs and at larger radii the background radiation can prevent the formation of molecular hydrogen. The disk will became stable and then unable to form molecular cloud complexes, given than a radii threshold (Martin and Kennicutt 2001; Schaye 2004).

In a hiererchical universe, disks endure across cosmological spans of time trough frequent merging with another galaxies, dynamical changes from the dark matter strucutres with its own dark matter halo or even to the growth of large scale perturbations (Toth and Ostriker 1992; Velazquez and White 1999; Font et al. 2001; Benson et al. 2004; Kazantzidis et al. 2008; Read et al. 2008; Kazantzidis et al. 2009; Purcell et al. 2009). The cold dark matter model is the most consistent with the presence of thin galactic disks, if there are some fractions of disks probably significantly thickened or destroyed by interactions with dark matter substructures.

The idea that gravitational instability might determine the critical gas density for star formation was introduced by Spitzer 1968 and Quirk 1972. The stability criteria for differentially rotation disks were developed first by Toomre: he determined when a thin gas disk is unstable to axisymmetric perturbations. For this work, Toomre resolved the dispersion relation for radial waves, and established the criterion:

$$Q \equiv \frac{\sigma\kappa}{\pi G\mu} \tag{1.1}$$

The disk is unstable when Q is less than unity. The epicyclic frequency κ, velocity dispersion σ and surface density μ refers to the gas disk at galactocentric radius R. The

parameter Q is named after Toomre (we call it the Toomre parameter). The parameter Q is also likely to be related to the occurrence of instabilities in turbulence-compressed gas on a galactic scale (Elmegreen, 2002).

The dimensionless parameter Q measures the ratio of the centrifugal force from the Coriolis spin-up of a condensing gas perturbation to the self-gravitational force, on the scale where gravity and pressure forces are equal. The derivation of Q assumes that angular momentum is conserved, so the Coriolis force spins up the gas to the maximum possible extent. When $Q > 1$, a condensing perturbation on the scale of the Jeans length spins up so fast that its centrifugal force pulls it apart against self-gravity. Thus gas disks should be generally unstable to form small spiral arms and clouds, even with moderately stable Q, although the growth rate can be low if Q is large.

Interstellar Medium Gas

Molecules and atoms emit radiation at characteristic wavelengths. If we consider the quantified energy levels of an atom, then this radiation correspond to the difference between two energy levels given by:

$$\frac{1}{\lambda} = Z\frac{m_e e^2}{8\epsilon_0^2 h^3 c}\left(\frac{1}{n_1^2} - \frac{1}{n_2^2}\right) \tag{1.2}$$

where Z is the atomic number, n_1 and n_2 are the quantum number of the lower and upper energy levels respectively. The excitation level is defined by their quantum numbers, n, l, s. In which n is the principal quantum number, l is their orbital one and s is the spin. For a given n energy level, the l can have sub-levels, $l = 1, 2, 3, 4...n-1$, divided into $2l+1$ states, the j states. This states is given by $j = |l \pm s|$ and each of this states has several configurations given by $m_j = -j, -j+1...j-2, j-1, j$. An isolated atom can then have all the sub-levels and states to a given level n with the same energy. If, the atom is in presence of magnetic field, the degeneracy is broken and the states reach different excitations energies. This phenomena is called fine structure where there a spin-orbit interaction of the electron.

This spin-orbit interaction within the nucleus can cause a similar phenomenon called hyperfine structure. The hyperfine transition of the hydrogen ground state corresponds to a wavelength of 21cm. In astrophysics, it is really common to use the H1-21 cm line emission to trace the cold atomic phase and derive the atomic gas mass, give by:

$$M(HI) = 2.343 \times 10^5 D_L^2 I(HI)(1+z)^{-1}, \tag{1.3}$$

the mass is in stellar mass $M_\odot, D_L$ is the luminosity distance in Mpc and I(HI) is the integrated flux in Jy.km/s.

The molecules also have electronic energy levels. Their structure enables additional energy levels with a hierarchical structure in energy. Their vibrational levels are subdivided into several rotational levels. The vibrational energy of these levels is given by:

$$E_\nu = \frac{h\omega_o}{2\pi}\left(\nu + \frac{1}{2}\right) \tag{1.4}$$

and the rotational energy by

$$E_J = \frac{\hbar}{2m_r 2r_0^2} J(J+1) \tag{1.5}$$

Where E_ν and E_J are the energy of the vibrational levels and of the rotational levels, respectively. The rotational transitions correspond to a dipole $J \rightarrow J \pm 1$. The most abundant molecule in the Universe, and the cradle where stars form, is the H_2. The molecular hydrogen does not have any dipole moment therefore the rotational transitions are due to a quadrupole moment $J \rightarrow J \pm 2$, and are very weak. Moreover, the transition $J = 0 \rightarrow J = 2$ of H_2 has an excitation temperature of 500k, and the molecular interstellar medium is at T$\sim$ 20K. The cold gas mass is thus poorly estimated with H_2 radiation.

The solution, for astronomical observations, is to use the second most abundant molecule, the carbon monoxide. CO is used then to trace the cold molecular gas, with a dipolar molecule rotational transition that makes it easy to observe. However, the excitation of other molecules depends on the collision rate with H_2.

Molecular gas

Details about fine structure of the ISM are available just for the Milky Way. Even so, it is very reasonable to consider that star formation and the fine structure of the ISM is the same for all the galaxies. In the MW, the ISM is predominantly made of cold gas. A molecular cloud is a condensation of interstellar gas where atoms change phase to become molecules. Molecular clouds contain essentially molecular hydrogen. The density of typical molecular clouds ranges between $10^2 cm^{-3}$ to $10^6 cm^{-3}$, but this value can be higher in regions of star formation. Since the first detection of CO emission from Milky way molecular clouds (Wilson et al 1970), followed in other galaxies, molecular surveys used CO line emission to characterize the molecular content of galaxies. Alternatively, sub-millimeter dust continuum emission is a good tracer of the cold molecular gas mass.

The CO emission, in its low-J levels, is generally optically thick; the molecular mass can then be derived from the CO luminosity, through a conversion factor, calibrated on the Virial masses in Milky-Way clouds. The mass is then related to the cloud size R, the brightness temperature T_b, and the line width $\Delta\nu$. We can express the CO luminosity as in the relation:

$$L'_{CO} = T_b \Delta\nu \Omega_s D_A^2 = T_b \Delta\nu \pi R^2 \tag{1.6}$$

Using the Virial theorem for the case of self-gravitating clouds then:

$$L'_{CO} = T_b \pi R^2 (GM/R)^{1/2} = (\frac{3\pi G}{4\mu})^{1/2} \frac{Tb}{n_{H_2}}^{1/2} M \tag{1.7}$$

Then, it is possible to define a $CO - H_2$ conversion factor, given by $\alpha_{CO} = M_{H_2}/L'_{CO}$. using the above equation, then the conversion factor becomes $\alpha = 2.6 n_{H_2}^{1/2}/Tb$, in the above observational units.

Giant Molecular Clouds: the site of star formation

The information regarding the detailed cloud structure of the ISM is available just in the MW. Since the spatial scales and the time-scale for star formation should be the same from galaxy to galaxy, we will assume the same cloud structure for external galaxies of the same type.

The ISM in MW has a very flattened disk-like structure predominantly of cold gas. The latter is dominated by atomic and molecular hydrogen, and the fraction of H_2 is roughly 30%. The fraction of molecular gas increases with the ISM density. The observations of the molecular gas in the MW show that it is highly clumpy, and distributed in giant molecular clouds. These giant molecular clouds (GMC) reveal to have large amounts of substructures. They have masses between $10^5 - 10^6 M_\odot$ in a few parsecs and the average densities $n_{H2} \simeq 100 - 500 cm^{-3}$. Also, the temperature inferred from molecular lines ratios is typically 10K. GMC are normally homogeneous in temperature, and sometimes there are regions heated by UV radiation from massive stars.

All known star formation is taking place in molecular clouds, i.e. in GMC. Only a low percentage of the total GMC mass ends up to form stars (e.g Hunter et al. 1992). Then, the observed mass distribution of GMCs and their sub-clumps is a power law given by:

$$\frac{dN}{dlnNM} = N_u \left(\frac{M}{M_u}\right)^{-\epsilon} \quad (M \lesssim M_u), \tag{1.8}$$

where $0.3 < \epsilon < 0.9$ and $M_u \sim 5 \times 10^6 M_\odot$ (e.g Rosolowsky 2005).

CMG have a very complex structure, even though we can well define their scaling relation. The masses and velocity widths of each molecular cloud and clump are observed, following their radii so there we have the proportionality: $M \propto R^2$; $\Delta v \propto R^{1/2} \propto \rho^{-1/2}$. e.g Larson et al. 1981. The observed line widths are much larger than what is expected from thermal broadening, indicating that GMC have supersonic turbulence.

GMC dynamics

Assuming that GMCs are self-gravitating, homogeneous, isothermal spheres of gas, they will collapse under their own gravity if their mass exceeds the thermal Jeans mass:

$$M_J = 40 M_\odot \left(\frac{c_s}{0.2 kms^{-1}}\right)^3 \left(\frac{n_{H_2}}{100 cm^{-3}}\right)^{-1/2} \tag{1.9}$$

In absence of any additional pressure force, the GMCs will collapse, and then form stars on a free-fall time, given by:

$$\tau_{ff} \simeq 3.6 \times 10^6 yr \left(\frac{n_{H_2}}{100 cm^{-3}}\right)^{-1/2} \tag{1.10}$$

This is shorter than their observed and inferred lifetimes, which means that the GMCs are supported against gravitational collapse by non-thermal pressure.

Formation of GMCs and formation of H_2

The most abundant molecule in the ISM is molecular hydrogen (H_2), and its abundance is set by formation and destruction processes. Astronomers frequently employ CO emission to measure molecular gas masses, then we have:

$$N(H_2) = X_{CO} W(^{12}C^{16}OJ = 1 - 0) \tag{1.11}$$

where $N(H_2)$ is the column density per squared centimetre and W(CO) is the integrated intensity given in K km/s. If we consider now a relation between the emitting area and the enclosed H_2 mass, including heavier elements in the molecular gas, then:

$$M_{mol} = \alpha_{CO} L_{CO} \tag{1.12}$$

Both α_{CO} and X_{CO} are referred to as the CO-to-H_2 conversion factors. For $X_{CO} = 2 \times 10^{20} cm^{-2} (K.km.s^{-1})^{-1}$ corresponds $\alpha_{CO} = 4.3 M_\odot (K.km.s^{-1}.pc^{-2})^{-1}$, which is typical for the Milky Way.

The main formation mechanism of H_2 is recombination of pairs of absorbed hydrogen atoms on dust grain surface of the ISM. The destruction one is by photo-dissociation. Inside a cloud the intensity of the radiation will diminish due to continuum shielding or attenuation of H_2. The molecules will absorb all photons. Deeper in the cloud it will be difficult to have any dissociation, it is like a self-shielding process.

The less abundant CO molecule is less self-shielded. CO emission is frequently very faint or nonexistent in gas-rich, actively star-forming low-density environments, where metallicity is low. This is true principally in dwarf galaxies and in the outskirts of giant galaxies. Normally, one can expect that lower C and O abundances imply a fainter CO emission. Because CO is optically thick, its luminosity is determined by the emitting area and its brightness temperature, and clouds are much smaller in a low-metallicity environment. The dependence of CO emission on metallicity can be seen in the figure 1.9. Bolatto et al. (2013) describes very well the effect of metallicity in CO and H_2 and also the size of the clump. Samples of clouds in galaxies may enable to cover all the extension of the metallicity range.

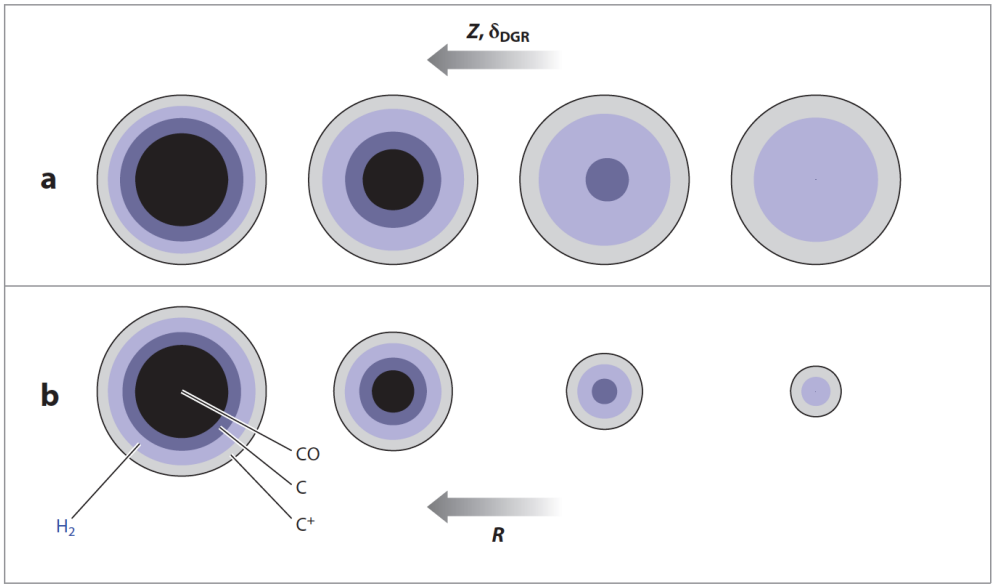

Figure 1.9 – *Effect of metallicity on CO and H_2 in a spherical clump immersed in a uniform radiation field. Blue shading indicates the region where the gas is molecular. Increasingly darker shading shows the regions where carbon is found as C+, C, or CO. Panel a illustrates the effect of decreasing metallicity and dust-to-gas ratio on the distribution of C+, CO, and H_2. Mostly because of the increase in NH required to attain a given A_V, the CO-emitting region is pushed further into the clump until, for a fixed cloud size, it disappears at low enough metallicities. Panel b illustrates the effect of changing the clump size or column density at a fixed metallicity. From Bolatto et al. (2013)*

Leroy et al. (2013) studied the effect of the dust/gas dependency in nearby disc galaxies. They demonstrated that in such galaxies, there is a metallicity dependency in the molecular gas estimation, which can be derived from the star formation laws. Leroy et al. (2013) expressed the correction factor as

$$\alpha_{CO} = \upsilon_{CO-dark}\alpha_{CO}^{MW} \tag{1.13}$$

then, it is possible to express:

$$\upsilon_{CO-dark}(D/G) = 0.5 \exp\left(\frac{0.4}{(D/G)'\Sigma_{GMC}}\right) = 0.67 \exp\left(\frac{0.4}{Z'\Sigma_{GMC}}\right) \quad (1.14)$$

This expression by Leroy et al. (2013) considers the D/G' and Z', which are the dust-to-gas ratio and metallicity normalized to the Galactic values and the surface density to $100 M_{\odot}.pc^{-2}$.

The conversion factor will then depend on the molecular cloud size, itself dependent of the photo-dissiociation regions (PDR). Dust-based determinations suggest that the conversion factor increases with decreasing metallicity, turning sharply below 1/3-1/2 solar metallicity. It is known that CO is not particularly effective in dwarf galaxies. Of course, there are cases where could observe, for example, in Rubio et al. (2016) could observe the core of a molecular cloud at 13% of the metallicity.

Star Formation Rate

The various star formation stages can be measured with both line emission and continuum. Each kind of emission line can be related to a type of stars or stage of its formation, for example, [O II] lines are formed when young very hot stars are already present. The star formation rates (SFR) are estimated using various emission lines in optical (e.g. Hα) or continuum from massive stars or dust grain in ultraviolet (UV) and infrared (IR, mid-IR of FIR).

Calibrations of SFR indicators have been presented in the literature for almost 30 years. Studies find interest in mid-IR or FIR SFR indicators, since they are extinction-free, contrary to UV or optical ones. The latter can have a much higher spatial resolution, and are easy to observe with high sensitivity. The mid-IR and FIR studies have become possible, with new and relatively high angular resolution, high-sensitivity IR space telescopes (Spitzer, Herschel). These have enabled the calibration of monochromatic SFR indicators in nearby galaxies. The UV and optical may be the preferred SFR indicators at very high redshift, when galaxies contained little dust (e.g., Wilkins et al. 2011; Walter et al. 2012) and IR complement with UV and optical wavelengths to study the SFR evolution of galaxies from $z \sim 7 - 10$ to the present (e.g., Giavalisco et al. 2004; Bouwens et al. 2009, 2010). The calibration of SFR indicators is still a issue for studies of distant galaxies. They can be affected by differences in star formation history (SFRH), metal abundances, content and distribution and distribution of stellar populations and dust between low and high redshift galaxies (Elbaz et al. 2011, Reddy et al. 2010; Lee et al. 2010; Wuyts et al. 2012). Also, have some variations in the cluster mass function and stellar initial mass function (IMF, Wilkins et al. 2008; Pflamm-Altenburg et al. 2009).

The SFR calibration can be related to the whole galaxy or in sub-galactic/sub-kpc scale. Normally, the SFR calibration for the whole galaxy attracted more attention than at kpc scales, due the limitations of spatial resolution. Nowadays, with the advent of technology the local SFR calibrations become prominent in the community.

Indicators from direct stellar light

SFR indicators are measures of luminosity either monochromatic or integrated over some wavelength range, with the goal of targeting continuum or line emission that is sensitive to the short-lived massive stars. The conversion from the luminosity of massive stars to a SFR can be performed under the assumption: the star formation is constant over the timescale probed by the specific emission that is being used and the stellar IMF is fully sampled (at least one star is formed in the highest mass range and all the others are populated accordingly with one or more stars). Using this, then we can calculate the following relation between SFR and the luminosity of each indicator.

The relation SFR-Lν considered in this section are all from Murphy et al. 2011. However, how the parameters are not universal, the relations can be different depended of the assumption made from each authors (e.g the IMF and the stellar mass). Kennicutt & Evans (2012) compared the SFR derived with the relations of Murphy et al. (2011) is between 60-70% (for the direct emission) and 85% (for the dust emission) that derived using the relations of Kennicutt (1998) (K98). In this thesis, for every SFR used here the original reference will be cited.

UV continuum

The youngest stellar populations emit the bulk of their energy in the restframe UV ($< 0.3\mu m$). In the absence of dust attenuation, this is the wavelength range perfectly suited to investigate star formation in galaxies over timescales of approx 100-300 Myr. Because O and B stars are brighter in the UV than at longer wavelengths. Extragalactic UV observations were made with the Galaxy Evolution Explores (GALEX; Martin et al. 2006) where, UV-emission can easily be observed at high-redshift and even resolved spatially.

Observations found a linear relation between SFR and FUV luminosity. For example, in Murphy et al., 2011 we have:

$$\left(\frac{SFR_{FUV}}{M_{\odot}.yr^{-1}}\right) = 4.42 \times 10^{-44} \left(\frac{L_{FUV}}{ergs.s^{-1}}\right) \tag{1.15}$$

Optical

In H_{II} regions, the gas re-emits the ionizing stellar continuum via optical recombination lines. We can use then emission from the Balmer series, principally H_{α} or H_{β} : they trace massive stars with short lifetimes. Using these tracers also has a possibility to have high sensitivity and resolution from the optical observation. This relation can be given by:

$$\frac{SFR_{H_{\alpha}}}{M_{\odot}yr^{-1}} = 5.37 \times 10^{42} \frac{L_{H_{\alpha}}}{ergs.s^{-1}} \tag{1.16}$$

At redshifts $z \gtrsim 0.5$ the H_α is no longer observable, therefore we can use the forbidden line doublet [O II], given by the expression :

$$\frac{SFR_{[OII]}}{M_\odot yr^{-1}} = 1.4 \times 10^{-41} \frac{L_{[OII]}}{ergs.s^{-1}} \tag{1.17}$$

This method is an ersatz, since [O II] is more affected by dust attenuation, and less precise than the H_α because there is not a constant [O II]/H_α ratio.

Indicators from dust

The interstellar dust absorbs parts of the optical and UV radiation of the galaxy and re-emits it through thermal IR. The IR emission can thus trace young stellar populations. The IR luminosity of a system will depend not only on its dust content, but also on the heating rate provided by the stars. The relation between SFR and L_{IR} is derived using synthesis models. Murphy et al. 2011 derived a calibration between SFR and IR emission in a specific range from 8 to 1000 μm , where it results in:

$$\frac{SFR_{IR}}{M_\odot yr^{-1}} = 3.88 \times 10^{-44} \frac{L_{IR}}{ergs.s^{-1}}, \tag{1.18}$$

where, L_{IR} is the IR luminosity for each wavelength.

With the multi-wavelength IR observations from *Spitzer* and *Herschel*, we can distinguish two components that exist in mid and far IR (FIR) spectrum: the 24μm (Rieke et al., 2009) and 70 μm (Calzetti et al., 2010). So we have:

$$\frac{SFR_{24\mu m}}{M_\odot yr^{-1}} = 2.03 \times 10^{-43} \frac{L_{24\mu m}}{ergs.s^{-1}} \tag{1.19}$$

and

$$\frac{SFR_{70\mu m}}{M_\odot yr^{-1}} = 5.88 \times 10^{-44} \frac{L_{70\mu m}}{ergs.s^{-1}} \tag{1.20}$$

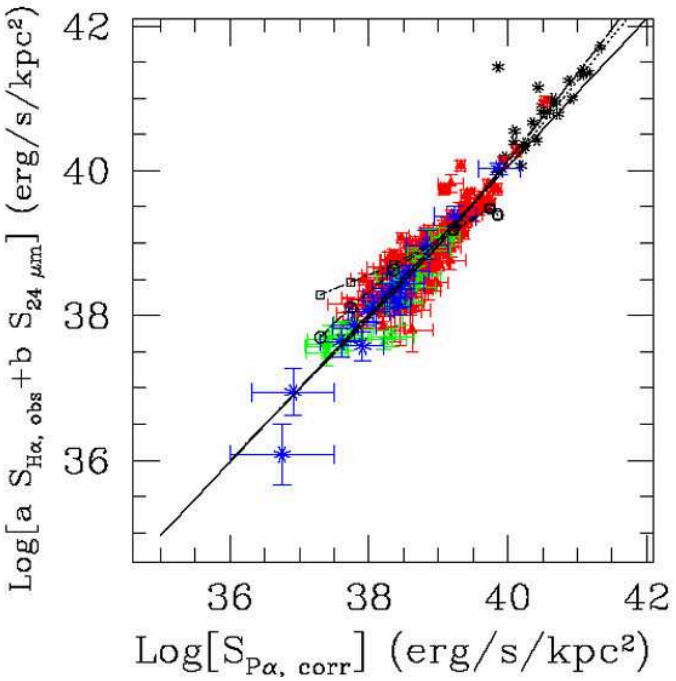

Figure 1.10 – *Example of a mixed SFR indicator. This specific example is for a local SFR indicator: the data points include star-forming regions in nearby galaxies (red triangles, green squares, blue crosses) and local LIRGs (black stars, from Alonso-Herrero et al., 2006). We can see that the relation is linear, indicating no dependency on metallicity and luminosity of the source. Figure from Calzetti., 2007*

Indicators from mixed processes

It becomes necessary to capture both dust-obscured and dust-unobscured star formation. This led to the reformulation of SFR indicators that attempt to use the best qualities of each indicator explained above. Of course, this brings advantages that compensate the problem to have two measures widely separated: one in the stellar light and the other in the dust. From (e.g.) Calzetti et al., 2005, 2007; Kennicutt et al., 2007, 2009; Liu et al., 2011; Hao et al., 2011 we can normally express SFR by:

$$\left(\frac{SFR(\lambda_1,\lambda_2)}{M_\odot yr^{-1}}\right) = C(\lambda_1)\left(\frac{L(\lambda_1)_{obs}}{ergs.s^{-1}} + \alpha_{\lambda_2}\frac{L(\lambda)_{obs}}{ergs.s^{-1}}\right) \tag{1.21}$$

The $SFR(\lambda_1,\lambda_2)$ is usually a tracer probing either direct stellar light and dust emission from each wavelength range λ_1,λ_2. The constant $C(\lambda_1)$ is the calibrator for the direct light probe, often from synthesis models. The luminosities $L(\lambda_1)$ and $L(\lambda_2)$ are the observed luminosities. The proportionality constant α_{λ_2} depends both on dust emission tracers used in a whole galaxy or in kpc-scale regions. A remarkable example of this is shown in the figure 1.10 where is displayed a relationship between the luminosity of Paschen$_\alpha$ with the luminosity/area of the observed H$_\alpha$ and 24 μm luminosity, in different regions of a given galaxy.

Star formation Efficiency

It is common to characterize the superficial density of star formation rate in a galaxy, either globally or locally, in terms of the SFR formed per area ($\Sigma_{SFR} = SFR/area$). Quantitatively, it is useful to estimate the gas consumption time-scale (or depletion time), through the relation between the SFR and the gas surface densities $\tau = \Sigma_{gas}/\Sigma_{SFR}$. The gas depletion time is also the inverse of star formation efficiency. This kind of expressions helps to derive the main principles that could describe Σ_{SFR} as a function of physical conditions. Empirical star-forming laws are based on the ISM properties. Scaling relations can give us useful insights into the physics underlying the star formation, i.e. knowledge about density, temperature or metallicity of the gas in the ISM.

Another important uncertainty concerns the molecular gas density. The surface density of molecular hydrogen, Σ_{H_2}, is determined from the integrated CO intensity (I_{CO}), intrinsically related to the CO-to-H_2 conversion factor.

Kennicutt-Schmidt relation

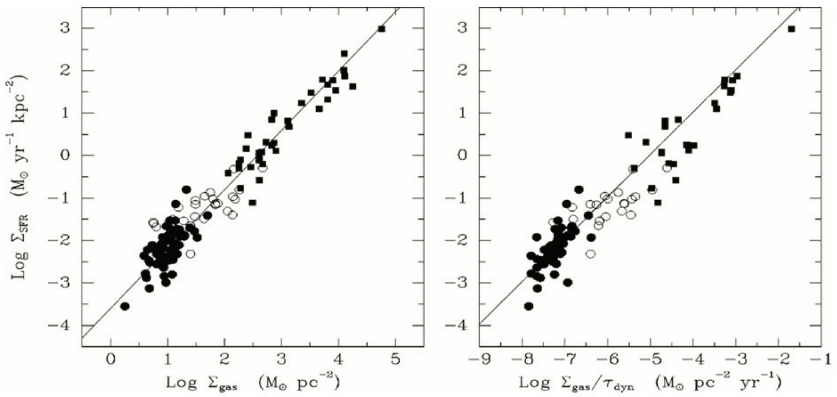

Figure 1.11 – *K98 found that in a sample of 100 nearby galaxies could fit with the law founded by Schmidt (1959). He examined the connection between the molecular gas density with SFR and he estimated the* $n = 1.4\pm$ *0.15*

The first study about an empirical relation of star-formation, started in 1950's with (Schmidt, 1959). He derived the SFR over the MW history, assuming a constant initial luminosity function of stars $\Psi(M_v)$, a stellar lifetime function $T(M_v)$. He assumed that the SFR volume density ρ_{SFR} depends essentially on the gas volumic density. When the stellar mass loss and the gas return equals to 30% of the stellar mass, and also the SFR function $f(t)$ is a power law of the gas mass (M_g), then we have:

$$f(t)\Psi(M_v)\Sigma_{MV} = C[M_g]^n \tag{1.22}$$

where $C[M_g]$ is for all stellar types. Schmidt (1959) analysed different values for n. Adopting a scale height for HI of 144 pc, a scale height for Cepheids of 80 pc, and a scale height for clusters of 58 pc, the values of n are n = 2 to 3. When he considered the white dwarfs, he then found $n > 2$. For the HI gas, higher values of n are found, $n \geqslant 2$ and for the stellar cluster masses $n = 1$ to 2. (Schmidt, 1959) suggested to use for the dense galaxies $n = 2$; they have now less gas than low-metallicity galaxies like the LMC. Concluding his work we have then:

$$\rho_{SFR} \propto (\rho_{gas})^n \tag{1.23}$$

The relationship between these two quantities can characterize the efficiency at which a galaxy transforms its gaseous reservoir into stars.

After his study, many authors derived scaling relations between the average surface density of star formation and the average surface density of gas. K98 extended such analysis including starburst galaxies. He used H_α for star formation, and HI and CO for the gas with a constant H_2/CO conversion factor. He could determine SFR as a function of galactocentric radius and also average over the whole galaxy disks. For whole galaxies, the average SFR surface density varies with the average gas surface density as a power law, with slope between 1 and 2. The simple Schmidt law gives a surprisingly good parametrisation of the global SFR over a surface density range.

Kennicutt's work established that the SFR had an abrupt cutoff in radius where the stability condition (Toomre Q) indicates a gravitational instability in the gas. He derived the existence of a threshold in gas column density for star formation. The Kennicutt-Schmidt (KS) law is often interpreted as indicating that the star formation rate is controlled by the self-gravity of the gas. K98 found that for normal galaxies, the slope of the SFR-surface density relation ranged between 1.3 and 2.5, depending on how the slope was measured. If all galaxies have the same scale height, this implies that

$$\Sigma_{SFR} \propto \Sigma_{gas}^n \tag{1.24}$$

is in good agreement with the empirical relation, see left-hand panel from figure 1.11. The value for n is still in debate. Around 2008, the popular KS law had a slope of around 1.5, when the SFR density was plotted versus total gas column density in a log-log scale (e.g., Leroy et al., 2008; Bigiel et al., 2008). This was interpreted with a dynamical model for star formation in which the SFR/area is equal to the available gas mass per area and divided by the free-fall time, i.e. proportional to the rate at which the gas mass is converted into stars. If the gas scale-height is constant, then $\Sigma_{SFR} \propto \Sigma_{gas}^{1.5}$. This could only work if the Toomre instability condition is satisfied ($Q < 1.4$). This was supported by some computer simulation (e.g., Li et al., 2006; Kravtsov, 2003)

K98 shows that the data reveal a proportionality between Σ_{SFR} and Σ_{gas}/τ_{dyn} (see the right-hand panel from 1.11). Here τ_{dyn} is defined as $2\pi R/V(R)$ the orbital time at

the outer radius R of the star-forming regions. In Silk (1997) a star formation law follows naturally in models where the star formation is self-regulated in discs that maintain $Q \sim 1$. However, this is not the only explanation: the SFR can be governed by the rate of gravitational collisions between clouds, or some models show that the spiral arms play an important role for the trigger of star formation, for example.

Hunter et al. (1998) using dwarf Irregular galaxies get a critical surface density lower than K98. This tends to imply that dwarfs have more stable gas than spirals. Boissier et al. (2003) with a sample of 16 resolved galaxies, have their best fits as $n = 2.06$. They assume that H_2/CO varies with radius and is metallicity-dependent, the same way as in Boselli et al. (2002). They tested three types of star formation laws: the Schmidt law, $\Sigma_{SFR} \times R/V(R)$ and SFR density versus $\Sigma_{gas}^{n}\Sigma_{T}^{-0.61}$ (the Dopita-Ryder law from Dopita & Ryder (1994)). They concluded that they find only small differences among them and all three star formation laws match observations in the Milky Way disc. They also conclude that the Σ_{crit} (considering gas+star) is the best threshold for determining where star formation occurs.

Zasov & Smirnova (2005) showed that the existence of a threshold like Σ_{crit} makes it possible to determine the gas fraction in galaxies. If the galaxies have Σ_{HI} approximated at the critical $\Sigma_{crit}\kappa\sigma/\pi G$, a priori proportional to V/R as is κ, then we can calculate $M_{gas} = \int 2\pi R\Sigma_{crit}dR \propto VR$. They also consider that $M_{tot} \propto V^2R$ and then $M_{tot}/Mgas \propto V$. They concluded that small galaxies are more gas rich than large ones; this occurs since all galaxies have their gas column densities close to the surface density threshold.

Depletion time

Studies showed that the relation between Σ_{SFR} and Σ_{gas} is well expressed by a single power law (e.g., Kennicutt, 1998; Bigiel et al., 2011; Schruba et al., 2011a). The figure 1.11 show that the slope is sharper at low gas surface densities. This can be explained because the gas is mostly atomic at low density. In the molecular phase, the relation is linear, while it is much steeper for the atomic gas.

A linear relation between the SFR and molecular gas surface densities means a constant star formation efficiency, which can also be described in terms of a constant depletion time. The depletion time is the inverse of the star formation efficiency, namely

$$\mathrm{t_{depl}} = \frac{1}{\mathrm{SFE}} = \frac{\mathrm{M_{gas}}}{\mathrm{SFR}}, \tag{1.25}$$

which corresponds to the time needed for the gas reservoir to turn into stars completely, at the present SFR. The average molecular depletion time,for local galaxies, is about 2 Gyr (e.g., Bigiel et al., 2008, 2010; Leroy et al., 2013). When the atomic phase is saturated and the excess gas is found in the molecular phase, then normally the surface density is 9 $\mathrm{M_{\odot}pc^{-2}}$. This is the inflexion found in the KS relation. Also, the KS relation has a scatter of about 0.2 dex, due to different evolutionary stages of molecular clouds (e.g.,

Lada et al., 2010; Lombardi et al., 2010; Zamora-Avilés et al., 2012; Zamora-Avilés & Vázquez-Semadeni, 2014; Utomo et al., 2015).

Daddi et al. (2010) found two regimes for star formation: the starburst galaxies are forming stars much more efficiently than the spiral ones, by a factor of 5-10. This could be due to the different conversion factors (α_{CO}) used for the two galaxy classes, different by a factor 6. It is of interest to note that this large variance of the α_{CO} is still a matter of debate. It is still possible to use a conversion factor continuous between the two limits $\alpha_{CO} = 0.8 - 4.6 M_{\odot}(K.km.s^{-1}.pc^{-2})$. For example, Narayanan et al. (2012) does not find the bimodality claimed in Daddi et al. (2010) .

In a study evaluating the variation of the molecular depletion time with redshift, Tacconi et al. (2013) also support different depletion times, as in Daddi et al. (2010). The star formation efficiency depends on the molecular gas mass reservoir within a galaxy, being more efficient for galaxies with a high gas fraction. This could be due to the existence of gas inflows that fuel galaxies periodically, maintaining the star formation activity.

Molecular star formation law

The star formation law is a relation between the SFR and the total gas (HI+H_2) surface densities, as a power-law with index of $n = 1.40 \pm 0.15$ in nearby galaxies. Wong & Blitz (2002) found an SFR varying linearly with the molecular gas density and suggests that the $n = 1.4$ KS law came from changes in the molecular fraction ($f_{mol} = \Sigma_{H_2}/\Sigma_{H_2} + \Sigma_{HI}$).

Fitting individual KS laws to individual galaxies yields best-fit values for n. Bigiel et al. (2008) studied 18 nearby galaxies, as can be seen in figure 1.12. The bottom-right panel shows that the Σ_{SFR} is poorly correlated to Σ_{HI}. The Σ_{SFR} covers three orders of magnitude, for less than one in Σ_{HI}. Hence, Σ_{HI} cannot be used to predict the local star-formation rate surface density. The bottom-left panel of figure 1.12 shows the contrary: a relatively well-defined KS relation for molecular gas. Bigiel et al. (2008) find $\Sigma_{SFR} \propto \Sigma_{H_2}^{1.0\pm0.2}$. The fact that the power law is close to unity implies a roughly constant star-formation efficiency. This suggests that the KS law between Σ_{SFR} and the $\Sigma_{gas_{total}}$ is actually an mixture from two regimes: the first is governed by the transformation of atomic to molecular gas and the second describes the turn of molecular gas into stars. This allows to understand the local KS law from the top panel of figure 1.12, since in the central regions of disk galaxies the gas is largely molecular.

In enviromment with low mettalicity, the SFE is low compare with central regions of disk galaxies, e.g dwarf galaxies and outerdisks (actually, dwarf galaxies are very similar to the outer parts of spirals in the Bigiel et al. (2008) sample). Elmegreen & Parravano (1994) suggested that the SFE in the outer parts of disk galaxies drops because of the pressure that becomes too low for the molecular phase to form. This may explain the star-formation threshold. This is not the only explanation however, the first one being the gravitational instability, and the critical velocity dispersion under which the gas turns unstable.

Leroy et al. (2008) compared the new survey results (like GALEX, Spitzer etc) to various models. They found that the depletion time is around 1.9 Gyr and is independent of the average local free fall time, the mid plane gas pressure and the gravitational stability of the disk. They showed that the KS is linear with stellar surface density and interstellar pressure and has an inverse squared dependence on the free fall time. It has also an exponential dependence on the galactic radius, which is the same for the rest of the disk, when compared with the radial scale length. Leroy et al. (2008) concluded that the $HI - H_2$ transition in spirals occurs at $0.43 \pm 0.18 R_{25}$ when $\Sigma_{SFR} = 81 \pm 25 M_{\odot} pc^{-2}$ and $\Sigma_{gas} = 14 \pm 6 M_{\odot} pc^{-2}$.

Comparing models with the results from Bigiel et al. (2008) and Leroy et al. (2008) shows that the theory for molecule formation in a galactic environment fits the observations Krumholz et al. (2009); Krumholz (2013).

What controls SFE

In the understanding of star formation, an important question arises: What causes the overall star formation efficiency in normal disks to be so low?

A possible solution is in terms of the angular momentum that can prevent the gas from collapsing to the center of the potential well and acquire high densities. This actually could distinguish disk galaxies from starburst galaxies. Because of some merger or close encounter, starbursts have their angular momentum removed from the gas, allowing to accumulate gas at the center and to form stars with higher efficiency. However this is not the only reason.

Magnetic Fields

Magnetics fields can be an important source of support against gravitational collapse for molecular clouds. We can then consider that the SFE is regulated also by magnetic fields.

The magnetic support can diminish through the ambipolar diffusion (Spitzer 1956). In a GMC which contains ionized and neutral particles, the neutral population is only indirectly coupled to the B field through collisions with the ionized population. When the ionized fraction is low, the collisions between neutral particles and ions become insufficient to couple the neutral and ionized gas. Then the neutral particles can diffuse through the magnetic field. In this way, the magnetic flux is reduced in the gas. The ambipolar diffusion time scale, τ_{ad} can be calculated from Elmegreen et al., (1979):

$$\tau_{ad} \simeq 1.1 \times 10^8 yr \left[\frac{n}{100 cm^{-3}}\right]^{1/2} \left[\frac{R}{10 pc}\right]^{3/2} \left[\frac{B}{30 \mu G}\right]^{-1} \tag{1.26}$$

which means that ambipolar diffusion is effective when the τ_{ad} is lower than the lifetime of GMCs, which is not the results found so far.

Turbulence

The gas cloud collapse can be affected by turbulence. The turbulent motion can increase the effective velocity dispersion of the gas, delaying or even suppress the gravitational collapse. Also, in a turbulent medium the gas can be swept and compressed by shocks trough the supersonic flow. This turbulence can trigger gravitational collapse increasing the gas density.

Self-regulation

The feedback includes the formation and expansion of stellar winds, supernovae and the HII regions (due to the ionization and heating by UV photons from massive stars). This process can produce some negative feedback on star formation itself. The feedback destroys molecular clouds and hence regulates the SFE.

Stellar feedback can cause the disruption of an entire GMC. The typical lifetime of a GMC is $\sim 10^7$yr, shorter than a typical age of a galaxy. In some cases, the feedback from massive OB stars can destroy the GMCs where they are placed.

In some studies about the SFE control suggest that the dominant destruction mechanism is probably the photoevaporation by HII regions (e.g. Williams & McKee, 1997; Krumholz et al., 2006).

Star formation may heat the ISM, increasing the velocity of the gas which make the disk stable against the gravitational collapse. This type of self-regulation has been invoked by Silk (1997) in order to explain why disk galaxies seem to have a Toomre parameter $Q \sim 1$ over the extent of the disk in which star formation is prevalent. When Q falls below 1, gravitational instabilities form clumps and increase the velocity dispersion, until Q$\sim$ 1 again.

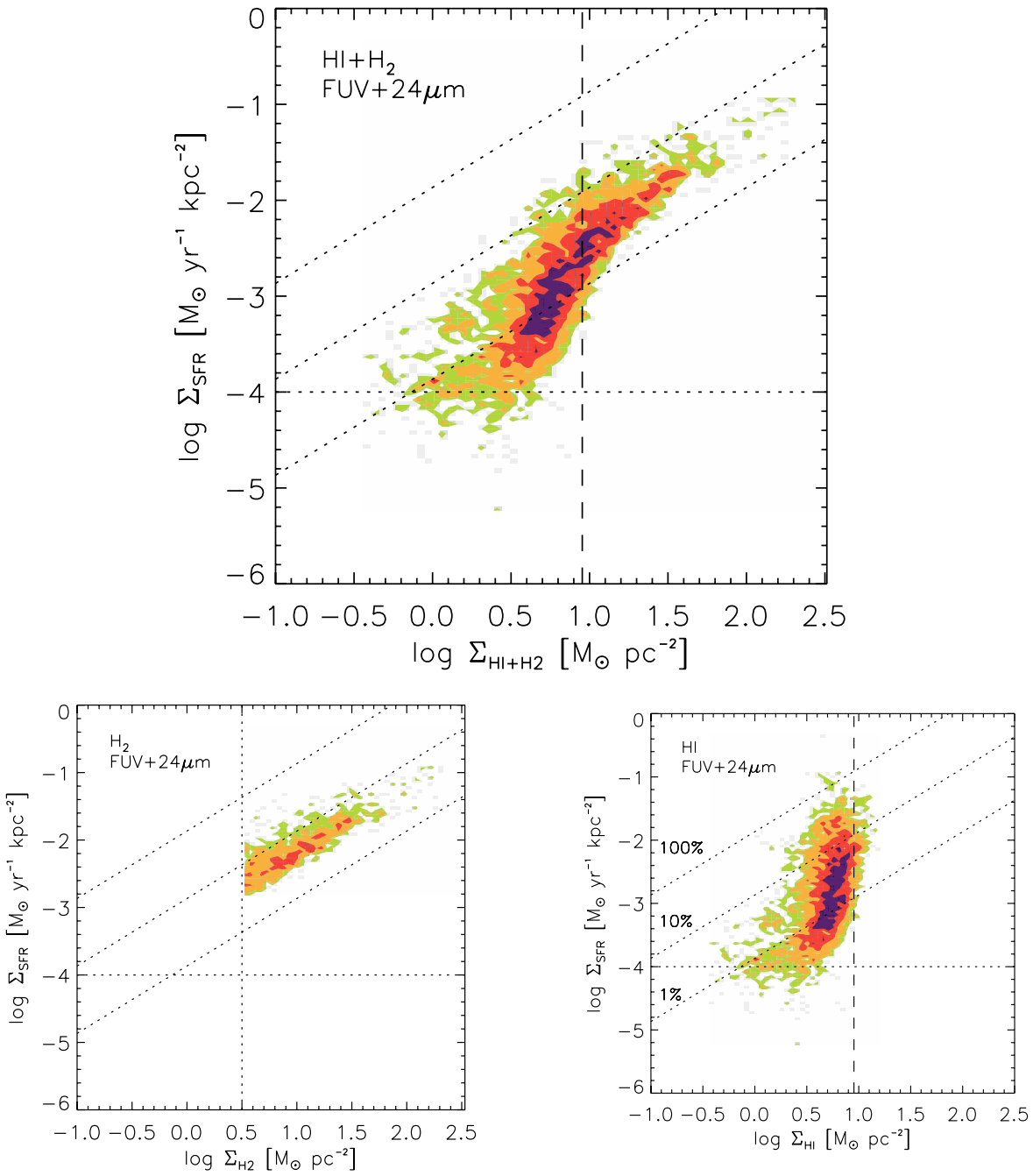

Figure 1.12 – *Local star-formation rate per unit area (measured on a scale of 750pc) as a function of the local atomic gas density (left-hand panel), molecular gas density (middle panel), and total gas density (right-hand panel). The grayscale is proportional to the number of independent data points (resolution elements) obtained from a sample of 18 nearby galaxies. The diagonal dotted lines show lines of constant star-formation efficiency, indicating the level of SFR needed to consume 1%, 10% and 100% of the gas reservoir (including helium) in 10^8 yr. Dashed vertical lines in the left and right panels show the surface density at which HI saturates. The dotted vertical line in the middle panel indicates the typical sensitivity of the CO data used to infer the molecular gas densities.*

Part One

XUV Disk Galaxies

CHAPTER 2

XUV disk galaxies

Over the last decades XUV disk galaxies have gained interest. Gil de Paz et al. (2005) show the presence of UV-bright complexes in the outermost of some galaxy disks. These are called XUV disk galaxies, hosting UV emission well beyond their optical radii. UV-bright disks extending up to 3 to 4 times their optical radius (R_{25}) have been reported in about 30% of spiral galaxies (Thilker et al., 2007; Gil de Paz et al., 2007b). Their extended UV emission covers a significant fraction of the area detected in HI at 21 cm wavelength (Bigiel et al., 2010; Boissier et al., 2007; Zaritsky & Christlein, 2007). Generally, the UV star-formation (SF) is related with this extending HI structure, e.g. shows evidence for metal enrichment (Gil de Paz et al., 2007a). Their far ultraviolet (FUV) and near ultraviolet (NUV) colours are generally consistent with young populations of O and B stars which probe a wider range of ages than H_α and at low SF levels the number of ionizing stars may be very small (Dessauges-Zavadsky et al., 2014; Boissier et al., 2007; Thilker et al., 2007). The corresponding age for FUV regions is 10-100Myr, and for H_α regions, 3-10 Myr.

Studying star formation beyond the optical radius allows us to address the condition of low-metallicity environments (Bigiel et al., 2010) . The KS relation is almost linear when most of the gas is molecular, providing a constant gas consumption time-scale of about 3Gyr (e.g Bigiel et al. (2011); Saintonge et al. (2011)). The SFE falls very quickly when the $\Sigma_{gas} < 10 M_\odot/pc^2$,i.e when the gas is mainly atomic. However, recent surveys of molecular gas at high resolution have the sensitivity to probe this relation at $\Sigma_{gas} \lesssim 3 M_\odot/pc^2$. Studies of SF beyond the optical radius primarily concentrated on comparing different SF tracers. Until now studies of SFE in XUV disk was principally focused on atomic gas. These environments are not propitious to H_2 formation due to the low gas density and low metallicity conditions, which are akin to galaxies in the early universe.

The confirmed occurrence of star formation in the outer disk of normal spirals has several important implications: it indicates the presence of molecular gas in the outskirts of spirals, possibly an efficient phase transition from HI to H_2. It is a good place to study the unresolved issue of the atomic hydrogen gas origin, and it provides a simplified

laboratory for determining the star formation threshold. It is also the place to investigate the star formation in quiescent and low-metallicity environments that may affect the SFE and the initial mass function.

Extended discs

The surface density of gas in spiral galaxies is generally an excellent tracer of the surface density of star formation. K89 tested the hypothesis that the Toomre stability criterion determines the gas density threshold for star formation, using the radial distributions of HII to trace the SFR. He found that there exists a drop-off in star formation at high radii. This SF truncation in outer disks occurs when the disks are unable to form stars below a critical gas density (e.g figure 2.1 showing such a truncation in M83). There is then a star formation threshold in Hα emission (Martin & Kennicutt, 2001).

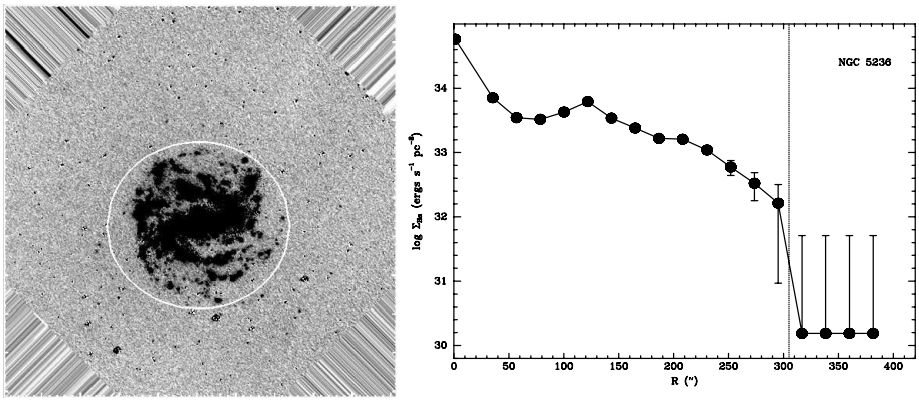

Figure 2.1 – *M83 truncation in star formation: Hα image at left, and radial distribution of the Hα flux, versus radius in arcsec, taken from Martin & Kennicutt (2001).*

Most studies until now showed that HII regions are quite abundant in the inner regions of galaxies or within their optical radius, R_{25} (defined by the B-band 25th magnitude per arcsec^2). Also, from HI studies in the 1990's, it is well known that atomic hydrogen is much more extended radially in galaxies, typically $\sim$ 1.5-2 R_{25} (Cayatte et al., 1994). These galaxies showing an extension of HI after the optical disk, are commonly referred to *extended HI disk* galaxies. These extended gaseous disks are peculiar environments, without much stellar recycling, and a perfect opportunity to study the star formation laws. They have physical properties with some similarity with the conditions prevailing in the early stages of galaxy formation. Ferguson et al. (1998) detected for the first time Hα emission in outer disks in three spiral galaxies, NGC628,NGC1058 and NGC 6946. They have determined their chemical abundances in the range 9%-15% solar for O/H and 20%-25% solar for N/O, at 1.5-2. R_{25}. The radial abundance gradients in the gas is compatible with a single log-linear relation, i.e. implying an exponential decrease of heavy elements. From simple closed-box chemical models, they conclude that the observed abundances require radial gas flows. The amplitude of these gas flows are similar in the outer disks of their sample to those in the solar neighbourhood. They also imply that the outer disks are relatively unevolved systems.

Two years later, Lelièvre & Roy (2000) study one of the galaxies in Ferguson et al. (1998), NGC 628. They focused on the SFR determined from the Hα flux and on its

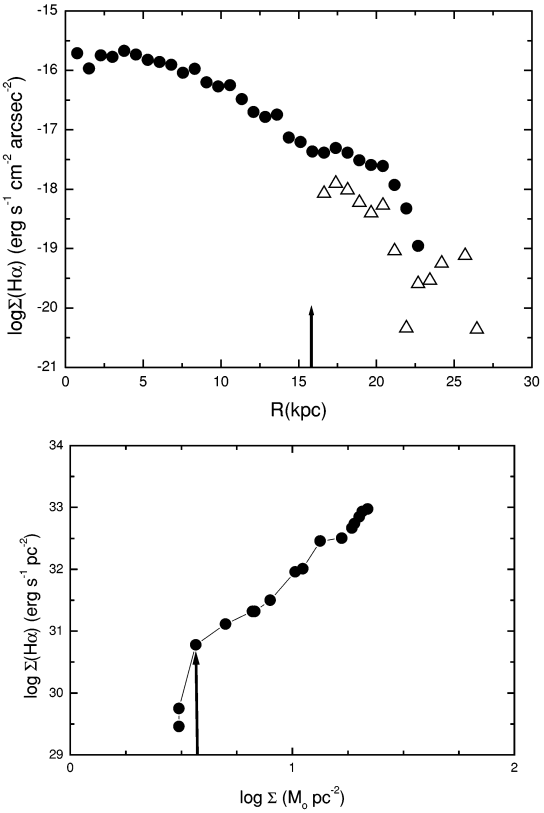

Figure 2.2 – *Top: Surface density of Hα versus radius (the arrow indicates R_{25}), and Bottom: Schmidt law, i.e. surface density of Hα flux versus the surface density of gas, sum of HI and H_2 derived from CO, from Lelièvre & Roy (2000).*

relation to the gas density, which was called "Schmidt relation" at this epoch (see figure 2.2). They were the first to study the star formation law in the outer disks. The figure 2.2 shows that the means Hα surface brightness decreases exponentially as a function of galactocentric distance until R_{25} (they have difficulties to ascertain the radial change at R$\sim$20kpc, because of the flat-fielding and background subtraction). Their Schmidt law "fails" (expression used by the authors) at $\sim$4 $M_\odot$ pc^{-2}: They interpret this drop in terms of molecular cloud cores being photodissociated by UV radiation.

Later, two more extreme outer disks in two spirals were studied: **M31** where evidences for B stars are found in the outer parts (Cuillandre et al., 2001) and **NCG6822** which reveals the presence of numerous blue, young stars (de Blok & Walter, 2003). The same density and physical conditions are found in certain dwarfs (van Zee et al., 1997), where are also observed some populations of blue stars with ages $\lesssim$ 100Myr. For the HII regions of NGC628, NGC 1058 and NGC 6946 the luminosity function become steeper at R$\sim$$R_{25}$ compared with the galaxy-wide sample.

The *Galaxy Evolution Explorer* (GALEX) revealed an extensive sample of UV-bright sources in the extreme outer disk of some galaxies. Thilker et al. (2005) (T05) presented far-UV (FUV) and Near-UV (NUV) wide-field GALEX images revealing an extensive population of star-forming regions in the M83 outer disk. This discovery has a significant

importance in contrast to Hα observations which fail to detect a significant amount of moderate-age star clusters. This gives more credibility to the discussion made by Ferguson et al. (1998) about chemical enrichment, magnetohydrodynamics (MHD) processes in galaxies disks (Sellwood & Balbus, 1999), ISM phase balance (Allen et al., 1986; Thilker et al., 2005). T05 argued that the B stars traced by GALEX could drive some feedback mechanisms.

In the same year, Gil de Paz et al. (2005) (GP05) study the same issue than T05 with NGC 4625. They find that these galaxies have some "puzzlings" properties due to the fact that even the extended UV disks are truncated at some radius. The same truncation was studied by K89 and MK01. That is not the case for NGC4625, where the Hα emission could be detected very far out in the disk, even at faint levels. Since then, extended ultraviolet disks have been found in many galaxies, these structures are now commonly termed extended UV discs (XUV disks).

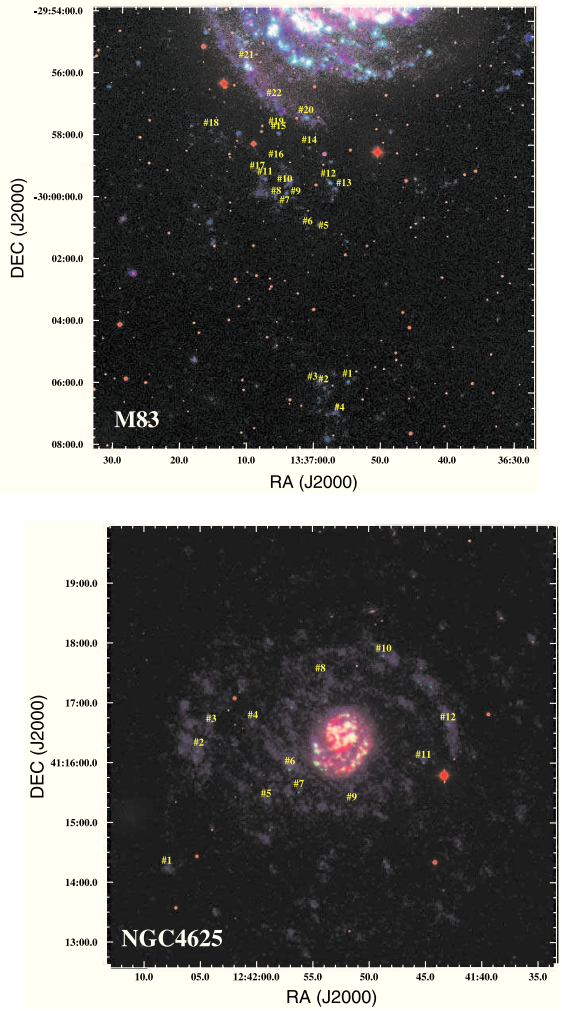

Figure 2.3 – *Extended UV disks in M83 (top) and NGC 4625 (bottom) from Gil de Paz et al. (2007b). The RGB image is a superposition of FUV (blue), Hα (green) and U-band (red). The Hα regions in green are indicated by numbers*

In continuation of this study, Gil de Paz et al. (2007b) made a comparison between

the Hα emission and UV in M83 and NGC4625 (see figure 2.3). They concluded that the ionizing radiation of this galaxies comes from young stars and the amount of gas in these XUV disks is enough to maintain the star formation level. Also, it is likely that the extended HI associated to the XUV disk (corresponding to only 10% of the HI disks, according to the authors) is a consequence of H_2 photodissiociation in PDRs (without H_2 the ratio A_{HI}/A_{FUV} would be smaller).

Since Ferguson et al. (1998), many observations have studied star formation in the outer disks of some local galaxies. One of the main issues is to determine whether the star formation in outer disks has different laws compared to the rest of the disk. The understanding of the star formation in these galaxies requires the mapping of the molecular component. In this Chapter of my thesis I will discuss the molecular gas in one galaxy of this kind, i.e. M83 with ALMA data.

Morphology and classification

In hierarchical models of galaxy formation, disks structures are predicted to regrow after some merger experiences (Steinmetz & Navarro, 2002; Governato et al., 2010). There are some indications that could possibly indicate that these extended UV disks are in reality extensions of the inner disk: Christlein & Zaritsky (2008) report that the UV knots in the outer disks are dynamically cold and rotating. Bush et al. (2008) found from simulations that the inner disk material propagates to the edge of the extended disk. These outer disks have peaks from spiral waves when gas density is above some threshold. In M83, UV knots are found extending to 4 R_{25}, and are associated with large-scale filamentary H I structures.

The UV emission in the outer disks are found most often in high-mass bulge-dominated galaxies, according to Kauffmann et al. (2007). These bulge-dominated galaxies are normally associated with large cold gas reservoirs, helping the growth of central black holes. There are also some propositions that the outermost disks could form through minor perturbations (Thilker et al., 2007). These interactions or gas accretion from fresh cosmic material could be consistent with the extended disks of HI, observed commonly in E/S0s types (Morganti et al., 2006; Oosterloo et al., 2007). Moffett et al. (2012) argues that XUV disks occur in a different range of mass in the blue and red sequence of galaxies. They suggest this comes from galaxy interactions or mergers. They propose that UV-B disks favour the blue sequence because of the cold-mode gas accretion or another mass-dependent evolutionary process. Indeed, many galaxies show a decline in the radially average SFR per unit area, where the disk becomes dynamically stable. The interactions may disturb the gas, triggering its collapse to form stars (this was proposed also by G05 for NGC4625 interacting with its neighbour NCG4618).

The two hypotheses can be debated: is SF at large radii linked to the inner disk or is it due to some outside perturbation? To better understand the properties of XUV disks, they have been classified. The first classification was made by Thilker et al. (2007), mainly in two types:

- Type I "show structured, UV-bright emission complexes beyond the anticipated location of star formation threshold" ($\gtrsim$ 20%). Sometimes they are referred like "M83-like".
- Type II "have bulge colour (FUV-NIR) within an exceptionally large,outer, and optically LSB portion of the disk" ($\sim$10%).
- They also consider a mixed-type where some objects possess the two characteristics

Using this classification scheme, they found 54 XUV-disk galaxies from 189 targets. This means that this kind of SF in disks is a common process in galaxy evolution. Goddard et al. (2010) found four extended galaxies in their sample that exhibit a smooth profile beyond the truncated edge. Observation in Far-Infrared also suggest that the dust detected is not primordial, i.e. it was transported from the optical disk or it must have been produced outside of the galaxy (Popescu & Tuffs, 2003). Thilker et al. (2007) also tried to find some evidence for interactions, using the perturbation parameter, f. With its limitation, they find some minor perturbations for type-I, but still this hypothesis requires confirmation. These perturbations could naturally accompany galaxy growth and gas accretion could trigger the XUV-disk formation. There are some given examples showing clearly the presence of minor external perturbations, but how much this could make a difference in SF in the outer disks? Or maybe these perturbations could just be a source to stimulate the SF in an environment already quiescent?

Star formation in the outer disk

The SF threshold in low-density environments has been studied already for almost thirty years. The typical gas surface density in these regions is less than 10 $M_\odot$ pc^2, and the gas is mostly atomic. These regions can be found in the outer disk of spirals, early-types, low surface brightness and dwarf galaxies. However, recent star formation was found in the outer disks of some galaxies, and *GALEX* could also detect a significant population of star clusters. M83 is considered the prototype of the XUV galaxies, with some recent stars formed far from the center. Normally, in disk galaxies the HII regions decline abruptly at R $>R_{25}$. The figure 2.4 shows the example for M83 (figure from T05), where there exists emission in NUV, FUV and HI when R$>$ 6.6kpc. The decrease of Hα implies less recent star formation rate at large radii. There exists only a few recent stars (10Myr), but the UV emission is due 100 Myr stars (Gil de Paz et al., 2007b).

Star formation might be truncated due to a gas volume density threshold (e.g., Martin & Kennicutt, 2001; Pflamm-Altenburg & Kroupa, 2008): these truncations are easily seen when obtaining an average Kennicutt-Schmidt law in SPH simulations (Bush et al., 2008, 2010). Sometimes this truncation corresponds to Hα observation, but not for all the extended disk galaxies (e.g., Goddard et al., 2010). Some outer disks have still high SFRs, due to their gas richness. If the star formation occurs above the critical density defined by the Toomre criterion for dynamical instability, then the outer disks can follow a Kennicutt-Schmidt law. Dong et al. (2008) find some recent star formation in the XUV

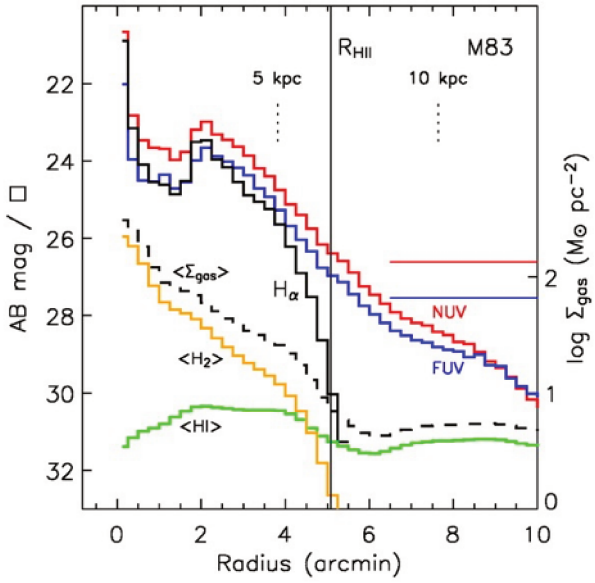

Figure 2.4 – *The M83 radial profilesof the median FUV (blue), NUV (red), and Hα (black) surface brightness, plus average surface densities derived from HI (green) and CO (orange) data. Azimuthally averaged gas surface density is shown with a dashed line. The vertical line indicates the last radius of HII regions. The difference between the Hα and UV profiles is remarkable. From T05*

disk of M83 with SPITZER, each time the HI density becomes higher than the threshold locally. Studing a sample of 43 galaxy disks, XUV or not, Boissier et al. (2007) find that the SF is compatible with a smooth KS relation. The Hα sudden break in XUV disks is not a change in the star formation regime, but is due to a very small number of ionizing stars corresponding to low levels of star formation. The same happens in SPH simulations, where Bush et al. (2010) found truncations in the azimuthally averaged KS relation.

One of the XUV properties is that they are always found with the *extended HI disk*. This is natural, since gas is the principal ingredient for star formation and newly born stars are responsible to the UV emission . Another point of view is to consider the HI gas as the product of UV-dissociation of the molecular gas. The *extended HI disk* could be a consequence of the UV emission, where H_2 is dissociated by the UV emission of newly formed stars in the PDRs (e.g., Allen et al., 1986).

Even though the cold gas in this regime is predominantly atomic, small and local concentration of molecular gas can sometimes be found. The SFE in these places is very low and seems to be uncorrelated with the gas density, where the SFR has much larger dynamic range than the local density (Bigiel et al., 2010, 2011).

Importance

What is the impact of XUV-disk galaxies through cosmological time and what are their consequences for galaxy formation?

The star formation at large radii usually is only a small fraction of the SF of the entire galaxy, but offers a different perspective to analyze the physical processes that hold the entire star formation. The knowledge about metal enrichment distribution versus radius in galaxies shed light about their evolution. Why do extended UV galaxies show the typical truncation visible in Hα and not other spiral galaxies, and why there is no truncation with UV emission? The XUV disks are also important to verify and understand the star formation threshold in galaxies. One has already discussed that HI emission is normally associated to the extended disks, even before they were called *extended HI disk*. The nature of atomic hydrogen gas origin has been debated: HI might be the result of photodissociation of H_2 by UV flux radiation emanated from newly formed stars (Allen et al., 1986). The relationship between HI and UV is important to measure the efficiency to form stars. Bigiel et al. (2010) concluded that the surface density of star formation traced by FUV emission decreases faster than the surface density of gas. More studies about the SF efficiency in this kind environments could help to solve this issue.

In particular, the molecular gas, not just the atomic gas, should be studied, since molecular clouds are the site of star formation. The presence of stars in the outer disks suggests large reservoirs of H_2. These reservoirs could contribute to the dark baryons still searched for in spiral galaxies (Dessauges-Zavadsky et al., 2014). The detection of CO in this environments is still difficult: CO emission lines are weaker when located in environment with low temperature, low metallicity, low density and low excitation (Combes, 1999)

Extreme environments are often analyzed to check the variation in the stellar IMF. The formation of massive stars sometimes are suppressed in low-density environments. XUV disks represent low gas surface density environments where the stellar initial mass function (IMF) might be truncated at masses below 10 $M_\odot$ (Pflamm-Altenburg & Kroupa, 2008; Meurer et al., 2009). Therefore, the study of star formation in the outer disks could provide some light on these questions.

Molecular gas in XUV disks galaxies

Star formation in disks at low gas surface density, less than 10 $M_\odot$ pc^{-2}, is not very well known. The SFE in these regions is very low and seems to be uncorrelated with Σ_{gas}: SFR has a much larger dynamical range than the local surface density (Bresolin et al., 2009). CO observations in such environments are rare, due to the weakness of the emission. A robust, quantitative picture of how the environment in the outer disks affects star formation is crucial to understand the origins of galaxy structure. Dessauges-Zavadsky et al. (2014) were the first to study molecular SFE in an XUV disk, M63, where

they detected CO(1-0) in 2 of 12 pointings using the IRAM-30m. The authors concluded that the molecular gas in those regions has low SFE compared to regions in the inner disc. Measurements of the gas consumption time-scales in the outer disks for different galaxies provides hints on the star formation over cosmic times. Molecular gas in outer disks, beyond R_{25} were studied in just a few galaxies: in addition to M63 (Dessauges-Zavadsky et al., 2014), NGC4414 (Braine & Herpin, 2004), NGC 6946 (Braine et al., 2007), M33 (Gratier et al., 2010), NGC 4626 (Watson et al., 2016), NGC628, NGC3344 and NGC2403 (Celia Verdugo thesis's). NGC628, NGC3344, NGC2403 and NGC4625 has been actively searched for CO emission but not detected.

The case of M83

Figure 2.5 – *This M83 image in the visible light has been taken with the Subaru telescope (note the pink HII regions). Several images of M83 were taken also with the European Southern Observatory's Wide Field Imager camera, and the Hubble Legacy Archive.*

M83 or NGC5236 is a beautiful face-on galaxy which lies a mere twelve million light-years away near the southeastern tip of the constellation hydra. This galaxy is sometimes called the "Southern Pinwheel". M83 is not just a magnificent example of spiral galaxy, but also for his history in astronomy. M83 was discovered by Nicholas Louis de Lacaille at the Cape of Good Hope on February 23 in 1752, at that time was considered like Lacaille I.6. Thus it became the first galaxy to be discovered beyond the Local Group, and the third of all the galaxies. It was on February 17 in 1781 cataloged by Charles

Table 2.1 – *M83 observations*

	Values
R.A (center)	$13h37m03.6s$
Decl. (center)	$-29d59'47.6''$
Distance (Mpc)	4.8
$R_{observed}$	7.85' = 11kpc
Synthetized Beam	0.75"x0.56" = 40x30pc

Messier, in Paris, it was a difficult object that he even said: "One is only able with the greatest concentration to see it at all." It was in early 19th century that the William Lassel described it as a "three-branched spiral". M83 was classified by G. de Vaucouleurs as SAB(s)c, from his catalog. M83 was also important for the discovery of extended ultra-violet disk, since it was one of the first study by G05.

Crosthwaite et al. (2002) studied the overall molecular gas morphology of M83 with CO(1-0) and CO(2-1) covering the 14'x14' optical disk.In this study they found that CO falls rapidly at radius of 5'=7kpc, and they proposed that this is also the decline in the total gas surface density, even if the HI emission continues further out, but with a lower surface density. Molecular gas dominates inside 7kpc radius (80% of the gas), while in total it is only 30% of the gas. The CO(2-1)/CO(1-0) intensity ratio is ∼1. At 7kpc, where the disk begins to warp, the ISM pressure might reach a threshold for the formation of molecular clouds.

Thilker et al. (2005) with GALEX observations have modified this view: diffuse UV emission is detected beyond the bright star-forming disk, when Hα and CO emission drop. This discovery made M83 the prototype of XUV disk galaxies. Koda et al. (2012) report deep Subaru Hα observations of the extended ultraviolet disk of M83, and found some weak emission, not seen by Thilker et al. (2005). Dong et al. (2008) with $SPITZER$ show that the SF has been an ongoing process in the extreme outer parts of M83 for at least 1Gyr. In a comparison between HI and FUV emission, Bigiel et al. (2010) show that the most extended atomic gas observed in M83 will not be consumed by *insitu* SF, and this might be due to the low efficiency of the HI-to-H_2 phase transition there. However the present low SF might be sufficient for chemical enrichment. A flat oxygen abundance gradient was obtained beyond R_{25} by Bresolin et al. (2009): they find only a slight decline in abundance beyond this galoctocentric distance with 12+log(O/H)=8.2 and 8.6. Bresolin et al. (2016) present a chemical evolution model to reproduce the radial abundance gradient of M83 in R_{25}, and their model is able to quantify the metallicity of the gas, which is very close to that of the stars. This is almost one of the other reasons to study the molecular gas in one region outside the optical disk of M83. In this section we present ALMA CO(2-1) data covering one region outside the optical disk of M83.

Observations

We observe CO(2-1) emission at 229.67 GHz (band 6) in M83 with ALMA during Cycle 2 (PI: Monica Rubio). The selected region is located at $13h37m03.6s$ $-29d59'47.6''$ enclosed

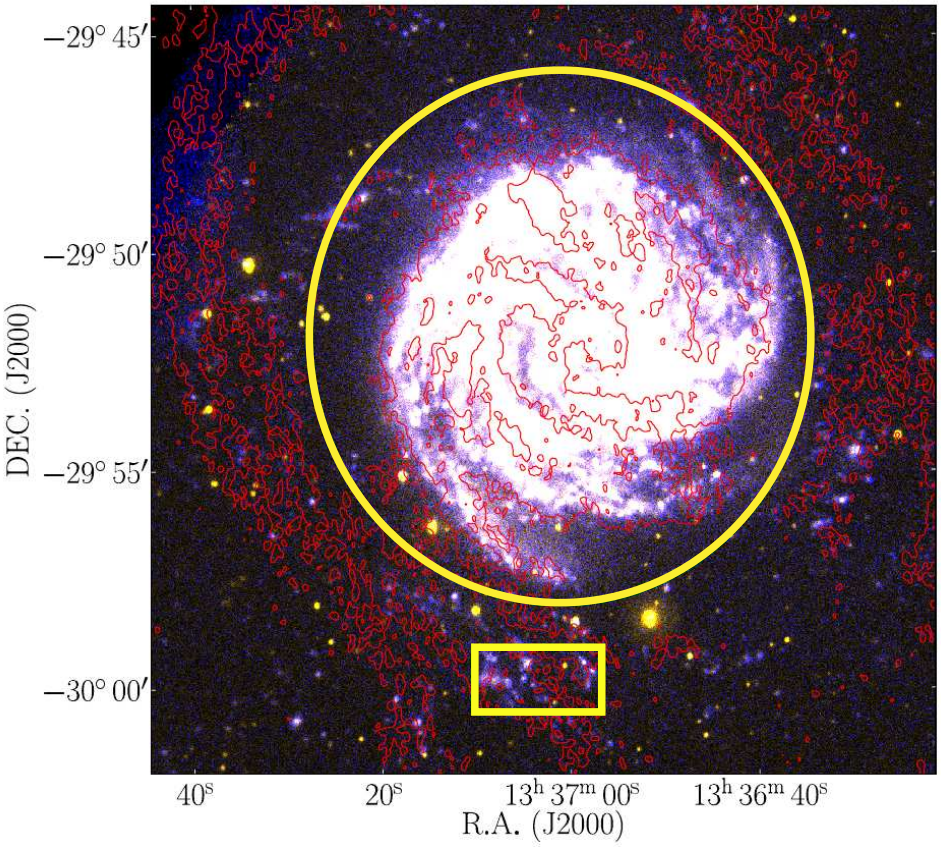

Figure 2.6 – *GALEX FUV image (background) of M83 with HI contours (red). The HI emission is from the THINGS survey. The yellow ellipse shows the optical radius ($r_{25} = 6.09' = 8.64kpc$) and the rectangle marks the region observed with ALMA and analyzed in this paper, located at $r_{gal} = 7.85' = 11kpc$.*

in a $3' \times 1.5'$ ($4kpc \times 2kpc$) rectangle located at $r_{gal} = 7.85' = 11kpc$ from M83 center. We used the selection criteria corresponding to FUV/NUV GALEX images (Gil de Paz et al., 2007a), using the peaks of UV emission, as well as the correlation with the HI emission from the THINGS survey (Walter et al., 2008). By choosing these peaks of emission we focused on the outer parts of the UV disks, beyond the r_{25} optical radius, where we are interested in detecting the molecular gas (see figure 2.6).

These selection criteria were used for the M63 XUV disk (NGC 5055), and led to a CO detection (Dessauges-Zavadsky et al., 2014) far outside the r_{25} limit, while Schruba et al. (2011b) only obtained an upper limit at 300" from the galactic center. The selected region of M83 was observed during 1hour in March 2014, in very good weather conditions (pwv 1.3mm). The 12m array was used with 34 antennas and a maximum baseline of 558.2 m. The map was done with a mosaic of 121 pointings separated by 12.9" (figure 2.7), and with an integration time of 10.8 sec per pointing.

The data were calibrated using the CASA reduction package. Approximately 36% of the data was flagged which was current at this epoch for 12m Array data. We produced

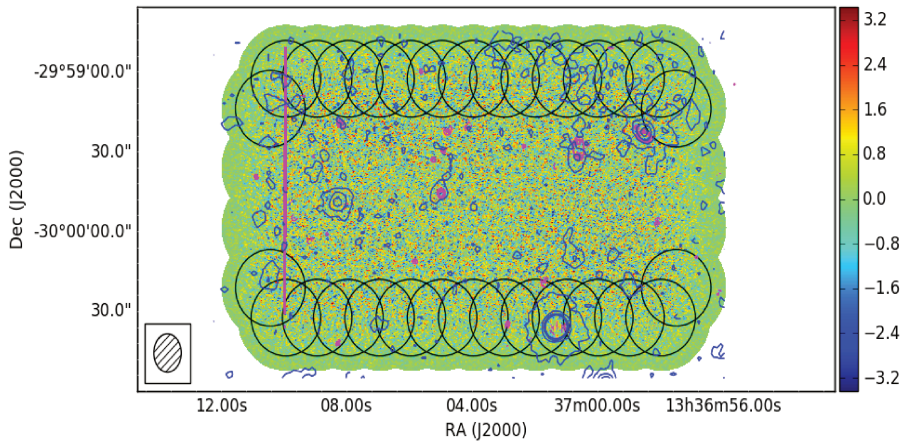

Figure 2.7 – *Scheme of the ALMA mosaic of our observations. The black circles of 27" diameter refer to the position of the 121 pointings used to map the CO(2-1) emission. The background image is the CO integrated emission (zero moment of the data cube). The contours are Hα (magenta colour) and FIR 24μm (black).*

a CO(2-1) data cube for each pointing with natural weighting, and for a velocity range from 15 to 1015 km/s, a channel spacing of 2.5 km/s and an rms of 10.3 mJy per channel. The calibrated 121 uv-tables were subsequently exported to GILDAS where the cleaning and the cube analysis were performed.

CO emission detection and upper limits

At the first sight, we searched in an automatic way for CO (2-1) emission with an SNR of more than 5 σ in each of the 121 cubes, with the "detection assessment" procedure in GILDAS, see example in figure 2.8.

From this assessment, we found 14 possibles emissions, falling in the HI range of velocities (500-700km/s) in this region of the galaxy, out of the 121 cubes. However, there is no spatial coincidence between these hints of emission and any of the other tracers. Also the width of the profiles are in general too large.

Reversely, we look for the most prominent clumps from other tracers, in particular Hα. Using the observations from the Subaru telescope (Koda et al., 2012) we found 13 regions of star formation, and tried to search for CO emission there. These regions are shown in the figure 2.9, where the circles scheme the spatial regions correspondent to our choice. After looking to the ALMA data, none of the hints found have more than 3σ signal.

In our observations, there is no continuum detection, except one weak (<2mJy) continuum (point) source, most probably a background source, at RA= 13h 37m 00.79s, DEC= -30° 00' 10.8". Using natural weighting, the synthesized beamsize of the continuum map was 0.78"x0.60", with rms=0.19 mJy.

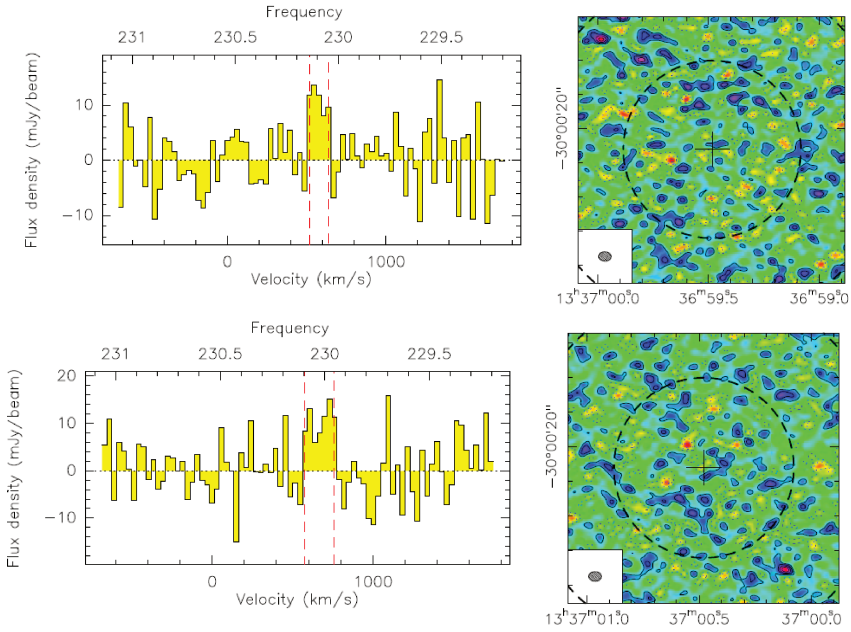

Figure 2.8 – *Example of search for CO detections using the task "detection assessment" at GILDAS. Both attempts of CO emission have more than 5sigma of SNR.*

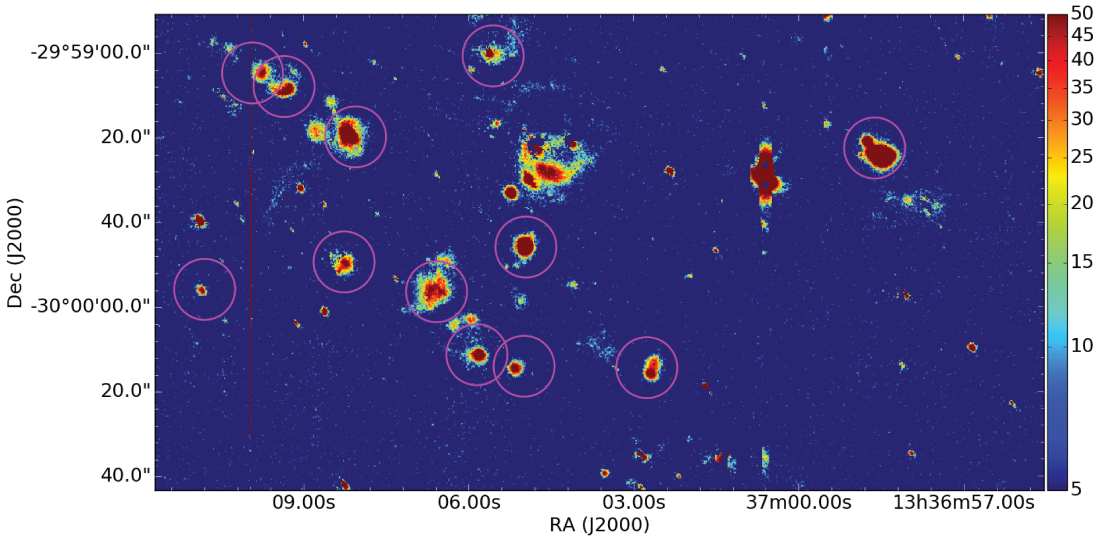

Figure 2.9 – *The H_α image of the region is shown, from Subaru (Koda et al., 2012). The magenta circles show the positions where CO was searched for.*

Using these two types of possibilities to find CO emission, we calculate the upper limits of our most prominent clumps. In this calculation we used GILDAS/CLASS , like is shown in figure 2.10 . Just from some spectra we really could have a weak gaussian, which leads us less possibilities than before.

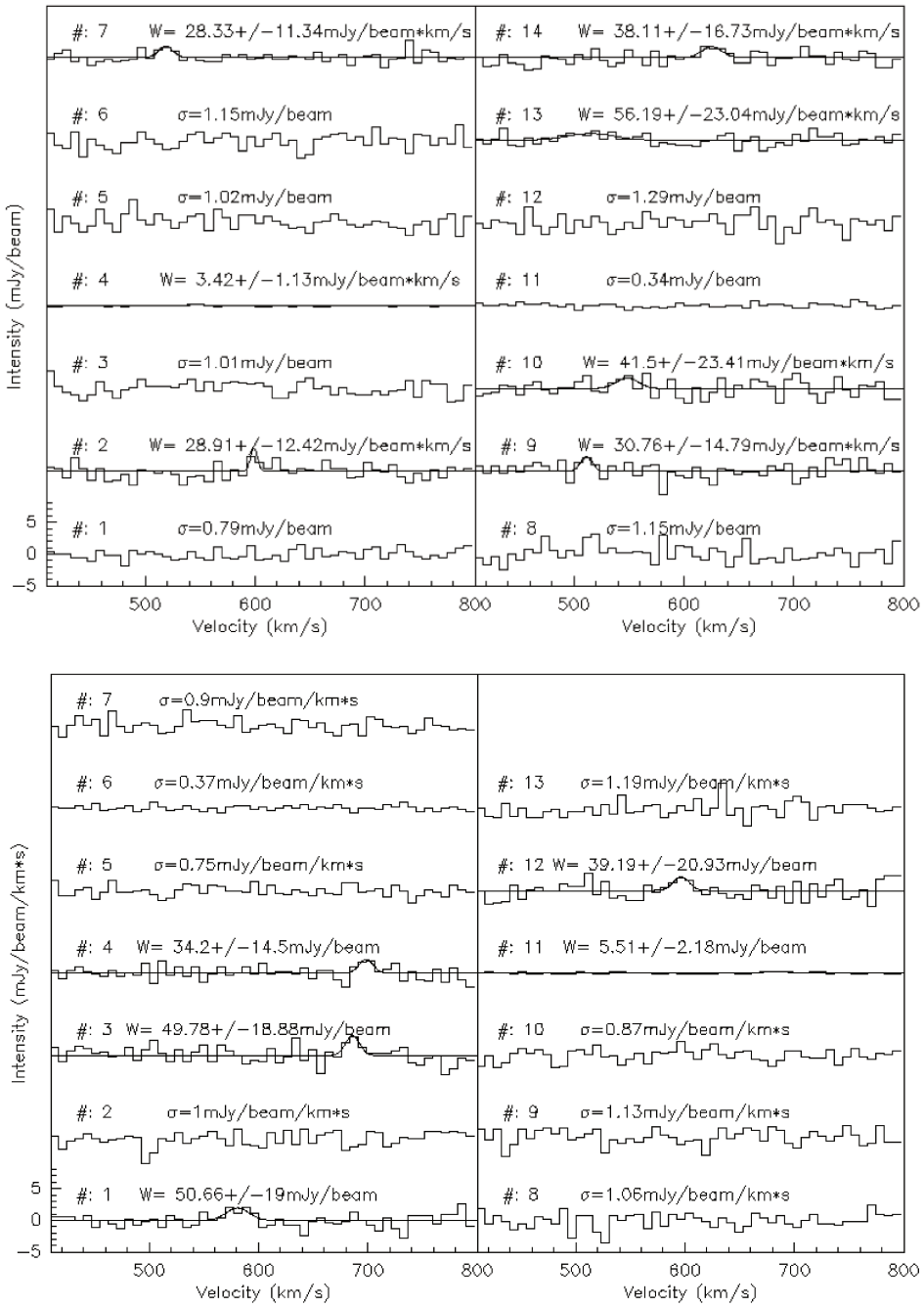

Figure 2.10 – *Spectra of the most prominent clumps, using Gaussian fits and rms estimation to calculate the upper limits. The values found indicated above at each spectrum are what we considered the values for upper limits.*

Matched Filter Technique

The reliable detection of weak signals is an issue in astronomical data. The data analysis process can lead us to underestimate the probability of false detection, that is why it is necessary to estimate it. A technique that is expected to have among the best probability of true detection is the Matched Filter (MF) technique. The goal of the filter is to

maximise the detectability of signal of known structure inside a random noise Gaussian (Vio & Andreani, 2016). To better comprehend the quality of our observations (e.g. to find out whether our measurements are biased) we first apply a simple technique. Here we want to check the assumption that the probability density function (PDF) of the noise peaks is close to a Gaussian. In Vio & Andreani (2016), they show from a zero-mean map that when the positions and number of sources are unknown the matched filter could underestimate the probability of false detections. We use here the simplest technique, where we plotted the pixels values from our moment 0 data. The values are plotted in figure 2.11. The plot shows no obvious irregularity or departure from a Gaussian, revealing no problem with the cleaning or reduction.

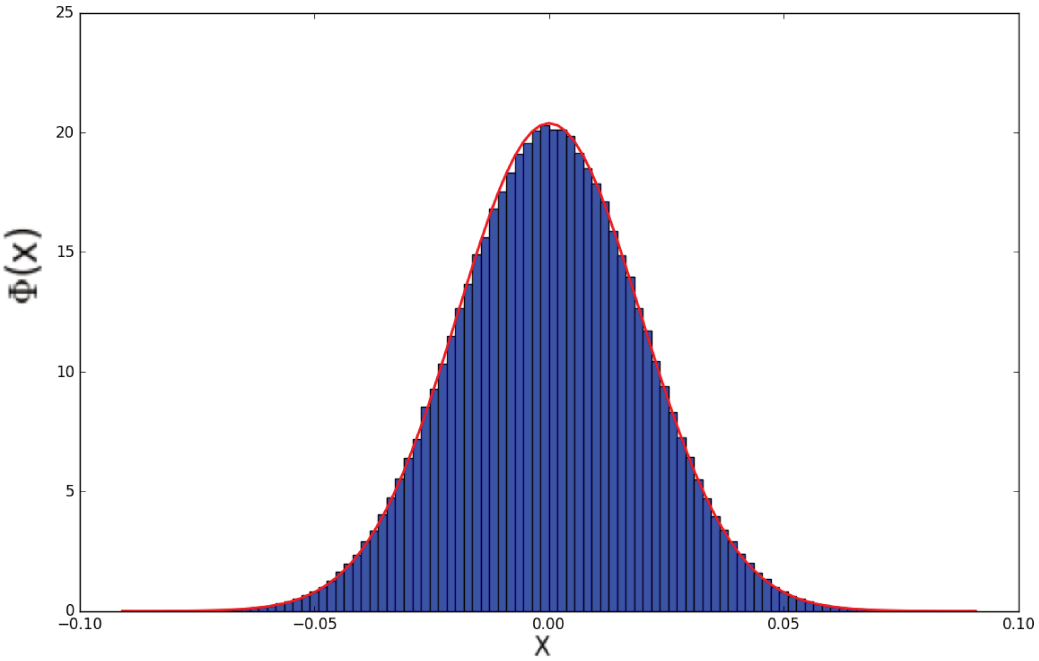

Figure 2.11 – *Histogram of the pixels values from the ALMA data cube (our observations). The blue histogram comes from the pixel values and the red curve is a Gaussian fit. We see that the noise is a perfect gaussian which does not show any indication of some bump that could be related to the reduction and deconvolution procedures.*

Stacking of CO spectra, according to the HI velocity

The CO emission is normally associated with HI peaks, because the host molecular clouds probably form in regions of relatively high HI column density, in absence of spiral density waves (Gardan et al., 2007) . Therefore, to exploit the full mosaic of data from ALMA, we must stack all individual spectra where emission is expected, at the HI expected velocity. Averaging all pixels of the map has not given any signal; this might be due to velocity dilution, since there is a significant velocity gradient, of $\sim$ 100km/s over the corresponding HI map (cf Figure 2.13). We therefore computed the first moment of the

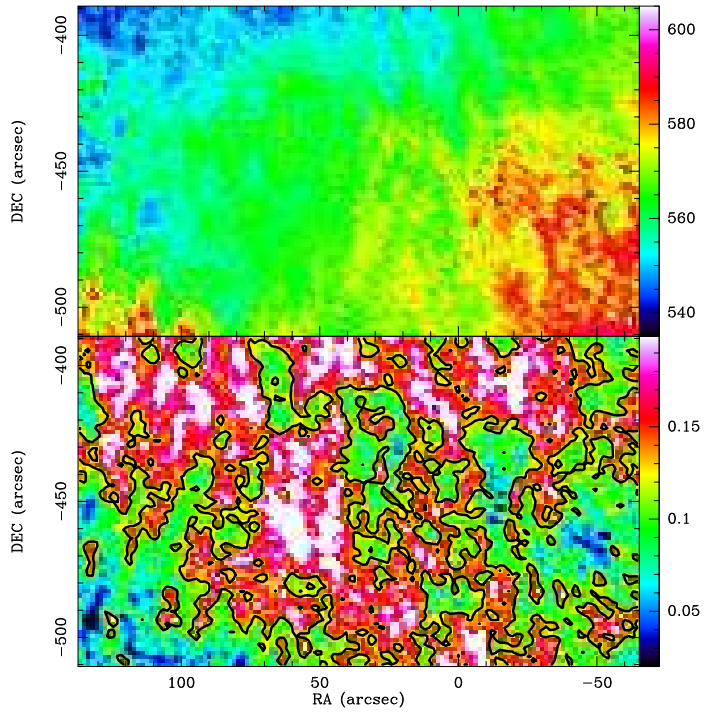

Figure 2.12 – *HI (THINGS) integrated intensity map (Jy×km/s, bottom) in the region of the mosaic observed by ALMA, and the corresponding average velocity (top) in km/s. The spatial coordinates are in arcsec offset from the galaxy center (13h37m00.9s, -29° 51'56"). The HI beam is 15.2" x 11.4" (VLA NA map from THINGS). The black contour corresponds to NHI = 10^{21} cm^{-2}.*

HI cube, to have an average velocity at each 1.5*arcsec* x 1.5*arcsec* pixel of the map. We smoothed the CO(2-1) map at the 1.5*arcsec* resolution, and for each beam, we shifted the spectra of the right velocity amount to have all of them centered at the expected velocity, known from the HI spectrum. Then we averaged all spectra, where the HI integrated intensity was above a certain threshold, which was 50 mJy/beam × km/s. The same stacking was done on the HI cube, which gives the result plotted in Figure 2.12. The resulting HI stacked spectrum has a FWHM of 33 km/s. No baseline was subtracted to the stacked spectra. The stacked CO(2-1) spectrum shows a hint of emission (at 3.5σ) with a FWHM of 14 km/s. When properly reduced, the average integrated flux is 0.17 mJy km/s. Adopting the conversion factor described above, this low value corresponds to an average mass of 13 $M_\odot$ of molecular gas per beam, but spread over 3 x10^4 beams, therefore would represent a total mass of 4 x 10^5 $M_\odot$ over the whole mapped region, of 4 x 2 kpc. The same computation can be done on the averaged stacked HI spectrum. With a flux of 0.1 Jy/beam km/s, and a beam of 15.2*arcsec* x 11.4*arcsec*, this gives a total HI mass of 4.2 x 10^7 $M_\odot$ over the same region. The mass ratio between the molecular and atomic gas is then $M(H_2)$ /M(HI) = 10^{-2} or below.

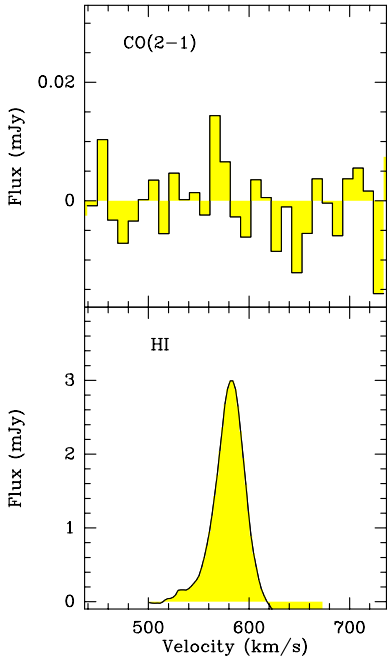

Figure 2.13 – *Result of the stacking procedure for the CO(2-1) map (top) and the HI map (bottom). Only spectra with a significant HI detection have been considered (see text), and they have all been shifted to 580km/s central velocity.*

Star formation diagram

The extended ultraviolet disks, present in 30% of nearby galaxies (Thilker et al., 2007), offer the opportunity to study the interstellar medium and star formation in extreme conditions with low average gas density and surprisingly abundant star formation. M83 was one of the first XUV detection in its outskirt regions and it is the prototype for these type of galaxies. However, no highly significant CO emission was detected in Cycle 2 ALMA maps. To analyse the impact of our observations in the context of star formation in outer XUV disks, we investigate the behaviour in the Kennicutt-Schmidt diagram of the tentative CO detections, in plotting the equivalent gas surface density, and star formation surface density.

The SFR surface density is determined using the calibration from Leroy et al. (2008):

$$\Sigma_{SFR} M_{\odot} yr^{-1} kpc^{-2} = 8.1 \times 10^{-2} F_{FUV}(MJysr^{-1}) + 3.2 \times 10^{-3} F_{24\mu m}(MJysr^{-1}) \quad (2.1)$$

We used the following equation to calculate the molecular hydrogen surface density:

$$\Sigma_{H_2} M_{\odot} pc^{-2} = 4.2 I_{1-0}, \quad (2.2)$$

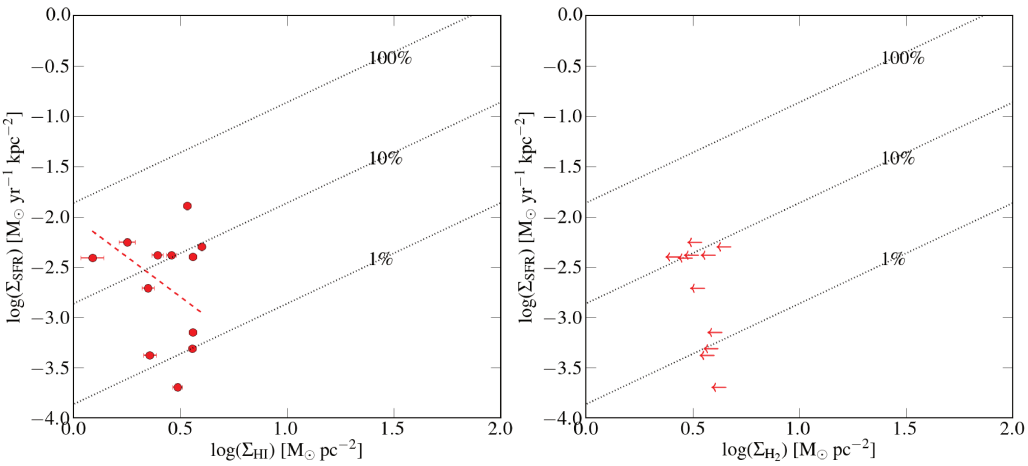

Figure 2.14 – *Kennicutt-Schmidt relations linking the SFR surface density to the gas surface density plotted separately fir Σ_{H_2} and Σ_{HI}. The black dotted lines represent "isochrones"of constant SFE, indicating the level of Σ_{SFR} needed to consume 100%,10% and 1% of the total amount of gas within 10^8 years.*

where I_{1-0} is the CO(1-0) line intensity in $Kkms^{-1}$, and we assume that the CO(2-1) to CO(1-0) intensity ratio is $R_{21} = I_{21}/I_{10} = 0.7$. With the spatial resolution of our observations, the flux scale is 0.018 Jy per K. The standard CO-to-H_2 conversion ratio of $X_{CO} = 2\ 10^{20}$ cm^{-2} /(K km s^{-1}) is adopted, and the number in equation 2.2 includes helium correction.

We plot the Kennicutt-Schmidt relation of M83 in figure 2.14 with HI data from *THINGS* (left plot) with our H_2 data (right plot). The regions used for this plot are the most prominent star forming regions in our observations.

Discussion and Perspectives

M83 star formation efficiency

In the previous section about M83 ALMA data, we display the CO upper limits in the star forming regions in the KS diagram, cf figure 2.14. In this figure, the star formation efficiency appears higher (with respect to H_2 gas) than in normal galaxy disks. We could have expected to find in some pixels masses corresponding to GMC. Since we know that the signal should correlate to the other ISM tracer, the HI-21cm emission, which gives us the spectral region to find the line, we now apply this filter to the data, through a stacking technique seen before in the section 2.3.4. We estimate the upper limit of CO column density in each pixel, given that there is no individual detection. Given the hint of global detection in the stacking of the CO compare with HI in M83, we assume a profile width of 15 km/s FWHM. The rms noise level is 4mJy in 15km/s channels, for

each beam of 0.75"x0.56". The corresponding 3σ upper limit in molecular mass per beam is $M(H_2) = 1.5/times10^4 M_\odot$, assuming an intensity ratio of I_{21}/I_{10}= 0.7 and a standard CO-to-H_2 conversion factor X_{CO} = 2 10^{20} cm^{-2} /(K km s^{-1}). This mass scale is much lower than a Giant Molecular Cloud (GMC) in the beam of 17 x 13pc.

Diagnostic comparison

It is interesting to compare M83 to other XUV disk galaxies already observed in molecular gas. Some of them have detected emission (Braine & Herpin, 2004; Braine et al., 2007; Dessauges-Zavadsky et al., 2014). Studying the KS law in the XUV disc galaxies, Watson et al. (2016) conclude that most extended UV-disc galaxies lack CO emission: CO detections are significantly offset towards higher SFR surface density for their molecular-hydrogen surface density.

To better understand the difference between the various studies, we plot the Kennicutt-Schmidt relation in figure 2.15, where we compare all data obtained in outer disks up to now, with the large sample of nearby galaxies from Bigiel et al. (2008). For M83, the regions used for this plot are the most prominent star forming regions in the Hα map. We have smoothed the molecular gas surface density over the extent of the Hα region size, about 200 pc, which leads to lower upper limits. In those regions, the average SFR surface density is high enough that we could expect to find only molecular gas. We then plot only the upper limit on H_2 surface density obtained by averaging over an assembling of 200 pc-sized region (then, this could increase the signal). For all other compared galaxies, only the molecular component is taken into account. It can be seen that the time to consume the molecular gas in the outer regions of M83 is smaller (t_{dep} < 3 10^8 yr) than the depletion time in nearby galaxies (t_{dep} = 3 10^9 yr). It is not relevant to represent in this diagram the average value obtained through the stacking over the whole region of 4kpc x 2kpc, since the surface densities are then diluted to a region much larger than the usual star forming regions, used in this diagram (about 200-500 pc in size). It is indeed over such scales that a star forming region can be defined. At lower scales, the star formation tracers, such as Hα or FUV, are not expected to be correlated to the molecular clouds of their birth, since newly born stars progressively drift away at a different velocity than the dissipative gas. For the other galaxies, the gas and SFR surface densities concern also such scales, like M63 (Dessauges-Zavadsky et al., 2014) corresponding to the IRAM-30m telescope beam of 0.5 and 1kpc in CO(2-1) and CO(1-0) respectively.

The dearth of CO emission in the outer disc of M83

One main issue to explain the absence of CO emission in galaxies is the metallicity Z of the gas. It is now well established that CO emission is frequently very faint or nonexistent in low-metallicity galaxies, for example in gas-rich irregular galaxies Elmegreen et al. (1980); Tacconi & Young (1987); Taylor et al. (1998). Both observations and theory indicate that the CO-to-H_2 conversion factor, X_{CO}, increases at low metallicity below

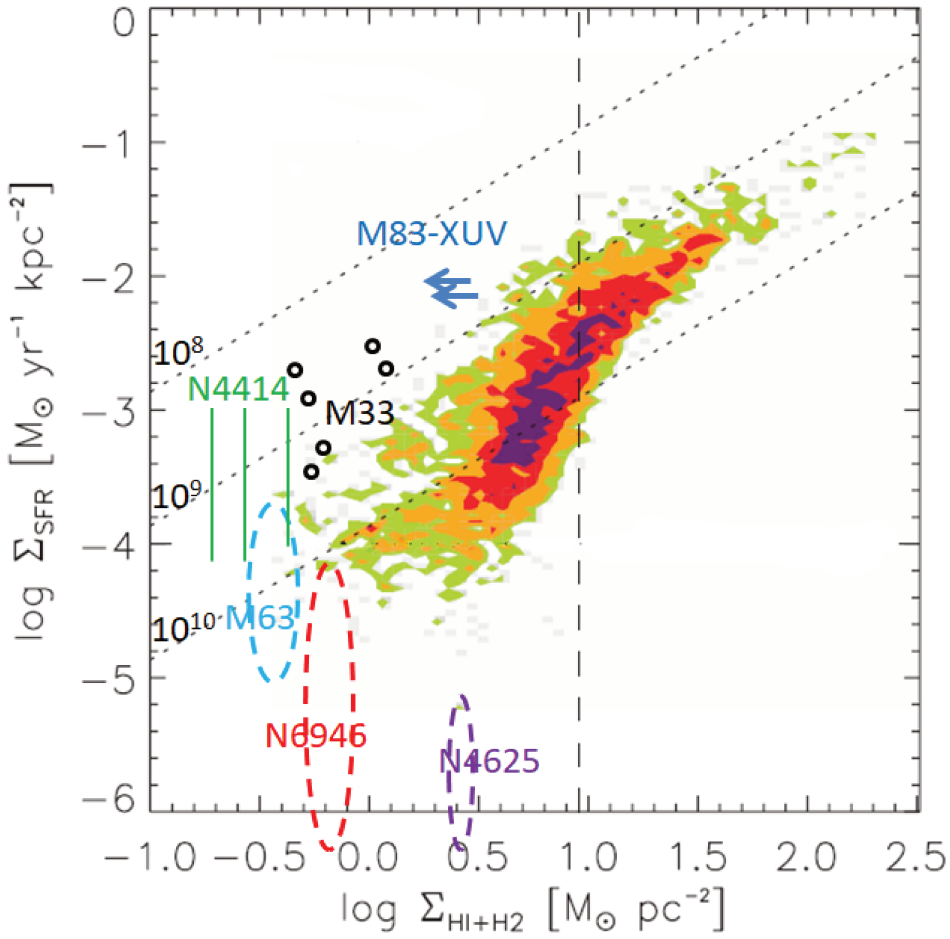

Figure 2.15 – *Kennicutt-Schmidt diagram relating the SFR surface density to the gas surface density, adapted from Verdugo et al. (2015) and Bigiel et al. (2008). Dashed ovals represent the data from the outer parts of XUV disk galaxies: NGC4625 and NGC6946 from Watson et al. (2016), and M63 (NGC5055) from Dessauges-Zavadsky et al. (2014), taking only the molecular gas into account in all of them. The 3 green vertical bars are from NGC4414 (Braine & Herpin, 2004), and the black circles for M33 (Gratier et al., 2010). The dotted vertical line shows the 9 $M_\odot/pc^2$ surface density limit above which the molecular gas dominates. Dashed inclined lines correspond to depletion times of 10^8, 10^9 and 10^{10} years to consume all the gas at the present SFR. The horizontal upper limits correspond to our CO(2-1) results on the M83 XUV disk, in two of the main SFR regions, of sizes ∼ 200pc.*

$12 + log(O/H) = 8.2 - 8.4$ Bolatto et al. (2013). The dependence of this relation is non-linear with Z, and may be in Z^{-2} or steeper at low Z, because of UV photo-dissociation in the absence of dust, in addition to the under-abundance of CO.

However, in the M83 field that we observed with ALMA, there is only little abundance deficiency, the average metallicity of the HII regions is $12+log(O/H) = 8.4$ Bresolin et al. (2009), i.e. 1/2 solar. With a slight change of X_{CO} for a higher value than standard, we should still be able to detect molecular clouds at more than 8σ. This means that the scatter in the X_{CO}-metallicity relation could not explain the dearth of CO emission.

The formation of the CO molecule occurs from OH via ion-neutral reactions that form HCO+, which after its dissociation forms CO. Thus, the CO formation rate depends on the abundance of OH, itself related to the rate of destruction by UV photons. The destruction of the CO molecule is mainly by photodissociation. In diffuse environments, the molecular clouds are more isolated, and less shielded. A schematic view of a molecular cloud includes a dense core, with CO emission, and a surface where CO is photodissociated, and emitting essentially in C+ and C lines (see figure 1.9). Because H_2 and CO have similar dissociation processes in their line-transitions, H_2 can partially shield the CO molecule, but with large CO column densities, the CO molecule is self-shielding. At low CO column densities, and in particular in the outer parts of molecular clouds, the CO molecule is absent, and the CO/H_2 abundance ratio drops. All the carbon is found in C and C+, and this gas is called CO-dark molecular gas.

Another possible scenario which could explain the lack of CO emission is that the photo-dissociated region is fragmented in smaller clouds. Each one has not enough depth to have CO emission, and is dominated by C+ emission. In outer disks, the small star forming clouds will emit much less together, for the same amount of gas, than the larger clouds present within the optical disk. The same scenario was invoked in Lamarche et al. (2017) where they failed to detect CO emission towards the starbursting radio source 3C368 at z=1.13 using ALMA data. They discuss the possibility that they observe far-infrared fine-structure oxygen lines in star-forming gas clouds before they have had the chance to form an appreciable amount of CO.

Watson et al. (2016) did not have a precise reason for not detecting CO in a young star-forming region of NGC4625, while Braine et al. (2007), Braine & Herpin (2004) and Dessauges-Zavadsky et al. (2014) could detect weak CO emission in the outer parts of NGC 6946, NGC 4414 and M63, respectively. However, in M63 CO is detected only in two out of 12 XUV-disc regions. Watson et al. (2016) conclude that, even if one explanation for the dearth of CO emission in lower-mass galaxies can still be the low metallicity, the issue remains for the outskirts of massive galaxies. Deeper observations are needed to disentangle the various proposed scenarios.

The gas metallicity is only half solar in our mapped ALMA field, which could already reduce the size of the CO clouds with respect to H_2 clouds. The dearth of CO emission could come also from the excessive local FUV radiation field, which dissociates CO preferentially, and from the small size of the clouds in the outer regions of some galaxies. M83 shows particularly strong FUV emission in its outer regions, with respect to others galaxies: the FUV flux ranges between 0.2 and 1.2 $\times$ 10^{-2} MJy/sr over our region. The resolution of the FUV observations is 100 pc, at the distance of M83, so we cannot know exactly the radiation felt by each cloud. Although the FUV flux is much smaller than in the inner galaxy disk, clouds are smaller and less numerous in outer parts of galaxies (here at half metallicity), which explains the more extended CO dissociation. This could be explored further through follow-up observations of the dust continuum in the Rayleigh-Jeans domain in the same region, another independent tracer of the molecular gas.

Perpectives

To test the hypothesis that the molecular clouds in some XUV disks are dominated by CO-dark molecular gas, we have proposed an observation with ALMA in band 7 to observe the dust continuum emission of the same field observed in cycle 2 in CO(2-1) (see figure 2.16). The PI of this project is Linda Watson and the other collaboraters are: Jin Koda; Monica Rubio; Celia Verdugo Kana Morokuma; Samuel Boissier; Frank Bigiel; David Thilker; Yutaka Komiyama and Thomas Puzia.

Dust continuum emission might be used as an other tracer of molecular gas, it scales with the total amount of gas independently of its phase (HI, H_2). This will give the possibility to have a flux density of 850μm for a 3$\times$ $10^4 M_\odot$ molecular cloud.

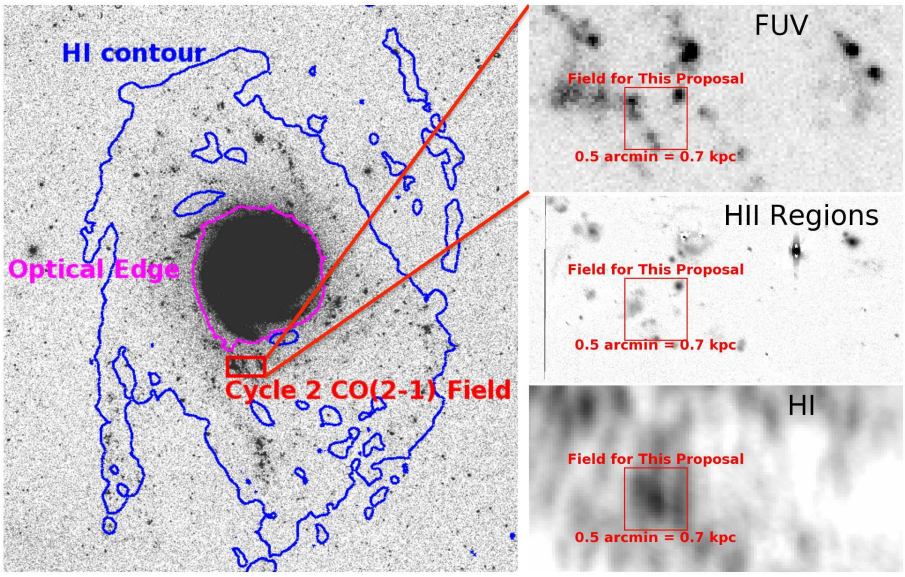

Figure 2.16 – *Figure from ALMA proposal. Zoom-in on the CO(2-1) field in FUV (top) Hα continuum-subtracted (middle: Koda) amd HI 21 cm (bottom Walter).*

Part Two

The star formation efficiency at high-redshift

CHAPTER 3

Star formation in galaxies at higher redshift

Determining the cosmic history of star formation through the Hubble time will help to understand how galaxies are formed. Galaxies evolve with time, at different rates according to their types. The Milky Way and similar nearby spirals form a few stars per year, contrary to main sequence galaxies 10Gyr ago, whose star formation rates (SFR) were twenty times higher. Understanding how SFR evolves through cosmic time, and how galaxies stop suddenly to form stars and are quenched, is one major goal of galaxy evolution. The processes controling star formation in the ISM are complex, and depend on galaxy internal dynamics and stability, galaxy interactions, and also feedback processes from supernovae and AGN.

Stars are formed from molecular gas, and high star formation rates require significant gas supply Madau & Dickinson (2014). In exceptional cases, this supply can be very high during a short period, and this leads to a starburst. But most of the stars in the Universe are produced in what is called the Main Sequence (MS) of star formation, where the time to consume the gas reservoir is at z=0 of the order of 2 Gyr (the depletion time). The main sequence is the location of these "normal" star-forming galaxies in the diagram of SFR versus stellar mass. On large samples of galaxies (for example the SDSS), color-magnitude diagrams have revealed a characteristic bimodality, i.e. the existence of a sequence of red passive galaxies and of a blue cloud of star-forming galaxies. The evolution of the specific star formation rate (sSFR, or SFR divided by the mass), of the gas fraction ($\mu = \mathrm{M}_{gas}/\mathrm{M}_{*}$) and of the star formation efficiency SFE = SFR/M_{gas} (the inverse of the depletion time) with redshift, are all crucial parameters to better understand the evolution of the main sequence of galaxies. Measurements of these quantities at different redshifts provide a better characterisation of galaxy evolution, allowing us to test the cosmic building-up and the winding-down of star-forming main sequence galaxies.

Indeed, the main features of the cosmic star formation density evolution across the Hubble time is a first increase until z$\sim$ 2, and then a decrease or winding down from z=2 to 0 by a factor 20. This evolution of the cosmic star formation density was initially attributed to a period rich in major mergers of galaxies around z=1-2 (e.g., Larson & Tinsley, 1978; Mihos & Hernquist, 1996; Elbaz & Cesarsky, 2003). These major mergers

would have produced starbursts, characterized by very short depletion time (t_{dep} <0.1 Gyr). But observations have revaled instead that may be 90% of the stars formed in the Universe are formed in the main sequence galaxies. This sequence is defined in the SFR-M_* diagram by an almost linear curve, with an rms scatter of about 0.3 dex. This indicates that the evolution of the SFR is not driven by mergers and starbursts, but by a decline in the cold gas reservoir supply, and also a decline in the star formation efficiency. If the decline was caused by mergers the scatter would be much larger, and there will be a larger population of galaxies above the main sequence, in the starburst regime. Many parameters can affect the gas supply, e.g winds driven by SN or AGN feedbacks, internal dynamics, and cold gas accretion from cosmic filaments, depending on environment.

The IRAM Plateau de Bure interferometer, today called NOrthen Extended Milimeter Array (NOEMA) (Schuster et al., 2007), with the PHIBSS program (Tacconi, Combes et al.) aimed to better understand these processes within normal MS galaxies, and to determine their molecular gas reservoirs. PHIBSS (Plateau de Bure High-z Blue Sequence Survey) is a Large Program to observe the CO lines in main sequence galaxies, and analyse the star formation law at sub-galactic scales at z=1.2 and 1.5 Genzel et al. (2013); Freundlich et al. (2013). Statistics over a large sample, and detailed mapping in the best cases, could also help us to characterize the star formation process across the epochs.

Now, PHIBSS has been continued with the Large Program PHIBBS2, providing a second phase of results, allowing to follow the gas fraction, the star forming efficiency (or depletion time), the Kennicutt-Schmidt (KS) relation, resolved or not, as a function of the morphology of galaxies (namely the bulge-to-disk ratio, the spiral structure, the surface density and concentration), across a wider range of redshifts, and also a wider departure from the MS (i.e. either starburts or partially quenched galaxies). The new CO measurements made in the last years involve more than 110 galaxies. These observations provide some possibilities to test the gas-regulated equilibrium model by measuring mean molecular gas fraction and depletion times across MS and redshifts. Follow up mapping with ALMA has been also undertaken, for galaxies in the southern COSMOS field.

The star formation at high redshift

Since star formation is directly linked to the amount of molecular gas present, it is important to determine the gas fraction as a function of redshift. Does the SFE increase or decrease with redshift? Does the molecular content of galaxies evolve with redshift? What happens in the evolution of star formation rate density (SFRD) with cosmic time? Can we explain the star formation peak at z=2-1 in the history of the Universe?

These important questions are still not completely answered. More important though, is to try to understand the influence of galaxy masses and morphologies, and the influence of environment, which appear to be the main empirical factors in star formation quenching (Peng, Lilly et al 2010). To do so, it is primordial to study the star formation from the local Universe to high redshift, and to compare the various galaxy masses and types.

The cosmic star formation history

Over the past two decades, many works have been published reporting measurements of the cosmic stellar mass density (SMD) at many different redshift using different data sets. Certain works made use of surveys such as the HDF-N, the Hubble Ultra deep Field (HUDF), Great Observatories origins Deep Surveys (GOODS), and Cosmic Evolution Survey (COSMOS) . The most common tools for the analysis of the cosmic SFRD are the rest-frame ultraviolet continuum measurements, because this method is quite sensitive and can be applied over a very broad range of redshift. Lilly et al. (1996) were the first to combine a large and deep spectroscopic redshift survey with multi wavelength photometry and to derive luminosity function at several different rest-frame wavelengths, including the UV rest-frame. They found that the luminosity density decrease by one order of magnitude from z = 1 to the present, which they interpreted as a steep decline in the SFRD. Madau et al. (1996) used the then-new HDF observations to extend this analysis at higher redshift, where they quoted only lower limits for the SFRD. Subsequently, many others surveys extended this finding using different methods.

The cosmic star formation and its evolution across the Hubble time are well studied since then. Nowadays, this relationship is well known and established: the SFRD peaked 3.5 Gyr after the Big Bang, and dropped exponentially at $z < 1$ with a timescale of 3.9 Gyr, like shown by Madau & Dickinson (2014), see figure 3.1. The Universe was more active in the past than today: stars formed at a peak rate almost 20 times that seen at the present epoch.

One of the main ways to analyze the cosmic star formation history (CSFH) is to try to understand the evolution of the H_2 density. Predictions by models and simulations show that the molecular gas density increases with redshift, and it becomes at high z dominant over the atomic gas in galaxies, while the contrary is true at z=0 (Combes et al., 2013).

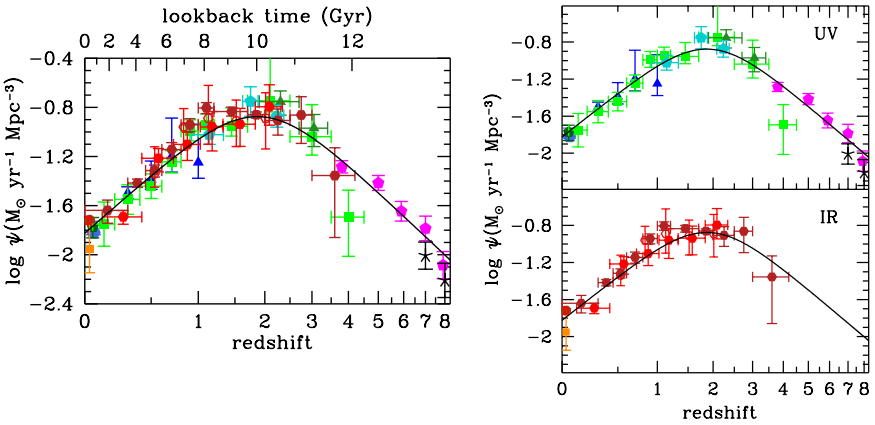

Figure 3.1 – *From Madau & Dickinson (2014): diagrams showing the history of cosmic star formation density from (top right panel) FUV, (bottom right panel) IR, and (left panel) FUV+IR rest-frame measurements.*

Main Sequence galaxies

The decrease after the peak (previously discussed) is not the same for all galaxy populations: stars are not forming at the same rate for all of them, and their quenching times and epochs vary. In other words, there is a bimodality between red passive galaxies and blue star-forming galaxies, as is well displayed in color-magnitude diagrams (e.g., Baldry et al., 2004; Bell et al., 2005; Noeske et al., 2007; Elbaz et al., 2007; Daddi et al., 2007; Damen et al., 2009; Santini et al., 2009; Wuyts et al., 2011a). The color is related to the SFR: galaxies are actively forming stars in the blue cloud, while galaxies in the red sequence are red and dead, i.e. their star formation has been quenched.

As shown in the figure 3.2, the bimodality holds at least from redshift $z = 0$ to $z \approx 2.5$, i.e., over the past 10 Gyr. The blue star-forming galaxies lie on a tight relationship between their stellar mass M_{star} and their SFR, the 'main sequence of star formation' (MS). The majority of the star formation history (~ 90 %) since $z \lesssim 2.5$ occurs in the MS (Rodighiero et al., 2011; Sargent et al., 2012).

The formation of stars is not the only characteristic of the bimodality, it happens that the colours define their morphologies: red for the ellipticals galaxies and blue for the disk ones. In terms of Sérsic index, MS galaxies have their indexes closes to 1, while the red ones have higher indexes, up to 4. Star Forming Galaxies (SFGs) on the MS are well characterized by exponential disks, quiescent galaxies at all epochs are better described by de Vaucouleurs profiles (n=4). Figure 3.2 shows the main sequence of star formation in terms of Sérsic index in the stellar mass, where the $n_{sersic} = 1$ corresponds to an exponential disk while $n_{sersic} = 4$ or de Vaucouleurs profiles describe elliptical galaxies and bulge-dominant galaxies. In other words, the profile shapes of galaxies are not a monotonic function of their star formation level. In Wuyts et al. (2011b) both their low and high redshift galaxies samples show an evolutionary connection between the high SFR

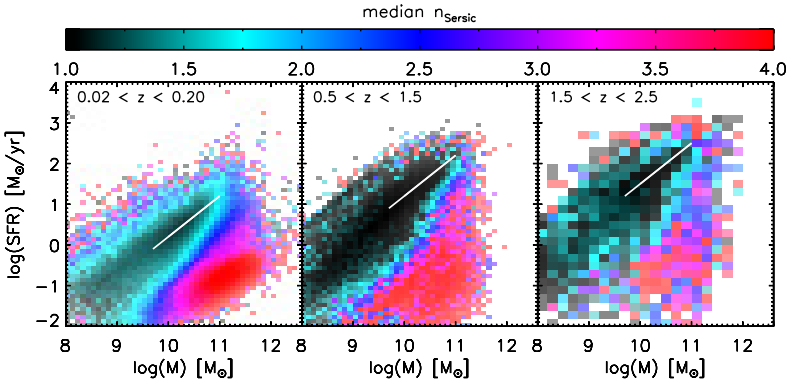

Figure 3.2 – *From Wuyts et al. (2011b): the definition of the main sequence. Three panels at different redshifts show SFR versus stellar mass. The color indicates the Sersic index of the stellar surface brightness profile. Blue corresponds to exponential disks, while red means quenched bulges or early-type galaxies. The SFR on the main sequence increases steadiy with redshift.*

and the quiescent galaxies, which is characterized by a cuspy surface brightness in their profiles. This introduces the merger problem: longer star formation cycles imply that the number of star-forming galaxies in a quiescent mode is higher, and then mergers are less frequent (Daddi et al., 2005; Caputi et al., 2006; Daddi et al., 2007). Also, the majority of galaxies in the local Universe do not present any classical bulges, implying that a large quantity of galaxies did not suffer any major merger since z=4 (Weinzirl et al., 2009).

SFE at high redshift

In a study of gas fraction and SFE in galaxies across redshift, Combes et al. (2013) concluded that there is a rise of SF efficiency between z=0.2 and z=1 (see figure 3.3). The star formation evolution depends on two factors, and the most important one is the gas fraction. They also concluded that both SFE and gas fraction play an important role in the SFH of Universe. Considering the evolution with cosmic time, the amount of gas decreases from z∼3. This can be related to the cosmic star formation history, since the gas fraction considerably increases with redshift.

In the same work, they show that some extreme objects with SFE $> 1000 L_{\odot}/M_{\odot}$ are perturbed due to galaxy interactions. Also, to better understand whether there is some correlation between SFE and the compactness, more high resolution mapping is needed. The new large facility ALMA is essential to do this kind of study. With high spatial resolution, it becomes possible not only to link the SFR to gas content globally, but also explore a resolved Kennicutt-Schmidt relation. indeed, the KS relation is almost linear, but as shown in Freundlich et al. (2013) and Cibinel et al. (2017) the SFE can vary in different regions within the same galaxy.

It becomes now more evident that the star formation suffers an abrupt decline between z=1 and z=0 due to the SFE drop (Combes et al., 2011). To trace redshift evolution, and

in particular the quenching of star formation after z=1, the intermediate redshift is then a key to study the major issues about star formation efficiency through cosmic time.

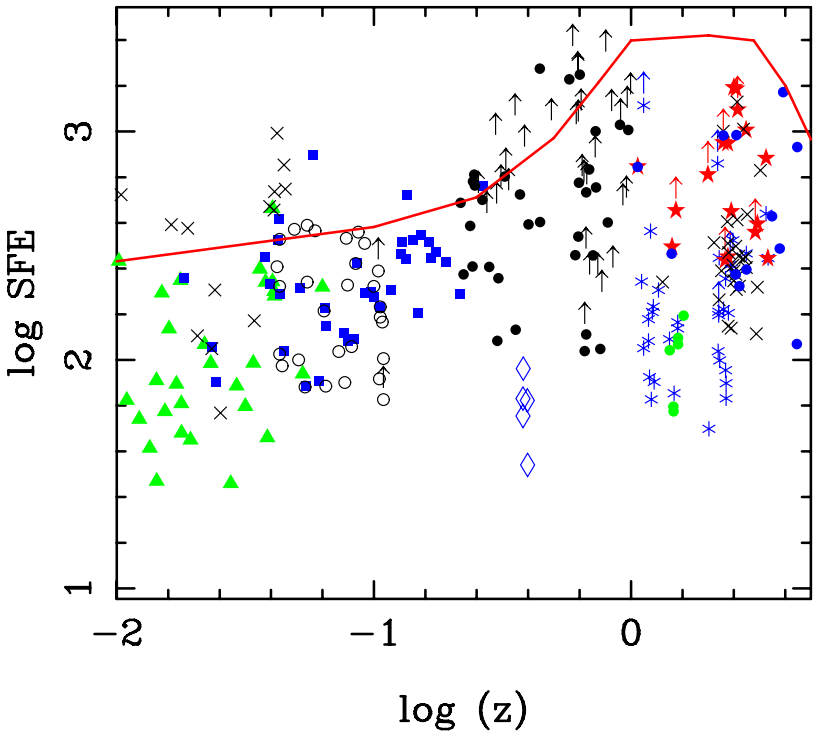

Figure 3.3 – *From Combes et al. (2013): Star Formation Efficiency SFE=$L_{FIR}/M(H_2)$ versus redshift. The red line represents schematically the evolution of cosmic star formation density. The points correspond to the various surveys available in the literature.*

The PHIBSS Program

The Plateau de Bure HIgh-z Blue Sequence Survey (PHIBSS, PI: L. Tacconi and F. Combes) is a Large Program on the IRAM Plateau de Bure Interferometer (PdBI; refs). The *Institut de radioastronomie millimétrique* (IRAM) is a French-German-Spanish collaboration that combines two radiotelescopes. One is a 30m-diameter single-dish located on Pico Veleta (called 30m-IRAM) in Spain, and the second is the interferometer called NOEMA, located at Plateau de Bure (where came the name for this project and the old name for the telescope) in the French Alps. At the time of the PHIBSS program, the PdBI (its name at that time) consisted in six antennas, each of them being 15m in diameter. Since then, two additional antennas have entered scientific operation. The next years, IRAM will continue to implement others antennas to the array until 2020, to build a 12-antenna telescope. The antennas are mounted on rails and can be distant up to 760m from each other to achieve a maximum spatial resolution of about 0.4″.

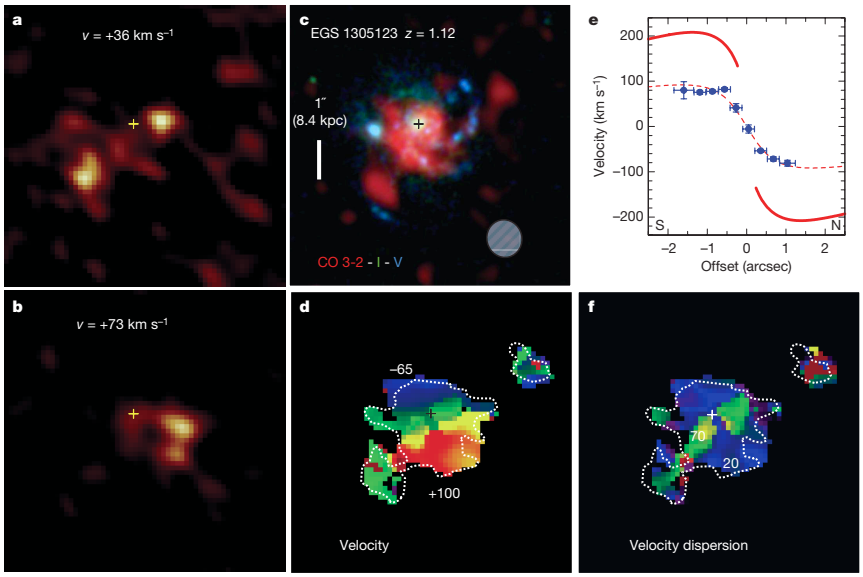

Figure 3.4 – *Molecular gas and kinematical maps for the EGS 1305123 galaxy at z=1.12, from Tacconi et al. (2010). The panels a) and b) are two CO(3-2) channel maps, at 36 and 73km/s. c) is the CO integrated line, composite with HST images. d) is the CO velocity map and e) the CO rotation curve . f) is the CO velocity dispersion. The velocity dispersion is derived by subtracting a rotating exponential disk best-fit model to the velocity field*

The first main goal of PHIBSS was to better understand the evolution of star formation and gas content within Main Sequence (MS) galaxies during the winding-down of cosmic star formation, after the z=2 peak. The study was made specifically from the point of view of molecular gas reservoirs. The PHIBSS program covers a large sample of galaxies until z$\sim$ 3.

The first part of the project comprised 52 CO (3-2) detections with 8 in higher resolution imaging with beam sizes between 0.3"-1". The main result of the project was to show the increase of gas fraction with redshift: galaxies at z=1.2 have mean molecular gas fractions $f_{gas} = M_{gas}/(M_{gas} + M_{star})$ of 33% and galaxies at z=2.2, 47%, while at z=0, the percentage is $\sim$ 5%. Gas-rich disks are more likely to be gravitationally unstable, and thus to display clumpy features and to form stars. PHIBSS observations have shown that the molecular gas corresponds to an extended disk comparable in size to the stellar disk of the HST images. Figure 3.5 shows the molecular gas content, velocity and velocity dispersion maps, as well as the rotation curve for the observations of one of the galaxies imaged at high resolution with PHIBSS (Tacconi et al., 2013). The rotation curve is very well fitted with an exponential disk model. However, the dispersion shows that the disk is relatively turbulent.

The PHIBSS obtained a near linear KS relation, e.g fig 3.5. This is consistent with low redshift measurements (Tacconi et al., 2013; Genzel et al., 2010). The depletion time of 0.7 Gyr founded for them is slightly lower than at present time. The timescale represents

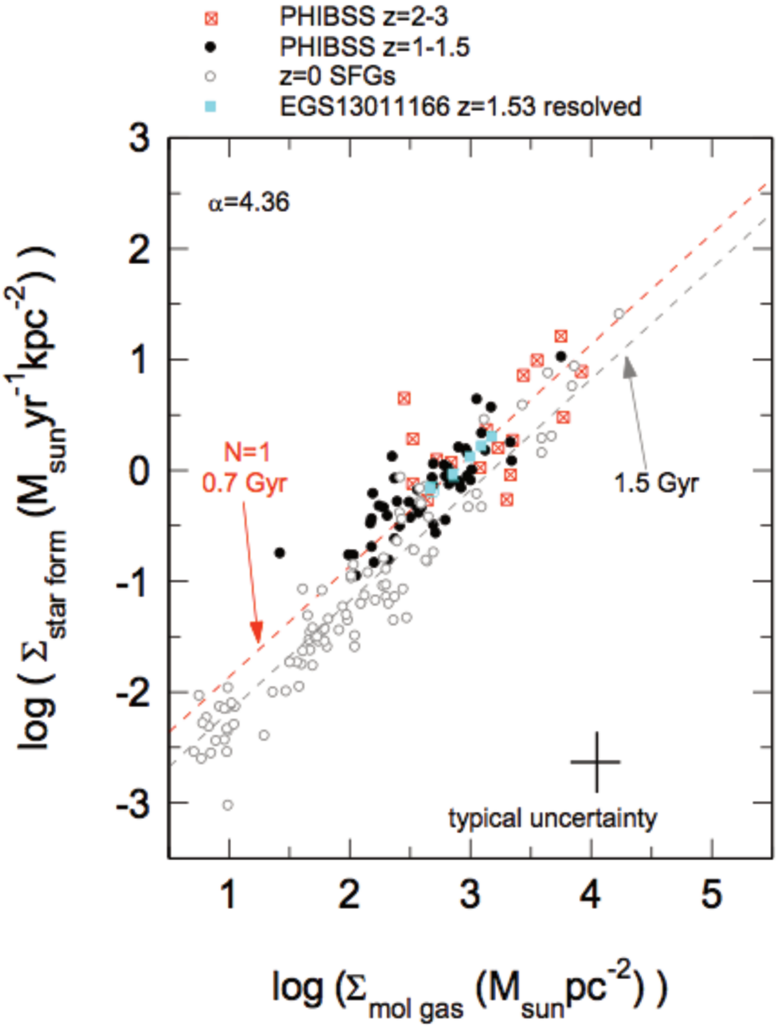

Figure 3.5 – *Kennicutt-Schmidt (KS) diagram, relating global SFR and gas surface densities of galaxies in the literature, compared with the PHIBSS samples, from Tacconi et al. (2013).*

the time needed for a galaxy to consume its gas in order to form stars, where this results implies a faster formation cycle implying a need for a gas to become full at the peak of the star formation activity.

In this project, a resolved KS relation was also obtained as can be seen in figure 3.6. The resolved kinematics enables to separate smoothed clumps by their different velocities, even below the spatial resolution, allowing the KS relation to be constructed at kpc-scale for four galaxies of the sample (Freundlich et al., 2013). An additional success of this project was a pixel by pixel KS relation for one typical massive star-forming galaxy with z=1.53. Genzel et al. (2013) took into account the extinction in H_{alpha} observations to show that the slope and shape of the relation depend on the extinction applied.

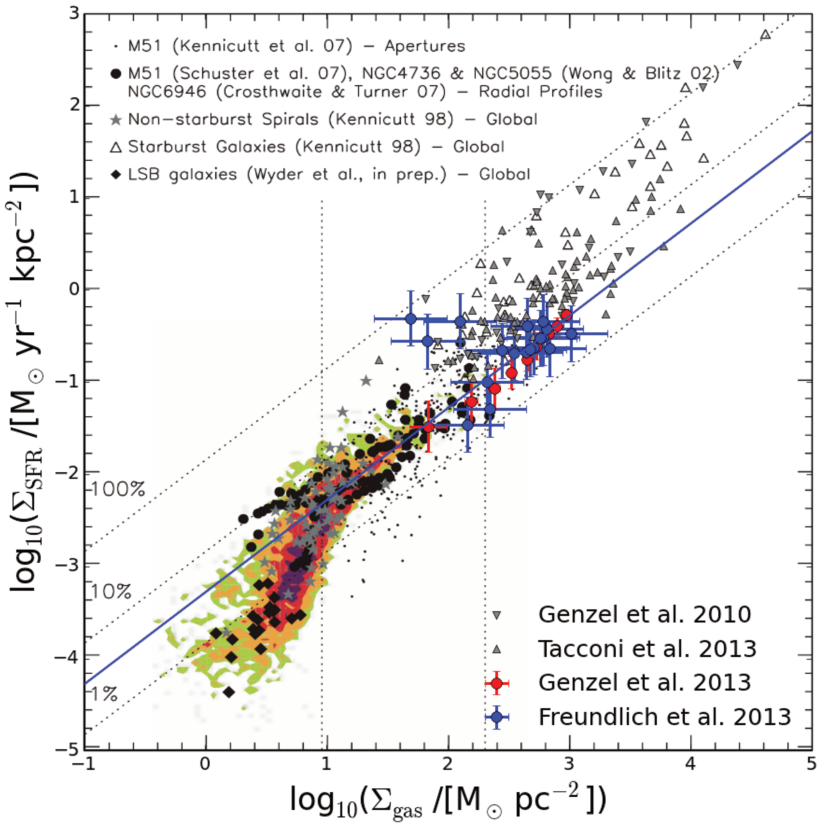

Figure 3.6 – *Spatially resolved molecular KS relation for ensembles of clumps of four galaxies from the PHIBSS sample (Freundlich et al., 2013) and for binned groups of pixels in EGS13011166 (Genzel et al. 2013), superimposed on the sub-galactic KS diagram obtained at low redshift by Bigiel et al. (2008). The solid blue line corresponds to a constant depletion time tdepl = 1.9 Gyr, and the grey data points to galaxy-averaged measurements. (Freundlich SF2A 2014)*

CHAPTER 4

PHIBSS2: Plateau de Bure HIgh-z Blue Sequence Survey 2

Due to observational difficulties, very little is known about the molecular gas content of galaxies for redshifts between z=1 and z=0. Paradoxically, it is easier to study higher redshift galaxies, because the CO line flux increases with the frequency at high-J lines of the rotational ladder (Combes, 1999). It is therefore necessary to carry on an observational program to determine the molecular gas in a wide range of redshifts. PHIBSS aims to study the molecular gas content in galaxies after the epoch of the maximum in cosmic star formation.

The PHIBSS2 Large Program

The second part of the program, now observing almost 150 galaxies, has more statistics, and explored more redshifts, and some departures from the MS . *PHIBSS 2 legacy program* was built from the success of the first results, intending to widen the range of redshifts to better understand and have a better sample in the MS plane at each redshift. The measurements enable to test, in a more rigorous way the gas regulation equilibrium model by the mean molecular gas fractions and depletion times in different redshifts across the MS.

In total the program used 1700 hours with NOEMA. The goal of the project was to exploit and optimize the NOEMA telescope performances. The new antennas had a significant statistical gain, with more dynamical range and more sensitivity.

Some authors have already observed that the depletion time decreases with redshift: normally the timescale to consume gas in galaxies at the present SFR is 2Gyr at z=0 and drops by a factor of 2 to 4 at z=2.5 (e.g., Bigiel et al., 2008; Daddi et al., 2010; Genzel et al., 2013; Tacconi et al., 2013, 2018; Saintonge et al., 2011). This has been confirmed recently with the results of PHIBSS2, the figure 4.1 from Tacconi et al. (2018) shows a

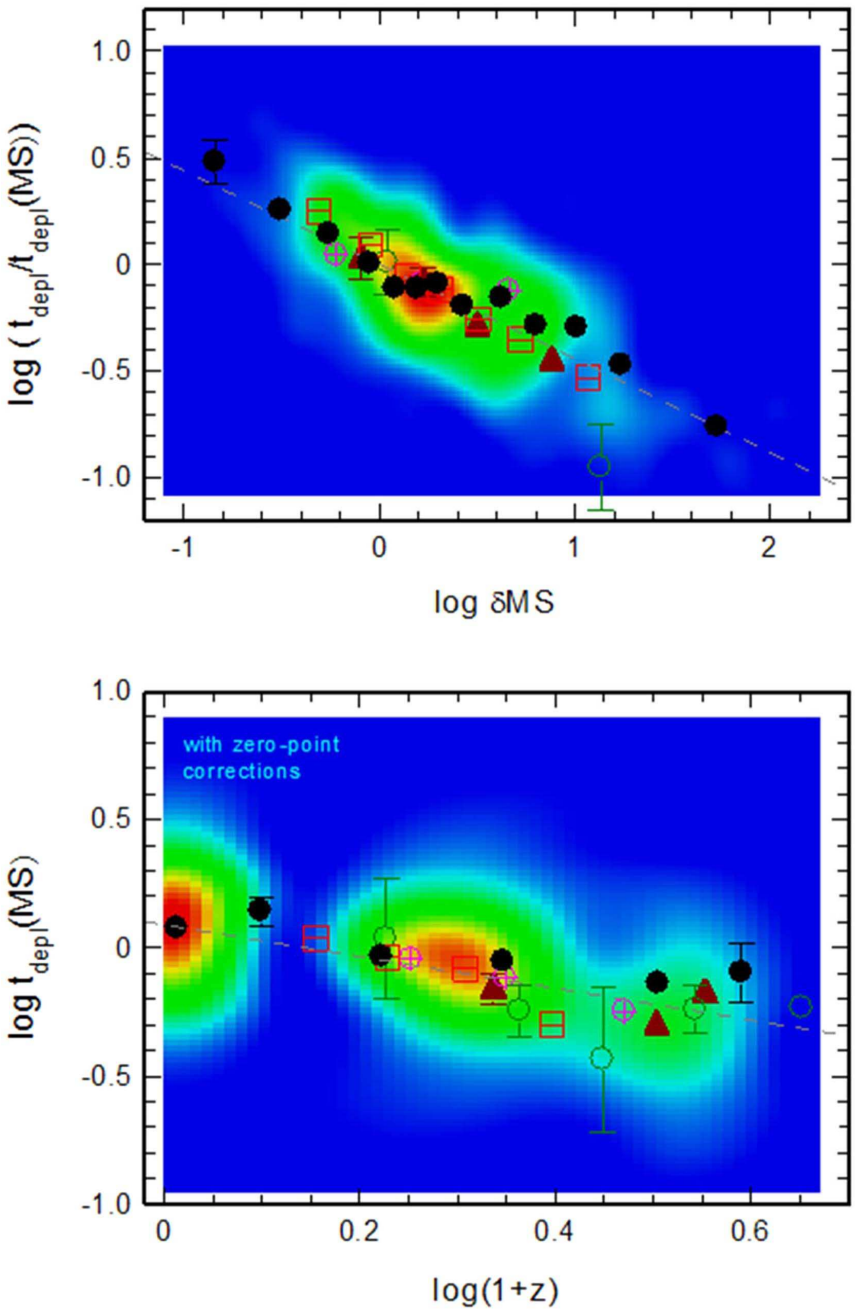

Figure 4.1 – *Dependence of molecular depletion time on departure from MS and on redshift, from Tacconi et al. (2018). Zero-point corrections were introduced for different methods in the literature, in order to minimize the scatter in the depletion time relation.*

dependence of molecular depletion time with redshift and also on the offset from the MS line. Tacconi et al. (2018) concluded that the star formation efficiency (the inverse of depletion time) is increasing with redshift, but only slightly. MS star formation may be driven by similar physical processes at high and low redshift, with some more efficiency at high z, due to the more compact character of distant galaxies.

To study how morphology affects star formation with PHIBSS2 data, Freundlich et al. (submitted) investigated how global parameters such as stellar mass, molecular gas mass and the SFR derived quantities like the depletion time, gas-to-stellar ratio, depend on the bulge-to-total mass ratio and the total surface density (see figure 4.2).

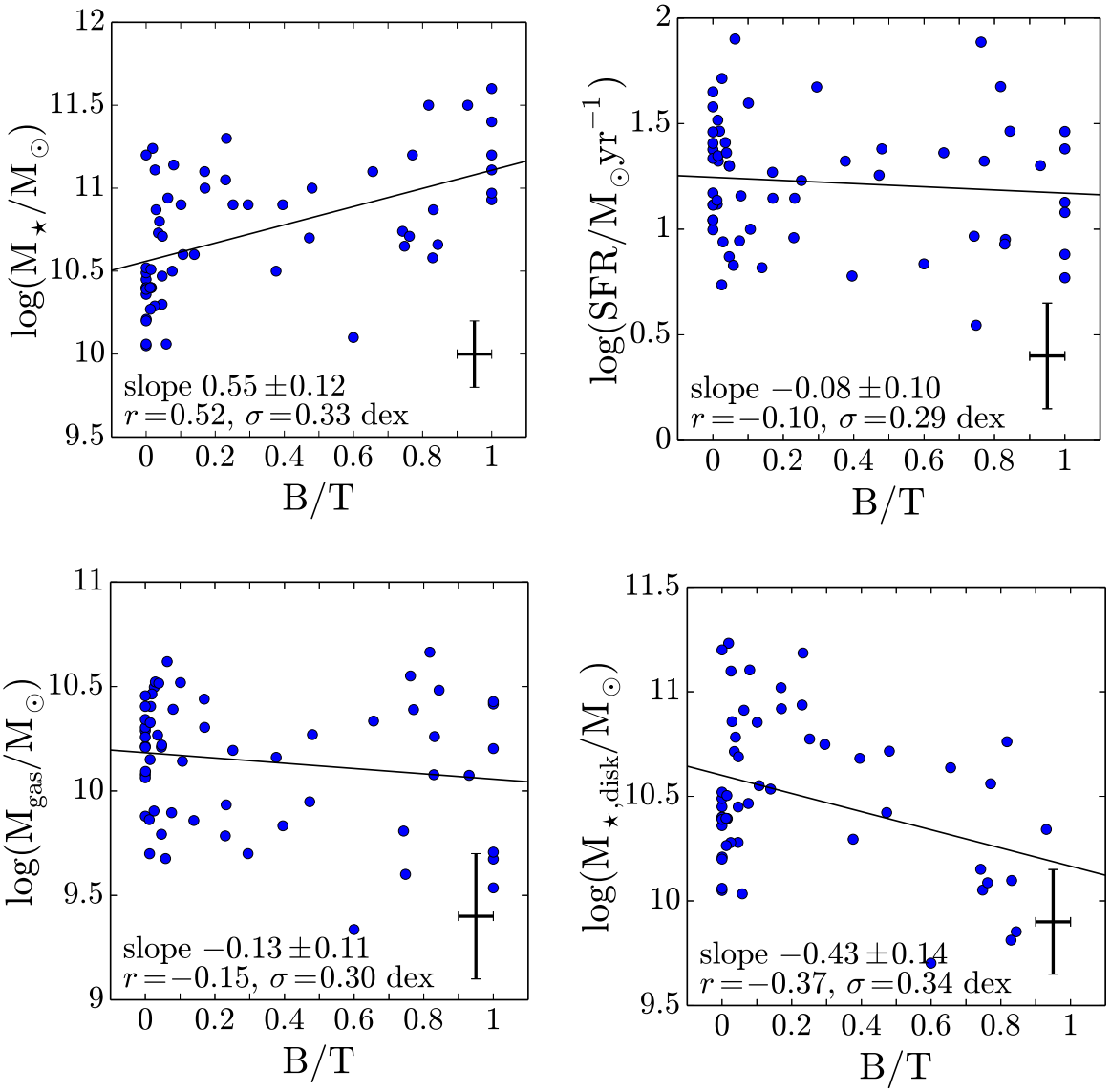

Figure 4.2 – *Galaxy parameters (stellar and gas masses, stellar disk mass and SFR) as a function of the bulge-to-total mass ratio within the PHIBSS2 sample in the range z=0.5-0.8. The black line is the linear least square fit, with 0.3 dex errors*

Most of star-forming galaxies between z=0 and 2.5 lie on the near-linear star-formation law of the MS. At z>1, main-sequence star-forming galaxies double their mass on a typical timescale of $\sim$ 300-500Myr and their growth appears to halt when they reach the Schechter mass. This origin of this quenching is still a challenge to study. Improvements from the IRAM have recently made possible to make a census of the molecular gas contents in the MS galaxies.

One of the main interests for our study was in the galaxies with z<1, where the star-forming galaxies are less massive and the SFR suffers a huge drop with time. In the next sections, we will focus on this range of redshifts.

Sample

The PHIBSS2 sample was chosen on the basis of large imaging surveys with well calibrated stellar masses, SFR and HST morphologies: Great Observatory Origins Deep Survey (GOODS-N) (Giavalisco et al., 2004), Cosmic Evolution Surveys (COSMOS) (Scoville, 2007) and All-Wavelength Extended Groth Strip International Survey (AEGIS) (Davis et al., 2007). The sources selected from these surveys have deep HST images and good UV and Herschel PACS and/or 24 μm observations that contribute to the SFR calculations. The low declination of the COSMOS field sources make them perfect for future follow-ups with ALMA.

The selected galaxies also have Hα and when is possible Hβ and O[III] emission free from atmospheric line contaminations. These was important to determine the SFR and metallicity. We also required 10 measurements in any given parameter, to gain more statistics, considering Poisson errors.

We aimed at a homogeneous coverage of the MS and its scatter in the plane of $M_\star$ and SFR., with a $\log(M_\star/M_\odot) \geqslant 10.1$ a SFR $\geqslant 3.5 M_\odot yr^{-1}$ to assure a high probability of reasonable integration times. The sample from redshifts between z=0.5 - 0.8 of near MS star-forming galaxies which is the focus of our present work is shown in table 4.1.

Observations

Inside the selected redshift range (z=0.5-0.8) we observed in our survey 61 galaxies. Their details are in the table 4.2, where we show the configuration, the integration time, the CO beam, the $\Delta z = z_{CO} - z_{optical}$ where z_{CO} came from a Gaussian fit to the CO line and the experimental RMS noise per 30km/s.

The SFR was calculated using the following equation:

$$\Big(\frac{SFR_{UV+IR}}{M_\odot.yr^{-1}}\Big) = 1.087 \times 10^{-10}\Big(\frac{L_{IR}}{L_\odot} + 3.3\frac{\nu L_\nu(2800\text{Å})}{L\odot}\Big), \tag{4.1}$$

where L_{IR} is the SPITZER μm luminosity extrapolated to the total IR and $\nu L_\nu(2800\text{Å})$ is the UV luminosity calculated from the best fit from Kennicutt (1998); Wuyts et al. (2011a).

The CO integrated fluxes are shown in the table 4.3. For the CO-to-H_2 conversion factor, we use the α_{CO} calculated as a function of metallicity Z as:

#	ID	Field	Source[a]	R.A. Optical	DEC. Optical	$z_{\rm optical}$	$M_\star$[c] ($M_\odot$)	SFR[d] ($M_\odot.yr^{-1}$)
1	XA53	COSMOS	822872	10:02:02.09	+02:09:37.40	0.7000	2.9E+11	47.3
2	XC53	COSMOS	805007*	10:00:58.20	+01:45:59.00	0.6227	8.4E+10	47.1
3	XD53	COSMOS	822965	10:01:58.73	+02:15:34.20	0.7028	8.9E+10	39.5
4	XE53	COSMOS	811360	10:01:00.74	+01:49:53.00	0.5297	2.3E+10	25.5
5	XF53	COSMOS	834187	09:58:33.86	+02:19:50.90	0.5020	1.2E+11	18.6
6	XG53	COSMOS	800405	10:02:16.78	+01:37:25.00	0.6223	1.6E+11	21.0
7	XH53	COSMOS	837919	10:01:09.67	+02:30:00.70	0.7028	5.4E+10	18.2
8	XI53	COSMOS	838956	10:00:24.70	+02:29:12.10	0.7026	2.9E+11	20.3
9	XL53	COSMOS	824759	10:00:28.27	+02:16:00.50	0.7506	1.7E+11	28.6
10	XM53	COSMOS	810344	10:01:53.57	+01:54:14.80	0.7007	4.4E+11	23.9
11	XN53	COSMOS	839268	10:00:11.16	+02:35:41.60	0.6967	1.1E+11	24.2
12	XO53	COSMOS	828590	10:02:51.41	+02:18:49.70	0.6077	2.5E+11	11.7
13	XQ53	COSMOS	838696	10:00:35.69	+02:31:15.60	0.6793	8.3E+10	26.9
14	XR53	COSMOS	816955	10:01:41.85	+02:07:09.80	0.5165	1.9E+11	14.5
15	XT53	COSMOS	823380	10:01:39.31	+02:17:25.80	0.7021	1.1E+11	22.7
16	XU53	COSMOS	831385	10:00:40.37	+02:23:23.60	0.5172	1.9E+10	28.0
17	XV53	COSMOS	850140	10:01:43.66	+02:48:09.40	0.6248	6.3E+10	23.1
18	XW53	COSMOS	824627*	10:00:35.52	+02:16:34.30	0.7503	2.5E+10	13.7
19	L14CO001	COSMOS	831870	10:00:18.91	+02:18:10.10	0.5024	1.5E+10	29.0
20	L14CO004	COSMOS	831386	10:00:40.29	+02:20:32.60	0.6885	2.8E+10	8.8
21	L14CO007	COSMOS	838945	10:00:25.18	+02:29:53.90	0.5015	5.1E+10	4.1
22	L14CO008	COSMOS	820898	09:58:09.07	+02:05:29.76	0.6081	8.8E+10	13.9
23	L14CO009	COSMOS	826687	09:58:56.45	+02:08:06.72	0.6976	2.8E+10	21.4
24	L14CO011	COSMOS	839183	10:00:14.30	+02:30:47.16	0.6985	2.6E+10	29.3
25	L14CO012	COSMOS	838449	10:00:45.53	+02:33:39.60	0.7007	3.9E+10	10.0
26	XA54	AEGIS	30084 (10098)	14:19:17.33	+52:50:35.30	0.6590	1.3E+11	51.7
27	XB54	AEGIS	17329 (5038)	14:19:37.26	+52:51:03.40	0.6702	1.7E+11	29.1
28	XC54	AEGIS	14885 (4097)	14:19:49.14	+52:52:35.80	0.5093	1.6E+11	37.9
29	XD54	AEGIS	24556 (8538)	14:19:46.35	+52:54:37.20	0.7541	2.3E+10	28.9
30	XE54	AEGIS	25608 (8310)	14:19:35.27	+52:52:49.90	0.5090	2.5E+10	11.0
31	XF54	AEGIS	32878 (11378)	14:19:41.70	+52:55:41.30	0.7683	5.1E+10	19.9
32	XG54	AEGIS	3654 (169)	14:20:13.43	+52:54:05.90	0.6593	1.4E+11	14.4
33	XH54	AEGIS	30516 (10745)	14:19:45.42	+52:55:51.00	0.7560	1.9E+10	13.1
34	L14EG006	AEGIS	23488 (7652)	14:18:45.52	+52:43:24.10	0.5010	3.0E+10	7.4
35	L14EG008	AEGIS	21351 (7021)	14:19:39.46	+52:52:33.60	0.7315	8.7E+10	79.5
36	L14EG009	AEGIS	31909 (11332)	14:20:04.88	+52:59:38.84	0.7359	1.1E+10	9.9
37	L14EG010	AEGIS	4004 (725)	14:20:22.80	+52:55:56.28	0.6702	5.5E+10	9.3
38	L14EG011	AEGIS	6274	14:20:26.20	+52:57:04.85	0.5705	5.4E+10	25.7
39	L14EG012	AEGIS	6449 (515)	14:19:52.95	+52:51:11.06	0.5447	1.1E+11	9.1
40	L14EG014	AEGIS	9743	14:20:33.58	+52:59:17.46	0.7099	8.5E+10	5.9
41	L14EG015	AEGIS	26964	14:20:45.61	+53:05:31.18	0.7369	9.3E+10	13.4
42	L14EG016	AEGIS	34302	14:18:28.90	+52:43:05.28	0.6445	4.0E+10	6.6
43	XA55	GOODS-N	21285 (9335)*	12:36:59.92	+62:14:50.00	0.7610	2.8E+10	44.7
44	XB55	GOODS-N	6666 (3091)†	12:36:08.13	+62:10:35.90	0.6790	4.5E+10	23.1
45	XC55	GOODS-N	19725 (8738)	12:36:09.76	+62:14:22.60	0.7800	4.6E+10	29.1
46	XD55	GOODS-N	12097 (5385)	12:36:21.04	+62:12:08.50	0.7790	3.1E+10	21.6
47	XE55	GOODS-N	19815 (8798)*	12:36:11.26	+62:14:20.90	0.7720	3.3E+10	14.8
48	XF55	GOODS-N	7906 (3565)	12:35:55.43	+62:10:56.80	0.6382	1.1E+10	11.1
49	XG55	GOODS-N	19257 (8697)	12:37:02.93	+62:14:23.60	0.5110	3.8E+10	8.5
50	XH55	GOODS-N	16987 (7668)	12:37:13.87	+62:13:35.00	0.7784	1.6E+10	13.0
51	XL55	GOODS-N	10134 (4568)	12:37:10.56	+62:11:40.70	0.7880	3.2E+10	22.2
52	L14GN006	GOODS-N	30883 (12248)	12:36:34.41	+62:17:50.50	0.6825	2.5E+10	23.8
53	L14GN007	GOODS-N	939 (334)	12:36:32.38	+62:07:34.10	0.5950	7.4E+10	8.9
54	L14GN008	GOODS-N	11532 (5128)	12:36:07.83	+62:12:00.60	0.5035	1.9E+10	5.5
55	L14GN018	GOODS-N	25413 (10807)	12:36:31.66	+62:16:04.10	0.7837	2.5E+10	32.8
56	L14GN021	GOODS-N	8738 (3875)	12:36:03.26	+62:11:10.98	0.6380	5.1E+10	76.9
57	L14GN022	GOODS-N	11460 (5127)*	12:36:36.76	+62:11:56.09	0.5561	1.3E+10	6.8
58	L14GN025	GOODS-N	36596 (14032)	12:37:13.99	+62:20:36.60	0.5320	4.5E+10	3.5
59	L14GN032	GOODS-N	21683 (9558)	12:37:16.32	+62:15:12.30	0.5605	1.3E+11	7.6
60	L14GN033	GOODS-N	1964 (918)	12:36:53.81	+62:08:27.70	0.5609	1.1E+10	6.7
61	L14GN034	GOODS-N	33895	12:36:19.68	+62:19:08.10	0.5200	7.4E+10	8.7

Table 4.1 – *Sample*

#	ID	Field	Source	Config.	$t_{\rm int}$ (hr)	CO beam	Δz^a	$s_{\rm peak}{}^c$ (mJy)
1	XA53	COSMOS	822872	D	2.2	$4.9'' \times 3.9''$	−0.0018	3.9
2	XC53	COSMOS	805007*	D	3.8	$4.4'' \times 3.4''$	−0.0064	0.8
3	XD53	COSMOS	822965	D	4.3	$4.2'' \times 2.3''$	−0.0008	3.5
4	XE53	COSMOS	811360	D	1.7	$5.4'' \times 3.4''$	−0.0007	5.4
5	XF53	COSMOS	834187	D	0.6	$4.7'' \times 2.8''$	−0.0001	3.2
6	XG53	COSMOS	800405	D	5.3	$3.0'' \times 2.0''$	−0.0006	1.9
7	XH53	COSMOS	837919	C	9.4	$2.7'' \times 2.0''$	−0.0009	2.1
8	XI53	COSMOS	838956	C	3.5	$2.6'' \times 1.9''$	−0.0015	3.4
9	XL53	COSMOS	824759	C	3.3	$3.0'' \times 1.8''$	−0.0017	1.8
10	XM53	COSMOS	810344	C	3.9	$2.8'' \times 1.9''$	−0.0002	1.4
11	XN53	COSMOS	839268	C	5.4	$4.6'' \times 3.8''$	−0.0002	2.6
12	XO53	COSMOS	828590	C	6.3	$3.4'' \times 1.6''$	−0.0018	1.2
13	XQ53	COSMOS	838696	D	4.3	$4.4'' \times 3.8''$	−0.0012	2.9
14	XR53	COSMOS	816955	D	3.7	$3.5'' \times 2.3''$	−0.0003	2.2
15	XT53	COSMOS	823380	D	3.9	$4.1'' \times 2.6''$	−0.0009	2.3
16	XU53	COSMOS	831385	D	2.2	$3.9'' \times 2.0''$	−0.0008	2.4
17	XV53	COSMOS	850140	C	4.2	$2.5'' \times 1.8''$	−0.0012	2.7
18	XW53	COSMOS	824627*	C	4.1	$3.1'' \times 1.8''$	−0.0005	3.3
19	L14CO001	COSMOS	831870	CD	3.5	$3.0'' \times 2.2''$	−0.0003	4.1
20	L14CO004	COSMOS	831386	CD	14.2	$2.8'' \times 1.5''$	−0.0011	0.6
21	L14CO007	COSMOS	838945	D	8.3	$5.2'' \times 2.8''$	−0.0001	1.1
22	L14CO008	COSMOS	820898	D	7.5	$4.2'' \times 2.8''$	−0.0016	1.3
23	L14CO009	COSMOS	826687	CD	7	$3.1'' \times 1.4''$	−0.0001	1.4
24	L14CO011	COSMOS	839183	CD	5.6	$4.4'' \times 2.8''$	−0.0016	2.5
25	L14CO012	COSMOS	838449	CD	4.2	$3.2'' \times 1.5''$	−0.0011	3.9
26	XA54	AEGIS	30084	ABD	30.3	$0.8'' \times 0.7''$	−0.0005	2.7
27	XB54	AEGIS	17329	D	4.7	$5.3'' \times 2.9''$	−0.0006	4.0
28	XC54	AEGIS	14885	D	2.6	$3.2'' \times 2.6''$	+0.0000	1.8
29	XD54	AEGIS	24556	D	11.3	$4.5'' \times 3.0''$	−0.0008	2.2
30	XE54	AEGIS	25608	D	1.8	$3.3'' \times 2.7''$	−0.0004	2.2
31	XF54	AEGIS	32878	D	9	$4.8'' \times 4.3''$	+0.0000	2.1
32	XG54	AEGIS	3654	D	7	$4.5'' \times 3.7''$	−0.0003	2.7
33	XH54	AEGIS	30516	C	10.6	$2.5'' \times 2.3''$	−0.0003	1.4
34	L14EG006	AEGIS	23488	D	10.2	$3.9'' \times 2.8''$	−0.0005	2.8
35	L14EG008	AEGIS	21351	AC	27	$2.6'' \times 2.1''$	−0.0002	4.2
36	L14EG009	AEGIS	31909	CD	10	$2.7'' \times 1.8''$	−0.0005	1.5
37	L14EG010	AEGIS	4004	CD	9.4	$2.3'' \times 2.3''$	−0.0007	4.8
38	L14EG011	AEGIS	6274	D	6.8	$3.2'' \times 2.9''$	−0.0005	1.9
39	L14EG012	AEGIS	6449	D	4.8	$3.2'' \times 2.3''$	−0.0009	2.6
40	L14EG014	AEGIS	9743	CD	9.2	$1.7'' \times 1.7''$	−0.0002	1.1
41	L14EG015	AEGIS	26964	CD	10	$1.9'' \times 1.6''$	−0.0013	1.1
42	L14EG016	AEGIS	34302	CD	8.1	$1.6'' \times 1.3''$	−0.0011	0.8
43	XA55	GOODS-N	21285*	D	4.3	$4.9'' \times 3.1''$	−0.0001	2.3
44	XB55	GOODS-N	6666†	D	9.3	$3.7'' \times 2.8''$		
45	XC55	GOODS-N	19725	D	5.8	$5.5'' \times 3.4''$	−0.0002	2.2
46	XD55	GOODS-N	12097	D	9.5	$4.5'' \times 4.3''$	−0.0004	1.8
47	XE55	GOODS-N	19815*	D	12.7	$4.6'' \times 4.0''$	−0.0040	1.2
48	XF55	GOODS-N	7906	D	10.9	$4.2'' \times 3.5''$	−0.0008	0.5
49	XG55	GOODS-N	19257	ABCD	8.9	$4.0'' \times 3.7''$	−0.0003	1.5
50	XH55	GOODS-N	16987	C	9.4	$2.5'' \times 2.0''$	−0.0001	1.1
51	XL55	GOODS-N	10134	D	14.3	$4.1'' \times 3.5''$	+0.0000	0.9
52	L14GN006	GOODS-N	30883	D	2.6	$3.4'' \times 3.1''$	−0.0005	2.3
53	L14GN007	GOODS-N	939	D	4.2	$2.8'' \times 2.3''$	−0.0001	1.6
54	L14GN008	GOODS-N	11532	D	14.3	$3.2'' \times 2.8''$	−0.0004	0.7
55	L14GN018	GOODS-N	25413	CD	10.3	$2.6'' \times 2.1''$	−0.0005	1.9
56	L14GN021	GOODS-N	8738	CD	4.6	$2.0'' \times 1.4''$	−0.0002	3.1
57	L14GN022	GOODS-N	11460*	CD	16.9	$1.5'' \times 1.4''$	+0.0000	1.1
58	L14GN025	GOODS-N	36596	CD	10.5	$1.9'' \times 1.2''$	−0.0008	1.0
59	L14GN032	GOODS-N	21683	CD	4.7	$3.4'' \times 2.3''$	−0.0004	2.3
60	L14GN033	GOODS-N	1964	D	15.9	$2.5'' \times 2.1''$	−0.0003	1.0
61	L14GN034	GOODS-N	33895	D	7.2	$2.8'' \times 2.1''$	−0.0004	1.6

Table 4.2 – *Observations*

#	ID	Field	Source	F(CO)[a] (Jy.km.s^{-1})	dF(CO) (Jy.km.s^{-1})	SNR[b]	$L_{CO(2-1)}$[c] (K.km.s^{-1}.pc^{-2})	M_{gas}[d] ($M_\odot$)	f_{gas}[f] (Gyr)	t_{depl}[g]
1	XA53	COSMOS	822872	1.45	0.46	3.2	9.4E+09	4.6E+10	0.14	1.0
2	XC53	COSMOS	805007⋆	0.20	0.08	2.5	1.0E+09	5.0E+09	0.06	0.1
3	XD53	COSMOS	822965	1.00	0.24	4.2	6.6E+09	3.3E+10	0.27	0.8
4	XE53	COSMOS	811360	1.29	0.45	2.9	4.7E+09	2.6E+10	0.53	1.0
5	XF53	COSMOS	834187	1.71	0.46	3.7	5.6E+09	2.8E+10	0.19	1.5
6	XG53	COSMOS	800405	0.98	0.25	4.0	5.0E+09	2.5E+10	0.13	1.2
7	XH53	COSMOS	837919	0.26	0.10	2.6	1.7E+09	8.8E+09	0.14	0.5
8	XI53	COSMOS	838956	0.37	0.10	3.5	2.4E+09	1.2E+10	0.04	0.6
9	XL53	COSMOS	824759	0.71	0.19	3.8	5.3E+09	2.6E+10	0.14	0.9
10	XM53	COSMOS	810344	0.83	0.20	4.1	5.4E+09	2.7E+10	0.06	1.1
11	XN53	COSMOS	839268	0.58	0.17	3.5	3.7E+09	1.9E+10	0.14	0.8
12	XO53	COSMOS	828590	0.67	0.13	5.2	3.3E+09	1.6E+10	0.06	1.4
13	XQ53	COSMOS	838696	0.51	0.19	2.7	3.1E+09	1.6E+10	0.16	0.6
14	XR53	COSMOS	816955	0.50	0.11	4.5	1.8E+09	8.6E+09	0.04	0.6
15	XT53	COSMOS	823380	0.67	0.18	3.7	4.4E+09	2.2E+10	0.16	1.0
16	XU53	COSMOS	831385	0.82	0.15	5.7	2.9E+09	1.6E+10	0.46	0.6
17	XV53	COSMOS	850140	1.26	0.28	4.5	6.5E+09	3.3E+10	0.34	1.4
18	XW53	COSMOS	824627⋆	0.17	0.08	2.2	1.3E+09	7.3E+09	0.22	0.5
19	L14CO001	COSMOS	831870	0.90	0.20	4.5	3.0E+09	1.7E+10	0.52	0.6
20	L14CO004	COSMOS	831386	0.23	0.07	3.4	1.4E+09	8.0E+09	0.22	0.9
21	L14CO007	COSMOS	838945	0.42	0.12	3.4	1.4E+09	6.9E+09	0.12	1.7
22	L14CO008	COSMOS	820898	0.84	0.17	4.9	4.1E+09	2.0E+10	0.19	1.5
23	L14CO009	COSMOS	826687	0.41	0.10	3.9	2.7E+09	1.5E+10	0.34	0.7
24	L14CO011	COSMOS	839183	0.70	0.10	7.4	4.5E+09	2.5E+10	0.50	0.9
25	L14CO012	COSMOS	838449	0.40	0.11	3.7	2.6E+09	1.4E+10	0.26	1.4
26	XA54	AEGIS	30084	1.11	0.10	11.1	6.4E+09	3.1E+10	0.20	0.6
27	XB54	AEGIS	17329	1.00	0.25	4.1	6.0E+09	2.9E+10	0.14	1.0
28	XC54	AEGIS	14885	1.17	0.27	4.4	4.0E+09	1.9E+10	0.11	0.5
29	XD54	AEGIS	24556	0.50	0.08	6.1	3.8E+09	2.2E+10	0.49	0.8
30	XE54	AEGIS	25608	0.66	0.25	2.7	2.2E+09	1.2E+10	0.33	1.1
31	XF54	AEGIS	32878	0.40	0.11	3.5	3.2E+09	1.7E+10	0.24	0.8
32	XG54	AEGIS	3654	0.87	0.17	5.0	5.0E+09	2.5E+10	0.15	1.7
33	XH54	AEGIS	30516	0.11	0.03	3.4	8.4E+08	5.0E+09	0.21	0.4
34	L14EG006	AEGIS	23488	0.36	0.08	4.3	1.2E+09	6.2E+09	0.17	0.8
35	L14EG008	AEGIS	21351	1.16	0.10	12.0	8.3E+09	4.2E+10	0.32	0.5
36	L14EG009	AEGIS	31909	0.43	0.13	3.4	3.1E+09	2.0E+10	0.64	2.0
37	L14EG010	AEGIS	4004	0.21	0.06	3.7	1.3E+09	6.4E+09	0.10	0.7
38	L14EG011	AEGIS	6274	0.85	0.18	4.7	3.7E+09	1.9E+10	0.26	0.7
39	L14EG012	AEGIS	6449	0.32	0.10	3.3	1.2E+09	6.1E+09	0.05	0.7
40	L14EG014	AEGIS	9743	0.14	0.08	1.8	9.4E+08	4.7E+09	0.05	0.8
41	L14EG015	AEGIS	26964	0.14	0.04	3.5	1.0E+09	5.1E+09	0.05	0.4
42	L14EG016	AEGIS	34302	0.25	0.08	3.1	1.4E+09	7.2E+09	0.15	1.1
43	XA55	GOODS-N	21285⋆	0.38	0.12	3.2	2.9E+09	1.6E+10	0.37	0.4
44	XB55	GOODS-N	6666†	< 0.46			< 2.8E+09	< 1.5E+10	< 0.25	< 0.6
45	XC55	GOODS-N	19725	0.70	0.14	5.0	5.7E+09	3.0E+10	0.40	1.0
46	XD55	GOODS-N	12097	0.40	0.12	3.4	3.2E+09	1.8E+10	0.37	0.8
47	XE55	GOODS-N	19815⋆	0.27	0.11	2.5	2.1E+09	1.2E+10	0.26	0.8
48	XF55	GOODS-N	7906	0.23	0.09	2.6	1.2E+09	7.6E+09	0.40	0.7
49	XG55	GOODS-N	19257	0.68	0.17	3.9	2.3E+09	1.2E+10	0.24	1.4
50	XH55	GOODS-N	16987	0.25	0.07	3.4	2.0E+09	1.2E+10	0.43	1.0
51	XL55	GOODS-N	10134	0.46	0.18	2.6	3.8E+09	2.1E+10	0.40	1.0
52	L14GN006	GOODS-N	30883	0.82	0.20	4.2	5.1E+09	2.9E+10	0.53	1.2
53	L14GN007	GOODS-N	939	0.78	0.17	4.5	3.7E+09	1.8E+10	0.20	2.0
54	L14GN008	GOODS-N	11532	0.44	0.12	3.6	1.5E+09	8.0E+09	0.29	1.5
55	L14GN018	GOODS-N	25413	0.30	0.07	4.2	2.5E+09	1.4E+10	0.36	0.4
56	L14GN021	GOODS-N	8738	1.28	0.21	6.1	6.9E+09	3.6E+10	0.41	0.5
57	L14GN022	GOODS-N	11460⋆	0.09	0.04	2.3	3.7E+08	2.2E+09	0.15	0.3
58	L14GN025	GOODS-N	36596	0.21	0.06	3.5	7.8E+08	4.0E+09	0.08	1.1
59	L14GN032	GOODS-N	21683	0.17	0.08	2.1	7.0E+08	3.4E+09	0.03	0.5
60	L14GN033	GOODS-N	1964	0.19	0.06	3.0	7.9E+08	4.7E+09	0.29	0.7
61	L14GN034	GOODS-N	33895	1.90	0.31	6.2	6.7E+09	3.3E+10	0.31	3.8

Table 4.3

$$\alpha_{CO} = \alpha_G(0.67 \times exp(0.36 \times 10^{8.67-logZ}) \times 10^{-1.27(logZ-8.67)})^{1/2}, \quad (4.2)$$

where $logZ = 12 + 8.47 - 0.087 \times (log(M_\star) - b)^2$ from Pettini & Pagel (2004); and from Genzel et al. (2015) with $b = 10.4 + 4.46 \times (log(1+z))^2$. This metallicity correction have the average result of $\alpha_{CO} = 4.0 \pm 0.3 M_\odot/(Kkm/spc^{-1})$. The luminosity conversion factor that we assume is $r_{12} = 0.72$ that already used by Genzel et al. (2015) and Tacconi et al. (2018).

The Kennicutt-Schmidt relation in PHIBSS2

One part of my work in PHIBSS2 was to analyse the KS relation with a statistical perspective. This section will be focused primally on the statistical aspects of our observations for the KS relation

The relation is usually fitted by a power-law of slope N. The value N=1 of the power-law is generally obtained from MS when averaging the SFR and molecular gas over the galaxy as a whole, and also even at subgalactic scale, as we saw in the previous chapter. The power-law exponent in the KS relation may vary because of the different evolutionary stages of the molecular clouds in galaxies. Even within the same galaxy, there can be widely different star formation efficiencies.

The parameters controlling the KS relationship are intrinsically linked to the mean and dispersion in the KS slope. These parameters are specifically the SFR and the gas surface density, which can be estimated in the galaxy samples that we have selected. Therefore, if we want to fit a model for this kind of relationship it is necessary to consider each parameter, over a wide range of different galaxies. For example, we can use star forming galaxies on the MS, URLIGS and also subgalatic structures.

Besides, it is important to consider many kinds of fitting models, for example linear fits to a set of points in log-log two dimensional plane (i.e. power-laws). Certainly, the star formation properties of each galaxy will be influenced by physical processes that are linked to their surface density. Measurement uncertainties can produce significant biases when one fits a model.

For estimating the parameters of the KS relationship for each galaxy one needs a rigorous treatment of scatter about the regression line. Shetty et al. (2013) use the regression line to estimate the parameters. In our case, we use this concept in our data of PHIBSS2, see figure 4.3. Contrary to Shetty et al. (2013), we use a weighted least-square fitting, adapted to the log space. Mathematically speaking, standard weighted least-squares fitting is only appropriate when there is a dimension along which the data points have negligible uncertainties. It is however difficult to have negligible uncertainties in the parameters of SFR and principally in surface density. For this reason, we chose to do different weights for different kinds of observations: with URLIGS in Combes et al.

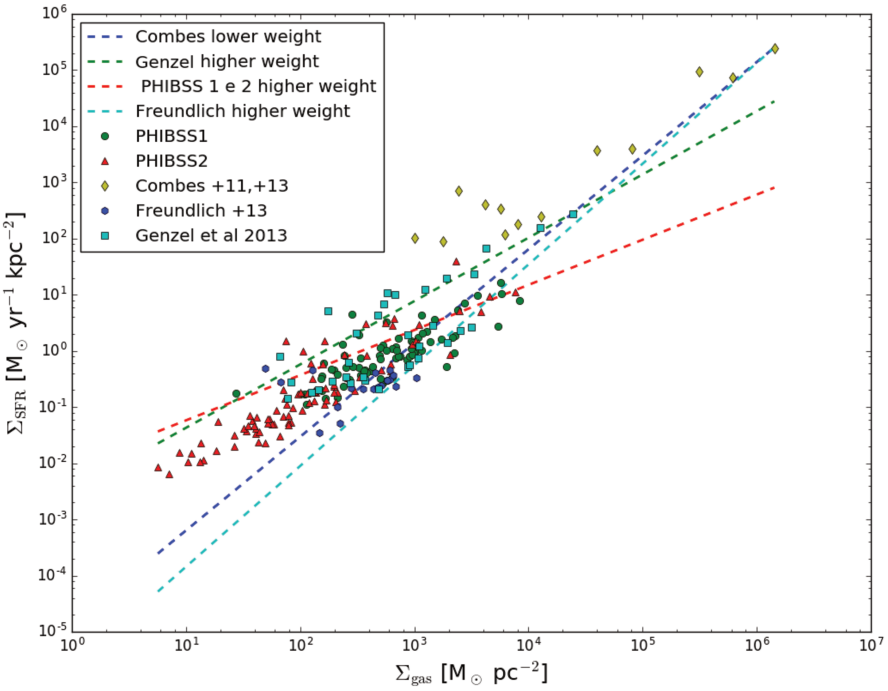

Figure 4.3 – *KS relation using a weighted least-square fitting. The data are from Combes et al. (2013) Freundlich et al. (2013), Genzel et al. (2013) and PHIBSS. In these fits, we give a lower weight for the URLIGS sample above the MS, and a higher weight for the MS galaxies.*

(2013), subgalactic scales from Freundlich et al. (2013), Genzel et al. (2013) and PHIBSS data. Depending on the kind of data chosen there will be a different scatter for this relation. In the case of URLIGS which are starbursts with a very efficient SFR, the fits and slopes are expected to be different. However, this is only the beginning of this kind of study, and more investigations are necessary for a statical analysis. For example, if a depletion time of 1 Gyr is observed on the MS at these redshifts, figure 4.4 shows that URLIGS have a much lower depletion time-scale.

Using just the PHIBSS sample and also the corresponding linear fit, we obtain the result of figure 4.5 (from Freundlich et al submitted). Figure 4.5 shows the KS relation from the PHIBSS2 z=05-0.8 with a linear exponent N=0.98±0.11, i.e. almost linear. The depletion time is constant t_{dep} = 0.9Gyr, it agrees with Tacconi et al. (2018) at z=0.65, intermediate between the values from molecular gas at z∼0 and z=1-3, Saintonge et al. (2017) with COLD GASS survey with a t_{dep} = 1.05Gyr and Tacconi et al. (2013) from the first PHIBSS sample with t_{dep} = 0.8Gyr, respectively.

Freundlich et al (submitted) showed a difference in the scatter in the KS relation, when taking the disk size $R_{d,1/2}$ instead of the global half-light radius $R_{1/2}$ to define the surface density. This can reduce the scatter from 0.27 dex with $R_{1/2}$ to 0.19 with $R_{d,1/2}$. It is coherent that the star formation occurs within the disk and not in the bulge. This result is important to show the relevance of the KS relation study: deriving this relation

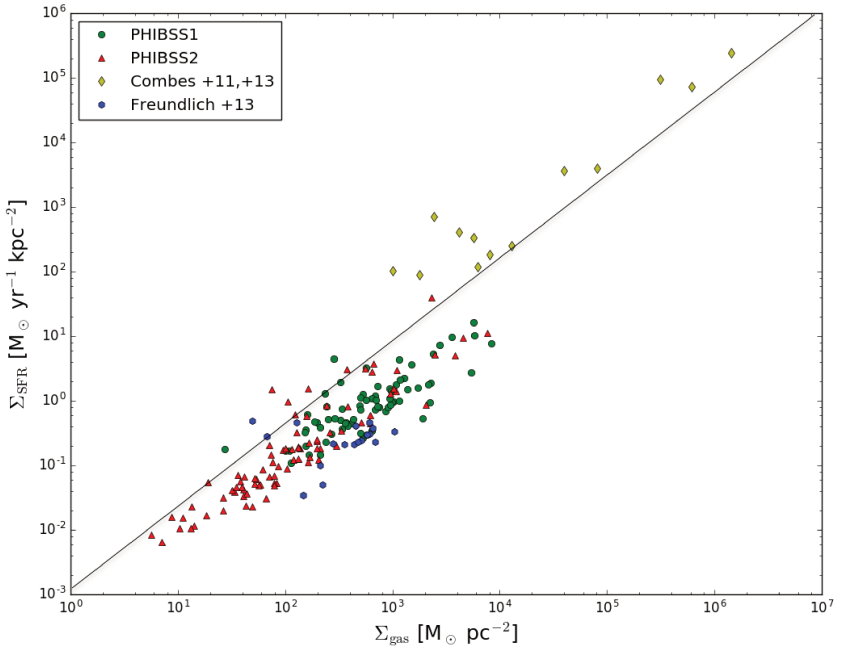

Figure 4.4 – *KS relation with different data sample from the figure 4.3. The line corresponds to a depletion time of1 Gyr.*

could lead to a more systematic study of the conditions in which stars are formed.

Resolved galaxies with NOEMA

In our PHIBBS2 sample, we found 3 galaxies with a good probability to resolve: EG008, XA54 and XG55 (ID corresponding to the tables 4.1,4.2 and 4.3). These resolved galaxies were then designed to me for the dynamical and kinematic study. Here I present the results of this study.

NOEMA re-observed some galaxies with greater resolution, when the signal-to-noise was sufficient and the morphology extended. From their data cubes we can extract the position-velocity (PV) diagrams, the various channel maps, and the three moments (zero for integrated emission, one for the velocity map, and two for the velocity dispersion). From the PV diagram, we can extract some important information, e.g the kinematics and the clumps. This is extremely important if we want to have a deeper analysis in some different parts of the galaxy. From the three mapped galaxies,

From the three mapped galaxies:,one is well resolved which one could do position-velocity maps (EG008), another is resolved but compact (XA54) and the last one is not resolved (XG55).

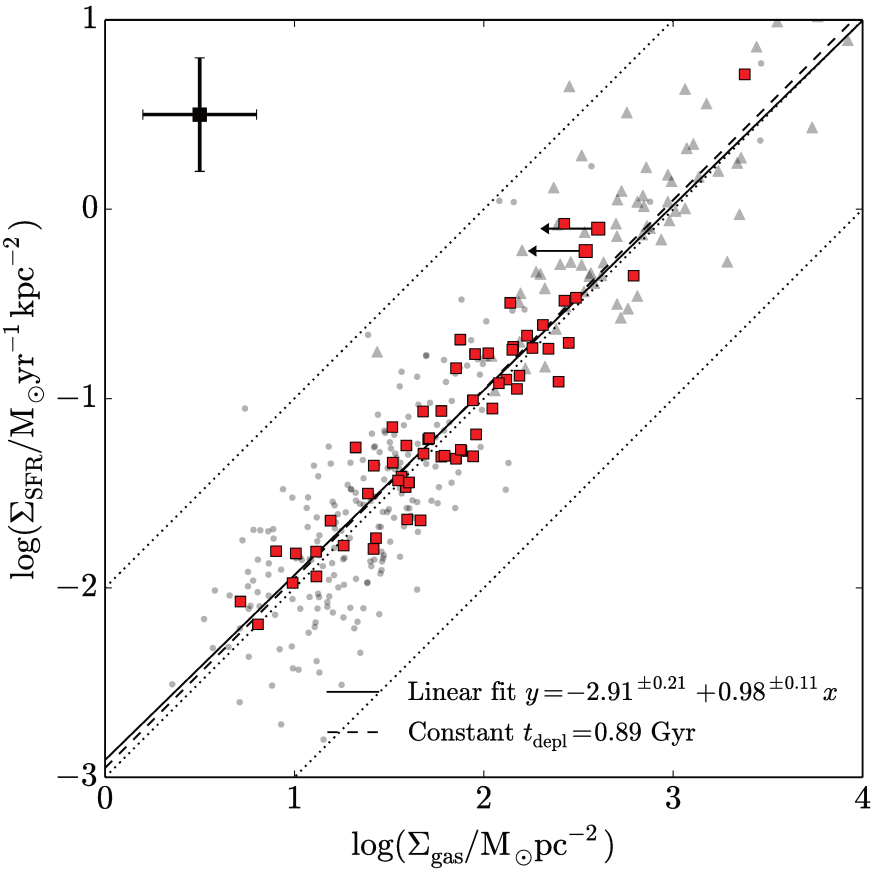

Figure 4.5 – *KS relation from PHIBSS2 sample at z = 0.5-0.8.The dotted diagonal lines correspond to constant depletion times of 0.1, 1 and 10 Gyr from top to bottom and the 0.3 dex errors assumed to assess the uncertainties are displayed at the upper left. The detections from PHIBSS2 are indicated by the red squares and upper limits by arrows. The grey dot points are from COLDGASS data from Saintonge et al. (2011) and the triangles are from Tacconi et al. (2013). The black solid line corresponds to a linear least square fits to the data points; the dashed lines to a constant depletion time corresponding to the best-fitting value on the KS diagram. (Freundlich et al. submitted)*

The figure 4.6 shows the maps in different velocity channels of the galaxy EG008, the velocity map and also the PV diagram. This galaxy is clearly resolved. The same for the figure 4.7 of the galaxy XA54: the velocity map shows that this galaxy is compact. ForXG55, and figure 4.8 we could just produce a position for some channels.

These results will be used in the next chapter where we compare the resolved KS maps of these galaxies with our new ALMA data.

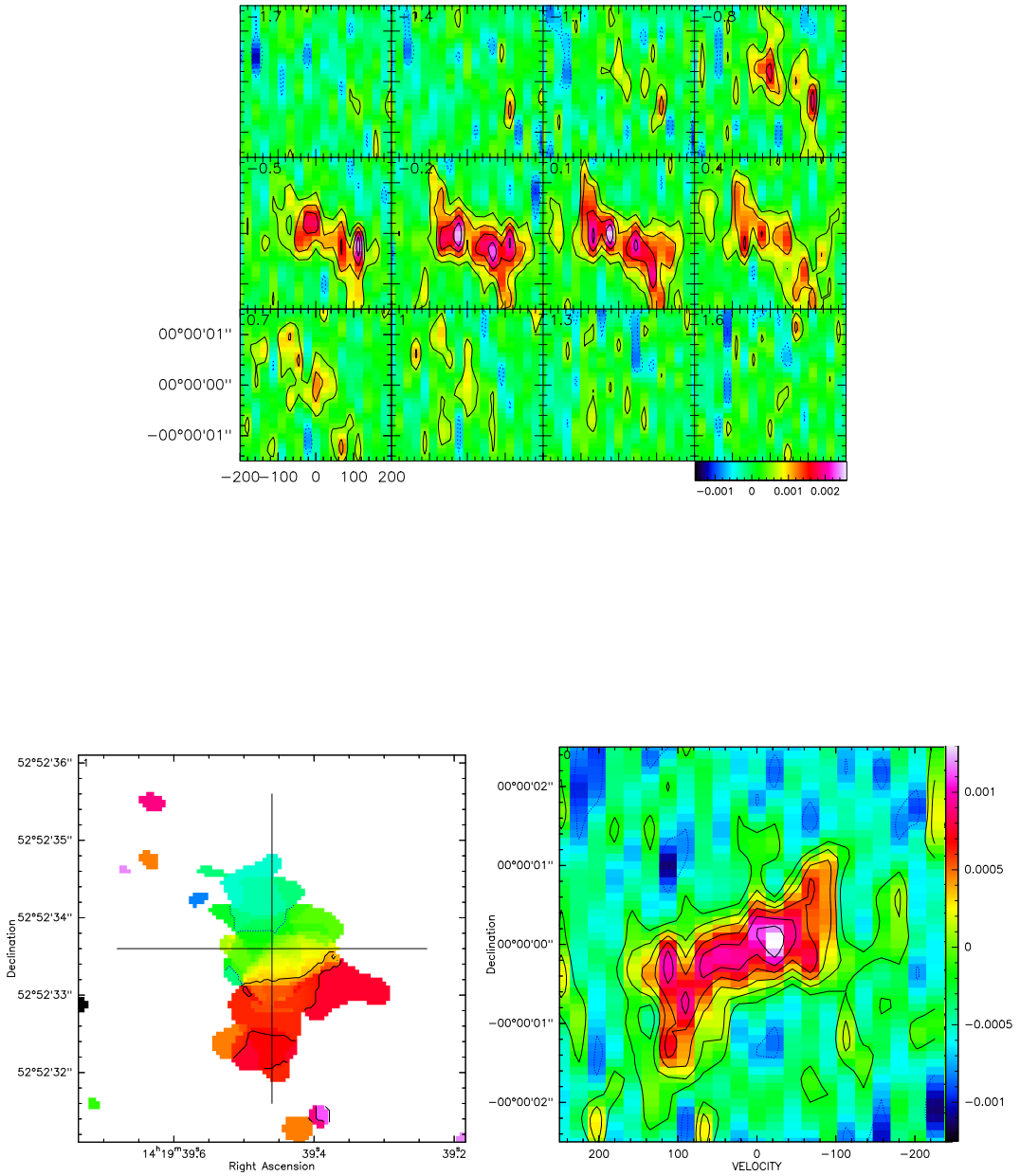

Figure 4.6 – *EG008 maps. The bottom image is the position of the galaxy with a velocity range for different channels. The left is the velocity map and the right one is the PV diagram on PA= 45 degree.*

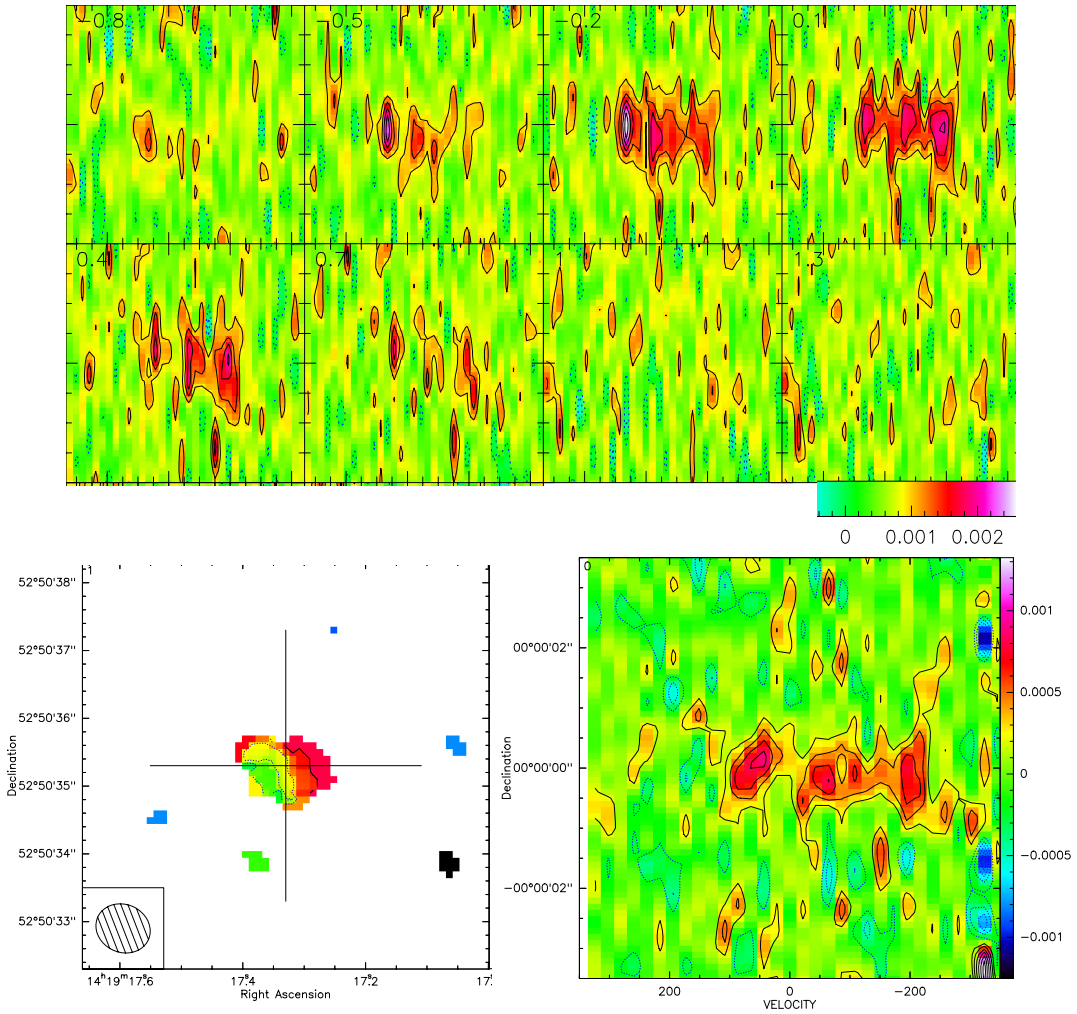

Figure 4.7 – *Same than 4.6 but for XA54. In this case, the galaxy is compact, but at least we can separate some regions through the PV diagram.*

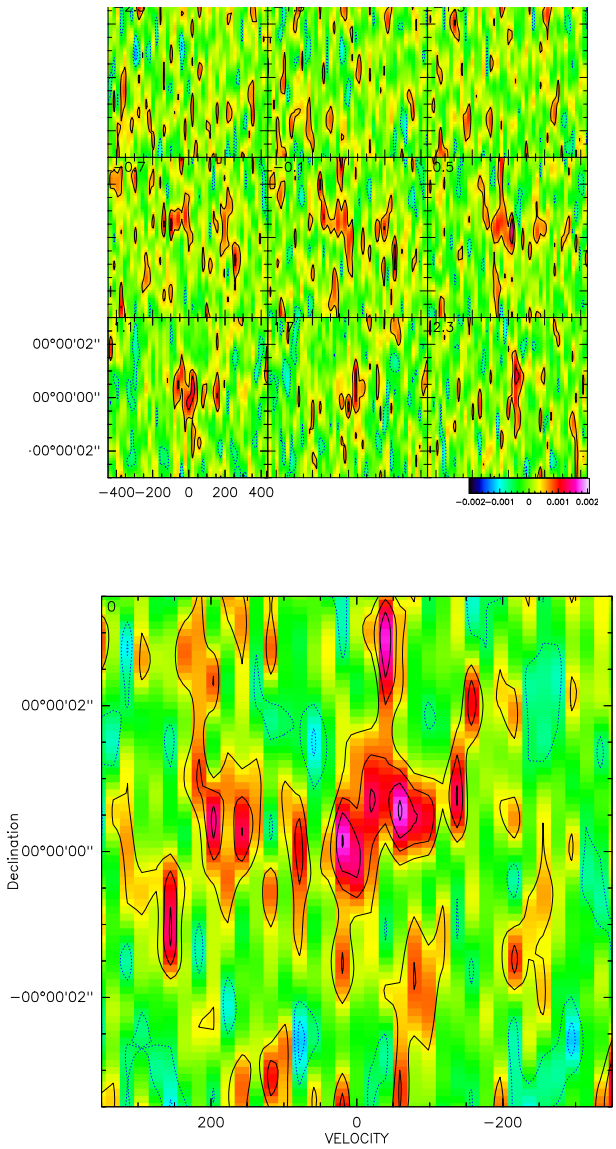

Figure 4.8 – *Same than 4.6 but for XG55. in this case we can not plot any velocity map since the source is not resolved.*

CHAPTER 5

ALMA

The KS relation obtained with spatial resolved mappings is linear with a constant molecular depletion time on smaller scales (Bigiel 2008, 2011, Lereoy 2008, Schrua 2011). It already told in this thesis,it is still difficult to obtain a resolved KS, principally due to the challenges to have better resolutions. In the previous works with PHIBSS it was possible to have a KS relation in kpc-sized substructures. Nevertheless, both studies from Freundlich et al. (2013) and Genzel et al. (2013) resolved just smoothed clump ensembles.

In order to continue investigate in detail the star formation processes and the fate of the star-forming regions after the peak epoch of star formation, we propose to expanded with new emissions. The continuity of this works is extreme important, principally with ALMA. The resolution of ALMA could have another perspective for this study, not in smooth clumps but at the scale of the star-forming regions. This was the principal reason that our group continue this project with ALMA follow-up.

Observations

The CO emission was observed with ALMA for 12 galaxies choosing from the PHIBSS2 program. There were two observations in Cycle 3 and 4, of 7.9 hours for the first and 8.3 hours for the second (PI: Jonathan Freundlich). This observation was in order to propose a high-resolution CO line and dust continuum imaging program of a sample of six massive star-forming galaxies at z=0.7 (Cycle 3) and z=0.5-0.6 (Cycle4).

The Cycle 3 it was observed the CO(4-3) emission in the band 6 with an angular resolution of 0.05". For the Cycle 4 it was observed CO(3-2) emission in the band 6 with an angle resolution between 0.143-1.156".

The data were calibrated using the CASA reduction package. Approximately 36% of the data was flagged which was current at this epoch for 12m Array data. We produced a CO cube for each galaxy with natural weighting a velocity range of -1000 to 1000 a

ID in PHIBSS	Field and Source	Line	R.A. Optical	DEC. Optical	$z_{\rm optical}$	$M_\star$ ($M_\odot$)	SFR ($M_\odot.yr^{-1}$)
XA53	COSMOS 822872	CO(4-3)	10:02:02:09	+ 02:09:37.40	0.7	2.9 E+11	47.3
XD53	COSMOS 822965	CO(4-3)	10:01:58.73	+02:15:34.20	0.7028	8.9 E+10	39.5
XL53	COSMOS 824759	CO(4-3)	10:00:28.27	+02:16:00.50	0.7506	1.7E+11	28.6
XM53	COSMOS 810344	CO(4-3)	10:01:53.57	+01:54:14.80	0.7007	4.4 E+11	23.9
XN53	COSMOS 839268	CO(4-3)	10:00:11.16	+02:35:41.60	0.6967	1.1 E+11	24.2
XT53	COSMOS 823380	CO(4-3)	10:01:39.31	+02:17:25.80	0.7021	1.1 E+11	22.7
XE53	COSMOS 811360	CO(3-2)	10:01:00.74	+01:49:53.00	0.5297	8.9E+10	39.5
XG53	COSMOS 800405	CO(3-2)	10:02:16.78	+01:37:25.00	0.6223	1.5E+11	21.0
XR53	COSMOS 816955	CO(3-2)	10:01:41.85	+02:07:09.80	0.5165	1.9E+11	14.5
XU53	COSMOS 831384	CO(3-2)	10:00:40.37	+02:23:23.60	0.5172	1.9E+10	28.0
XV53	COSMOS 850140	CO(3-2)	10:01:43.66	+02:48:09.40	0.6248	6.3E+10	23.1
L14CO001	COSMOS 831870	CO(3-2)	10:00:18.91	+02:18:10.10	0.5024	1.5E+10	29.0

Table 5.1 – *ALMA observations from Cycle 3 and 4. Showing the same* $M_\star$ *and SFR from the table 4.1*

channel spacing of 2.5 km/s and an rms of 10.1 mJy per channel. The calibrated uv-tables were subsequently exported to GILDAS where the cleaning the cube analysis were performed.

sample selection

Our sample was taken from the IRAM PHIBSS2 sample and comprises twelve COSMOS galaxies at z=0.6-0.7 whose PHIBSS 2 CO(2-1) measurements had good SNR. The sample is shown in the table 5.1.

From our observation of Cycle 3 we did not have a SNR > 6.

This low detection rate is partly due to the small beam size (0.0500), which does not allow to recover all the signal given the SNR, and to the fragmented uv coverage. But together with our PHIBSS2 CO(2-1) measurements and other ALMA observations of multiple CO transitions it also hints at lower gas excitation levels in such star-forming galaxies than in the BzK selected galaxies studied by Daddi et al. (2015). Here we consequently prefer to target the less uncertain CO(3-2) transition, which was not accessible for the z = 0.7 galaxies initially observed, with a $\sim$0.1500 resolution and a higher SNR >9.

Our observations of Cycle 4 have a better resolution and SNR >7, nevertheless not all galaxies have detections for sub-kpc resolution. From twelve galaxies for our observations, four has a resolution to give a KS resolved(see figure 5.1).

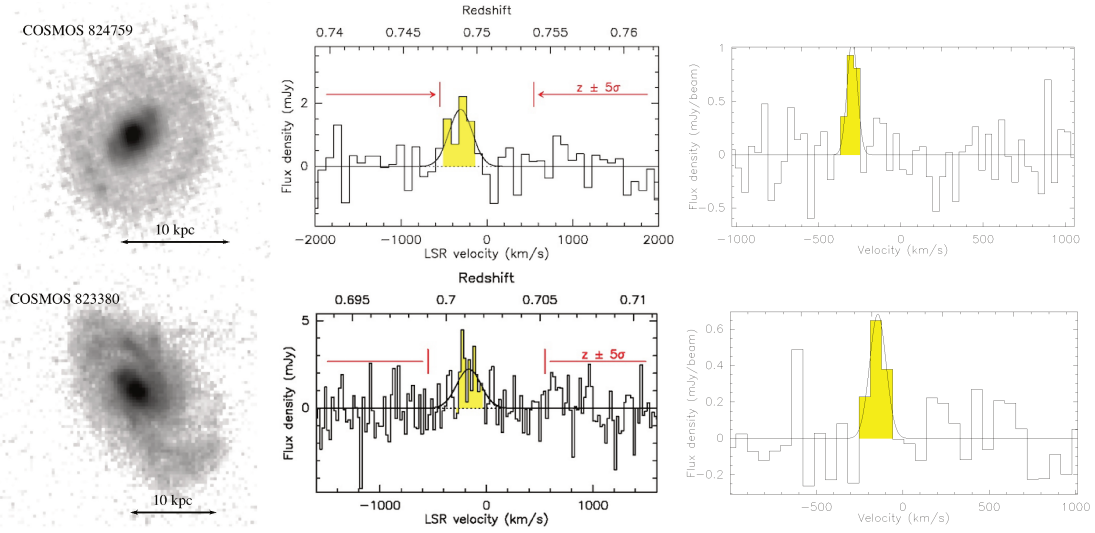

Figure 5.1 – *CO(4-3) spectra for two galaxies of our observation from 2015.*

Conclusion

CHAPTER 6

Conclusion and perspectives

The evolution of galaxies is strongly influenced by the manner in which gas condenses to become stars. A global correlation between SFR and gas surface density is obtained empirically when both quantities are normalized by the area of the stellar disk. Therefore, more thorough and precise measurements of this relationship is of major importance for better comprehending the phenomenon.

The process of star formation in galaxies is generally assumed to follow a single universal law, with an exponential N=1 (K98). This assumption is expected to be challenged in the coming years on account of new surveys . Through this we will be able to further constrain the star formation rate from the large quantity of data. It should also be remembered that apparently SFE may differ based on the analysis method. In some cases, galaxies may show a fixed relationship between SFR and density. If we study a galaxy through its individual parts, we may, for example, discover a constant SFE in up to the optical disk, above which (as we have already seen) there can be a steep decrease. As well, the total gas surface density cannot be beyond the critical quantity, which fixes the SFR over the HI dominated parts of these galaxies.

The SFE is also seen to vary among the galaxies. This can be seen in the range of the power law coefficients, as well as in the varying dex from one galaxy to another . Another open question is whether the Kennicutt-Schmidt law is fundamentally a molecular phenomena or if a single, universal power law relates total gas and star formation. Based on studies from Bigiel et al. (2008) and Leroy et al. (2008) it has become more clear that the molecular gas is indeed an important parameter to be properly accounted for in measurements of the surface density.

With the advent of a new generation of interferometers — ALMA in the South and NOEMA in the North — this domain of galactic studies has been made easier and more profound.

This work addresses the issue of star formation in the Universe from two different perspectives, with the ultimate goal of better understanding various aspects of galaxy

formation and evolution through different techniques and based upon new observations. In the first part we use the ALMA mosaic to study the outskirts of galaxies, specifically in XUV galaxies. We study the prototypical candidate for this type of galaxy: M83. In the second part this has been related to the observations of NOEMA for the PHIBSS program. Aiming to better understand quenching after the peak epoch of star formation, the PHIBSS2 program is now in its final stages. We also have two follow-up programs, which will use ALMA data of 12 galaxies. The aforementioned data was used to quantify the star formation activity (and principally their efficiency) through Kennicutt-Schmidt relations.

The two projects, regardless of new ALMA technology, still encountered problems with respect to CO emission. For the first project we had hypothesized that they should indeed be CO-dark in these regions. For the second part, it was found to be difficult to resolve galaxies at high redshift with sub-kpc resolution, as well to obtain a resolved KS. Even with ALMA's optical power it was discovered that we had underestimated the required amount of observation time.

XUV galaxies

We have reported about a mosaic of CO(2-1) observations obtained with ALMA in the outer disk of M83, rich in atomic gas and UV emission.

Our aim was to map CO emission in a small region around the galaxy centre ($r_{gal} = 11kpc$). The result is a dearth of CO emission. An automated search for CO emission in the data cube provides tentative detections of 14 clouds, but the CO(2-1) signal at 4-5 σ does not correspond spatially and spectrally to any other tracer. We considered then, therefore, as as false detections. Alongside this, we searched the CO map and extracted the spectra at regions corresponding to peaks of star formation (as traced by Hα). This did not provide any CO detection higher than 3σ.

We have also stacked all CO pixels for regions in which there is significant HI signal, shifting their velocity scale to a common central velocity expected from the HI signal. This gives a hint of detection, with a profile width of $\Delta V = 14$ km/s. The corresponding H_2 mass across the entire 4 x 2 kpc area is only 2 x 10^6 $M_\odot$. The H_2-to-HI mass ratio over this region is $< 3 \times 10^{-2}$.

We display the CO upper limits towards the star forming regions in the Kennicutt-Schmidt diagram, and the depletion time required to consume the molecular gas is found to be $<$ 3 x 10^8 yr, lower than in normal galaxy disks (3 x 10^9 yr). We had expected to find, in some pixels of 17 x 13pc, GMC masses of 10^6 $M_\odot$. However, the 3σ upper limits are $\sim 10^4$ $M_\odot$.

The explanation for this lack of CO emission could be due partly to a low metallicity, since the gas abundance in this region of M83 is half solar. The average metallicity for

H_{II} regions is $12 + log(O/H) = 8.4$ Bresolin et al. (2009). Other causes of the of the lack of CO may be the strong UV field, and the low global density of gas and dust (the gas is predominantly H_2, but the CO molecules only account for the minority of carbon). In the photodissociation regions, the carbon is found as C and C+.

In the outer parts of galaxies, where we find low gas surface densities, the size of the clouds are likely to be smaller than in the disk, and less self-shielded. The CO column density in each cloud is thus insufficient to avoid dissociation, and the region is dominated by C+ emission.

High redshift galaxies

The PHIBSS2 z = 0.5–0.8 measurements confirm the striking uniformity of the galaxy-averaged KS relation, with a linear exponent $n = 1$ at each epoch, and with a depletion time that varies slowly with redshift. The power-law $n = 1$ is indeed what was expected, as it corresponds to the main sequence galaxies after having averaged their respective SFRs (and their molecular gas surface densities) across the entirety of each galaxy.

Of the NOEMA observations from 61 galaxies, three were found to have sufficient resolution to study the relevant kinematics.

Using subgalactic scales could also tell us whether or not the star formation scaling law between the SFRs and gas surface densities is significantly different at high redshift, as opposed to in the local Universe. The KS for the whole galaxy shows a depletion time close to 1 Gyr, and for resolved higher-redshift measurements we seem to find lower values for the depletion time. The resolved KS gives a relationship that is not perfectly linear, as opposed to that found after averaging over many galaxies.

We conclude that CO observation is extremely important for properly studying the efficiency of star formation, regardless of the redshift: from the local Universe up to high-redshift main sequence galaxies. Even the non detection of molecular gas could help us to better understand the the processes, and the nature of the observations in CO emission. This could further clarify future observations that also return non-detections of CO emission.

References

References

Allen, R. J., Atherton, P. D., & Tilanus, R. P. J. 1986, Nature, 319, 296

Baldry, I. K., Glazebrook, K., Brinkmann, J., et al. 2004, ApJ, 600, 681

Bell, E. F., Papovich, C., Wolf, C., et al. 2005, ApJ, 625, 23

Bigiel, F., Leroy, A., Walter, F., et al. 2010, AJ, 140, 1194

Bigiel, F., Leroy, A., Walter, F., et al. 2008, AJ, 136, 2846

Bigiel, F., Leroy, A. K., Walter, F., et al. 2011, ApJ, 730, L13

Boissier, S., Gil de Paz, A., Boselli, A., et al. 2007, ApJS, 173, 524

Boissier, S., Prantzos, N., Boselli, A., & Gavazzi, G. 2003, Monthly Notices of the Royal Astronomical Society, 346, 1215

Bolatto, A. D., Wolfire, M., & Leroy, A. K. 2013, ARA&A, 51, 207

Boselli, A., Lequeux, J., & Gavazzi, G. 2002, A&A, 384, 33

Braine, J., Ferguson, A. M. N., Bertoldi, F., & Wilson, C. D. 2007, ApJ, 669, L73

Braine, J. & Herpin, F. 2004, Nature, 432, 369

Bresolin, F., Kudritzki, R.-P., Urbaneja, M. A., et al. 2016, ApJ, 830, 64

Bresolin, F., Ryan-Weber, E., Kennicutt, R. C., & Goddard, Q. 2009, ApJ, 695, 580

Bush, S. J., Cox, T. J., Hayward, C. C., et al. 2010, ApJ, 713, 780

Bush, S. J., Cox, T. J., Hernquist, L., Thilker, D., & Younger, J. D. 2008, ApJ, 683, L13

Caputi, K. I., Dole, H., Lagache, G., et al. 2006, ApJ, 637, 727

Cayatte, V., Kotanyi, C., Balkowski, C., & van Gorkom, J. H. 1994, AJ, 107, 1003

Christlein, D. & Zaritsky, D. 2008, ApJ, 680, 1053

Cibinel, A., Daddi, E., Bournaud, F., et al. 2017, MNRAS, 469, 4683

Combes, F. 1999, in Astronomical Society of the Pacific Conference Series, Vol. 187, The Evolution of Galaxies on Cosmological Timescales, ed. J. E. Beckman & T. J. Mahoney, 59–71

Combes, F. 2009, "Mysteries of Galaxy Formation"

Combes, F., García-Burillo, S., Braine, J., et al. 2011, A&A, 528, A124

Combes, F., García-Burillo, S., Braine, J., et al. 2013, A&A, 550, A41

Crosthwaite, L. P., Turner, J. L., Buchholz, L., Ho, P. T. P., & Martin, R. N. 2002, AJ, 123, 1892

Cuillandre, J.-C., Lequeux, J., Allen, R. J., Mellier, Y., & Bertin, E. 2001, ApJ, 554, 190

Daddi, E., Bournaud, F., Walter, F., et al. 2010, ApJ, 713, 686

Daddi, E., Dickinson, M., Morrison, G., et al. 2007, ApJ, 670, 156

Daddi, E., Elbaz, D., Walter, F., et al. 2010, ApJ, 714, L118

Daddi, E., Renzini, A., Pirzkal, N., et al. 2005, ApJ, 626, 680

Damen, M., Labbé, I., Franx, M., et al. 2009, ApJ, 690, 937

Davis, M., Guhathakurta, P., Konidaris, N. P., et al. 2007, ApJ, 660, L1

de Blok, W. J. G. & Walter, F. 2003, MNRAS, 341, L39

Dessauges-Zavadsky, M., Verdugo, C., Combes, F., & Pfenniger, D. 2014, A&A, 566, A147

Dong, H., Calzetti, D., Regan, M., et al. 2008, AJ, 136, 479

Dopita, M. A. & Ryder, S. D. 1994, ApJ, 430, 163

Elbaz, D. & Cesarsky, C. J. 2003, Science, 300, 270

Elbaz, D., Daddi, E., Le Borgne, D., et al. 2007, A&A, 468, 33

Elmegreen, B. G. 2002, ApJ, 577, 206

Elmegreen, B. G., Morris, M., & Elmegreen, D. M. 1980, ApJ, 240, 455

Elmegreen, B. G. & Parravano, A. 1994, ApJ, 435, L121

Ferguson, A. M. N., Gallagher, J. S., & Wyse, R. F. G. 1998, AJ, 116, 673

Freundlich, J., Combes, F., Tacconi, L. J., et al. 2013, A&A, 553, A130

Gardan, E., Braine, J., Schuster, K. F., Brouillet, N., & Sievers, A. 2007, A&A, 473, 91

Genzel, R., Tacconi, L. J., Gracia-Carpio, J., et al. 2010, MNRAS, 407, 2091

Genzel, R., Tacconi, L. J., Kurk, J., et al. 2013, ApJ, 773, 68

Genzel, R., Tacconi, L. J., Lutz, D., et al. 2015, ApJ, 800, 20

Giavalisco, M., Dickinson, M., Ferguson, H. C., et al. 2004, ApJ, 600, L103

Gil de Paz, A., Boissier, S., Madore, B. F., et al. 2007a, ApJS, 173, 185

Gil de Paz, A., Madore, B. F., Boissier, S., et al. 2005, ApJ, 627, L29

Gil de Paz, A., Madore, B. F., Boissier, S., et al. 2007b, ApJ, 661, 115

Goddard, Q. E., Kennicutt, R. C., & Ryan-Weber, E. V. 2010, MNRAS, 405, 2791

Governato, F., Brook, C., Mayer, L., et al. 2010, Nature, 463, 203

Gratier, P., Braine, J., Rodriguez-Fernandez, N. J., et al. 2010, A&A, 522, A3

Hunter, D. A., Elmegreen, B. G., & Baker, A. L. 1998, ApJ, 493, 595

Kauffmann, G., Heckman, T. M., Budavári, T., et al. 2007, ApJS, 173, 357

Kennicutt, Jr., R. C. 1998, ApJ, 498, 541

Koda, J., Yagi, M., Boissier, S., et al. 2012, ApJ, 749, 20

Kravtsov, A. V. 2003, ApJ, 590, L1

Krumholz, M. R. 2013, IAUS, 292, 227

Krumholz, M. R., McKee, C. F., & Tumlinson, J. 2009, ApJ, 693, 216

Lada, C. J., Lombardi, M., & Alves, J. F. 2010, ApJ, 724, 687

Lamarche, C., Stacey, G., Brisbin, D., et al. 2017, ApJ, 836, 123

Larson, R. B. & Tinsley, B. M. 1978, ApJ, 219, 46

Lelièvre, M. & Roy, J.-R. 2000, AJ, 120, 1306

Leroy, A. K., Walter, F., Brinks, E., et al. 2008, AJ, 136, 2782

Leroy, A. K., Walter, F., Sandstrom, K., et al. 2013, AJ, 146, 19

Li, Y., Mac Low, M.-M., & Klessen, R. S. 2006, ApJ, 639, 879

Lilly, S. J., Le Fevre, O., Hammer, F., & Crampton, D. 1996, ApJ, 460, L1

Lombardi, M., Alves, J., & Lada, C. J. 2010, A&A, 519, L7

Madau, P. & Dickinson, M. 2014, ARA&A, 52, 415

Madau, P., Ferguson, H. C., Dickinson, M. E., et al. 1996, MNRAS, 283, 1388

Martin, C. L. & Kennicutt, Jr., R. C. 2001, ApJ, 555, 301

Meurer, G. R., Wong, O. I., Kim, J. H., et al. 2009, ApJ, 695, 765

Mihos, J. C. & Hernquist, L. 1996, ApJ, 464, 641

Mo, H., van den Bosch, F. C., & White, S. 2010, Galaxy Formation and Evolution

Moffett, A. J., Kannappan, S. J., Baker, A. J., & Laine, S. 2012, ApJ, 745, 34

Morganti, R., de Zeeuw, P. T., Oosterloo, T. A., et al. 2006, MNRAS, 371, 157

Narayanan, D., Krumholz, M. R., Ostriker, E. C., & Hernquist, L. 2012, MNRAS, 421, 3127

Noeske, K. G., Weiner, B. J., Faber, S. M., et al. 2007, ApJ, 660, L43

Oosterloo, T. A., Morganti, R., Sadler, E. M., van der Hulst, T., & Serra, P. 2007, A&A, 465, 787

Pettini, M. & Pagel, B. E. J. 2004, MNRAS, 348, L59

Pflamm-Altenburg, J. & Kroupa, P. 2008, Nature, 455, 641

Planck Collaboration, Ade, P. A. R., Aghanim, N., et al. 2015, ArXiv: 1502.01589

Planck Collaboration, Aghanim, N., Akrami, Y., et al. 2017, A&A, 607, A95

Popescu, C. C. & Tuffs, R. J. 2003, A&A, 410, L21

Rodighiero, G., Daddi, E., Baronchelli, I., et al. 2011, ApJ, 739, L40

Roy, J.-R. 2017, "Unveiling Galaxies"

Saintonge, A., Catinella, B., Tacconi, L. J., et al. 2017, ApJS, 233, 22

Saintonge, A., Kauffmann, G., Wang, J., et al. 2011, MNRAS, 415, 61

Santini, P., Fontana, A., Grazian, A., et al. 2009, A&A, 504, 751

Sargent, M. T., Béthermin, M., Daddi, E., & Elbaz, D. 2012, ApJ, 747, L31

Schmidt, M. 1959, ApJ, 129, 243

Schruba, A., Leroy, A. K., Walter, F., et al. 2011a, AJ, 142, 37

Schruba, A., Leroy, A. K., Walter, F., et al. 2011b, AJ, 142, 37

Schuster, K. F., Kramer, C., Hitschfeld, M., Garcia-Burillo, S., & Mookerjea, B. 2007, A&A, 461, 143

Scoville, N. 2007, in Astronomical Society of the Pacific Conference Series, Vol. 375, From Z-Machines to ALMA: (Sub)Millimeter Spectroscopy of Galaxies, ed. A. J. Baker, J. Glenn, A. I. Harris, J. G. Mangum, & M. S. Yun, 166

Sellwood, J. A. & Balbus, S. A. 1999, ApJ, 511, 660

Shetty, R., Kelly, B. C., & Bigiel, F. 2013, MNRAS, 430, 288

Silk, J. 1997, ApJ, 481, 703

Sparke, L. S. & Gallagher, III, J. S. 2007, "Galaxies in the Universe"

Steinmetz, M. & Navarro, J. F. 2002, New A, 7, 155

Tacconi, L. J., Genzel, R., Neri, R., et al. 2010, Nature, 463, 781

Tacconi, L. J., Genzel, R., Saintonge, A., et al. 2018, ApJ, 853, 179

Tacconi, L. J., Neri, R., Genzel, R., et al. 2013, ApJ, 768, 74

Tacconi, L. J. & Young, J. S. 1987, ApJ, 322, 681

Taylor, C. L., Kobulnicky, H. A., & Skillman, E. D. 1998, AJ, 116, 2746

Thilker, D. A., Bianchi, L., Boissier, S., et al. 2005, ApJ, 619, L79

Thilker, D. A., Bianchi, L., Meurer, G., et al. 2007, ApJS, 173, 538

Utomo, D., Blitz, L., Bolatto, A., Wong, T., & Vogel, S. 2015, IAU General Assembly, 22, 57914

van Zee, L., Haynes, M. P., Salzer, J. J., & Broeils, A. H. 1997, AJ, 113, 1618

Verdugo, C., Combes, F., Dasyra, K., Salomé, P., & Braine, J. 2015, A&A, 582, A6

Vio, R. & Andreani, P. 2016, A&A, 589, A20

Walter, F., Brinks, E., de Blok, W. J. G., et al. 2008, AJ, 136, 2563

Watson, L. C., Martini, P., Lisenfeld, U., Böker, T., & Schinnerer, E. 2016, MNRAS, 455, 1807

Weinzirl, T., Jogee, S., Khochfar, S., Burkert, A., & Kormendy, J. 2009, ApJ, 696, 411

White, S. D. M. & Rees, M. J. 1978, MNRAS, 183, 341

Wong, T. & Blitz, L. 2002, ApJ, 569, 157

Wuyts, S., Förster Schreiber, N. M., van der Wel, A., et al. 2011a, ApJ, 742, 96

Wuyts, S., Förster Schreiber, N. M., van der Wel, A., et al. 2011b, ApJ, 742, 96

Zamora-Avilés, M. & Vázquez-Semadeni, E. 2014, ApJ, 793, 84

Zamora-Avilés, M., Vázquez-Semadeni, E., & Colín, P. 2012, ApJ, 751, 77

Zaritsky, D. & Christlein, D. 2007, AJ, 134, 135

Zasov, A. V. & Smirnova, A. A. 2005, Astronomy Letters, 31, 160